

REPORT DOCUMENTATION PAGE

AFRL-SR-BL-TR-98-

8

Public reporting burden for this collection of information is estimated to average 1 hour per response, including the time for reviewing the data needed, and completing and reviewing the collection of information. Send comments regarding this burden estimate or any other aspect of this collection of information, including suggestions for reducing this burden, to Washington Headquarters Services, Directorate for Information Operations and Reports, 1204, Arlington, VA 22202-4302, and to the Office of Management and Budget, Paperwork Reduction Project (0743).

ces, gathering
s collection of
highway, Suite

1. AGENCY USE ONLY (Leave Blank)	2. REPORT DATE June, 1994	3. REPORT TYPE AND DATES COVERED Final	
4. TITLE AND SUBTITLE Wall-Fluid Instabilities in Compliant Channels Conveying Developing Flows		5. FUNDING NUMBERS	
6. AUTHORS Peter Gavin Larose			
7. PERFORMING ORGANIZATION NAME(S) AND ADDRESS(ES) Northwestern University		8. PERFORMING ORGANIZATION REPORT NUMBER	
9. SPONSORING/MONITORING AGENCY NAME(S) AND ADDRESS(ES) AFOSR/NI 4040 Fairfax Dr, Suite 500 Arlington, VA 22203-1613		10. SPONSORING/MONITORING AGENCY REPORT NUMBER	
11. SUPPLEMENTARY NOTES			
12a. DISTRIBUTION AVAILABILITY STATEMENT Approved for Public Release		12b. DISTRIBUTION CODE	
13. ABSTRACT (Maximum 200 words) See Attachment			
14. SUBJECT TERMS		15. NUMBER OF PAGES	
		16. PRICE CODE	
17. SECURITY CLASSIFICATION OF REPORT Unclassified	18. SECURITY CLASSIFICATION OF THIS PAGE Unclassified	19. SECURITY CLASSIFICATION OF ABSTRACT Unclassified	20. LIMITATION OF ABSTRACT UL

DTIC QUALITY INSPECTED 8

NORTHWESTERN UNIVERSITY

WALL-FLUID INSTABILITIES IN COMPLIANT CHANNELS CONVEYING
DEVELOPING FLOWS

A DISSERTATION

SUBMITTED TO THE GRADUATE SCHOOL
IN PARTIAL FULFILLMENT OF THE REQUIREMENTS

for the degree

DOCTOR OF PHILOSOPHY

Field of Engineering Sciences and Applied Mathematics

By

PETER GAVIN LAROSE

Evanston, Illinois

June 1994

19981202 036

© Copyright by P. Gavin LaRose 1994
All Rights Reserved

ABSTRACT

Wall-Fluid Instabilities in Compliant Channels Conveying Developing Flows

Peter Gavin LaRose

A collapsed lung airway or flexible tube is modelled as a two-dimensional channel of infinite length. We consider the linear stability of this system conveying a developing flow profile, which is approximated with a uniform profile and perturbation of the Blasius profile for flow over a flat plate. Exact and asymptotic solutions are found for the uniform profile. For the perturbation profile an analytical solution is found for long waves and a numerical shooting solution for arbitrary wave lengths. Results for the uniform and perturbation profiles are found to be generally in qualitative agreement, though the perturbation profile is less stable. For the perturbation profile we find a long wave instability which is absent for uniform flow and hence has not been seen in previous channel studies. This is stabilized by increasing the elastance of the wall, but other wall properties do not affect the critical flow speed except in correction terms. Increasing the channel width decreases the critical flow speed for the instability, but increases the critical flow rate. We hypothesize that this is related to the tube collapse that is seen in this type of system prior to the appearance of an oscillatory (flutter) instability. The finite wave length (flutter) instability is destabilized by decreasing wall damping, increasing wall inertia, decreasing wall elastance or flexural rigidity, and decreasing channel width, and may appear independent of or simultaneously with the long wave instability. Comparisons with experimental investigations of air flow in flexible tubes shows that the theoretically predicted flutter frequencies are in good agreement with

those observed experimentally, but that there are difficulties in comparing the predicted critical flow speeds, due to the tube geometry introduced by the tube collapse that precedes flutter. We investigate the possible effect of this geometry using finite elements software to model flow in the collapsed tube cross-section. Finally, we compare the experimentally observed critical flow speeds for the onset of collapse with our theoretical predictions for the long wave instability, finding qualitative support for our hypothesis that collapse is the physical manifestation of the long wave instability.

Advisor: Professor James B. Grotberg

ACKNOWLEDGEMENTS

That I am even considering being able to finish my graduate work is a tribute to the support and assistance of many, the magnitude of whose help I do not pretend to be able to summarize here. Special thanks, nonetheless, to: Professor Jim Grotberg, my advisor, for keeping me productive (insofar as possible) and for reminding me that learning is progress; to all of the members of the lab/office in which I had the pleasure to work (and move twice), esp. Drs. David Halpern, Yahong Jiang, and Oliver Jensen, for listening and talking (and good advice); to Professors Steve Davis and Grae Worster, for willing advice and physical intuition; to Professors Mike Miksis and Ed Olmstead, for stepping up to fill out my defense committee; to all of the ES/AM graduate students with whom I have shared the last five years, esp. Dan, Joe, Nathan, Burt, Cheryl, and Dan. And to all others whom I have in my mind-worn state forgotten, and everyone who helped and hoped with me, in particular Mum, Dad and David.

I also acknowledge the financial support of Northwestern University and the Department of Defence NDSEG Fellowship Program, without which none of this work would have been even started.

TABLE OF CONTENTS

ABSTRACT	iii
ACKNOWLEDGEMENTS	v
LIST OF TABLES	viii
LIST OF FIGURES	ix
CHAPTER 1 Introduction	
1.1 Motivation	1
1.2 Characteristics of flexible tubes	1
1.3 Flow limitation and flutter in the lung	3
1.4 Organization of the remainder of the dissertation	4
CHAPTER 2 Literature Review	
2.1 Overview	5
2.2 Early work and instability types	7
2.3 Work with finite length panels and pipes in potential flow	8
2.4 Work with channel flow	9
2.5 Additional work on flow over compliant plates	12
2.6 Other approaches	14
2.7 Conclusions	16
CHAPTER 3 Model Derivation	
3.1 Derivation of nondimensional equations and boundary conditions	18
3.2 System linearization and simplification	22
3.3 Specification of the base flow profile	24
CHAPTER 4 Asymptotic and Exact Solutions for a Plug Flow Base State	
4.1 Introduction and equations	30
4.2 Asymptotic solution	31
4.3 Exact solution	37
4.4 Results	40
CHAPTER 5 Numerical and Analytical Solutions for Developing Base Flow	
5.1 Introduction and equations	55
5.2 Analytical solution for long waves	56
5.3 Numerical solution method	62
5.4 Comparison with known stability results	66
5.5 Results	69
5.6 Discussion of the limit of infinite channel width	82

CHAPTER 6 Comparison with Experiments	
6.1 Overview	85
6.2 Comparison with flutter in tube experiments	85
6.3 Comparison with collapse in tube experiments	88
6.4 The TSI in the tube experiments	89
6.5 Comparison with wheezing in the lung	90
CHAPTER 7 Conclusions and Discussion	
7.1 Summary	94
7.2 Discussion of the Tollmien-Schlichting instability	95
7.3 The effect of nonparallelism in the base flow	96
7.4 Directions for future work	97
REFERENCES	99
APPENDIX A Finite Difference Solution for Developing Channel Flow	
A.1 Problem formulation and uniform grid difference scheme	105
A.2 Modifications for a non-uniform grid	109
A.3 Results	110
APPENDIX B FIDAP Solution for Flow in a Collapsed Tube	
B.1 Solution procedure	112
B.2 Results	112
CURRICULUM VITAE	116

LIST OF TABLES

Table V.i	Comparison of critical Reynolds and wave numbers for TSI in flows with rigid boundaries	67
Table V.ii	Comparison of Blasius flutter roots from present and past work, scaled on maximum flow speed and boundary layer displacement thickness	68
Table VI.i	Dimensional and non-dimensional parameters for lung airways	91
Table VI.ii	Theoretically predicted flutter frequencies and critical flow rates for the parameters indicated in table VI.i.	92

LIST OF FIGURES

Figure 3.1 Flexible walled channel system	18
Figure 3.2 Solutions for developing channel flow	28
Figure 4.1 Plug flow dispersion relation for undamped system	41
Figure 4.2 Plug flow dispersion relation for damped system, root 2	42
Figure 4.3 Plug flow dispersion relation, showing difference between exact and asymptotic solutions	43
Figure 4.4 Plug flow dispersion relation, showing singularity in asymptotic solution . . .	44
Figure 4.5 Neutral stability curves for plug flow	46
Figure 4.6 Plug flow neutral stability curves for different M , G , showing long wave stabilization	48
Figure 4.7 Plug flow critical flow speed S_{CR}^F and flutter frequency as functions of wall damping and mass ratio	49
Figure 4.8 Plug flow S_{CR}^F and flutter frequency as functions of wall elastance and bending stiffness	51
Figure 4.9 Plug flow S_{CR}^F and flutter frequency as functions of half channel width and wall elastance	52
Figure 4.10 Plug flow neutral stability curves for different half channel widths	54
Figure 5.1 Critical flow speeds and frequencies as functions of half channel width and elastance	59
Figure 5.2 Critical volumetric flow rate for long wave instability as a function of half channel width and elastance	60
Figure 5.3 Neutral stability curve for Blasius flow over a single rigid plate, TSI	70
Figure 5.4 Neutral stability curve for Blasius flow over a single compliant plate, TSI . . .	71
Figure 5.5 Developing flow flutter dispersion relation as a function of flow speed; root 1	73
Figure 5.6 Neutral stability curves, flutter instability	74

Figure 5.7 Neutral stability curves for different mass ratios, showing long wave and flutter instabilities	75
Figure 5.8 Critical flow speeds S_{CR}^{LW} and S_{CR}^F and frequency at S_{CR} as functions of wall damping and mass ratio	76
Figure 5.9 Critical flow speed S_{CR} ($= S_{CR}^F$) and flutter frequency as functions of wall elastance E	78
Figure 5.10 Neutral stability curves for different channel widths, showing long wave instability and comparison with Blasius flow over a single compliant plate	80
Figure 5.11 Dispersion relation for developing flow in a very wide channel, showing singularity at $S = \text{real}(c)$	83
Figure A.1 Finite difference solution for developing channel flow	111
Figure B.1 Meshed domain for FIDAP computations	113
Figure B.2 Vector plots of steady velocity in collapsed tube cross-section	114
Figure B.3 Contour plots of steady velocity in collapsed tube cross-section	115

CHAPTER 1: INTRODUCTION

§1.1 *Motivation*

In this dissertation we examine the stability of a flexible, fluid-conveying two-dimensional channel. This is a model for the many systems in engineering and physiology in which flows are conveyed by tubes that are to some degree flexible. In engineering applications the existence of flow-induced vibrations or larger scale motion, *e.g.* in oil pipelines, may attest to the flexibility of a tube, and in other applications, *e.g.* physiological tubes such as the lung airways, the flexibility of such a structure is more obvious. In many of these applications the tubes are short and flow speeds large, so that the flows do not become fully developed. This is the case for the application in which we are primarily interested, the lung airways, which have air flow through short, thick-walled tubes. It is thought that wheezing lung sounds are symptomatic of an oscillatory wall-fluid instability (flutter), and this motivates the present study.

§1.2 *Characteristics of flexible tubes*

There are a number of interrelated steady and unsteady behaviors that occur in flexible fluid-conveying tubes which are absent in rigid systems. If the pressure difference between the exterior and interior of such a tube is sufficiently large, the tube may collapse, resulting in an obstruction of the tube cross-sectional area. With increasing pressure, the initially circular cross-section becomes oval, then dumbbell shaped, and finally reduces to a pair of small conduits connected by a completely closed center section (Shapiro 1977). For very flexible tubes the pressure difference required to precipitate collapse may be small enough that easily attainable changes in the tube environment, or the pressure drop resulting from a flow in the tube interior,

may be sufficient to cause some degree of reduction in the tube cross-sectional area. With the occurrence of collapse, the flow rate through the tube may become independent of the conditions at the downstream end of the tube, either from wave-speed limitation (Dawson and Elliot 1977; Shapiro 1977) or viscous limitation (Shapiro 1977). While the flow rate remains constant, however, the flow speed in the tube may still increase with decreasing downstream pressure to maintain mass conservation through the narrowing collapsed section of the tube. Concurrent with or following collapse, large or small amplitude oscillations of the tube walls may also be seen; small amplitude wall oscillations may also occur in less flexible (uncollapsed) tubes transporting fluids at sufficiently high velocities.

The oscillatory wall-fluid instabilities that are present in flexible tubes may be divided into two categories; those that require wall inertia (which we call flutter) and those that do not. The work on oscillatory instabilities in the absence of wall inertia is the subject of a review by Kamm and Pedley (1989); we refer the reader to their paper for a complete treatment of and reference list for this subject. Instabilities of this type are commonly large amplitude, lower frequency oscillations due to unsteady head loss resulting from the motion of the separated flow region downstream of a constriction in the tube. Flutter instabilities are small amplitude, high frequency oscillations arising from the coupling of the fluid-dynamic pressure with the compliant wall. Instabilities similar in mechanism to Kelvin-Helmholtz and water waves are among these. For the appearance of a flutter instability, a well defined critical fluid velocity must be attained. Flow limitation is not a prerequisite for the instability, but flutter may be facilitated through the decrease in tube cross-sectional area and resulting increase in fluid flow speed that accompany limitation, and in experimental studies of flutter in thick-walled tubes (Gavriely *et.al.* 1989) and wheezing in the lung (Gavriely *et.al.* 1987) these oscillatory phenomena have in fact been

observed only in the presence of flow limitation.

§1.3 *Flow limitation and flutter in the lung*

Flow limitation is well documented in the lung, and is described in a review by Hyatt (1983). In healthy subjects, flow limitation may be seen in forceful exhalation, and in lung obstructed patients the effort required to cause flow limitation may be low enough that the flow rate in normal breathing may become limited. In collapsible tubes oscillatory instabilities are seen following tube collapse and flow limitation (Gavriely *et.al.* 1989), and it was proposed by Grotberg and Davis (1980) that wheezing lung sounds may be symptomatic of such a flutter instability in the lung airways. Experiments with forced expiratory wheezes and lung preparations have shown that flow limitation is a requisite for wheezing sounds (Gavriely *et.al.* 1987), that these sounds are dependant on wall, rather than gas, properties (Shabtai *et.al.* 1992), and that they depend on the flexibility of lung structures (Gavriely and Grotberg 1988). Thus a wall-fluid instability provides a likely explanation for the wheezing sounds heard on forced exhalation and in lung preparations. Further, as the spectral content and other characteristics of these sounds are similar to those of wheezes in patients with asthma and other lung obstructive diseases (Gavriely *et.al.* 1987) and tube experiments (Gavriely *et.al.* 1989), the sound-producing mechanism in each is likely to be the same. In tube experiments, in particular, oscillatory instabilities may be observed directly and compared with theoretical investigations of flutter (Grotberg and Gavriely 1989) to demonstrate that this provides a likely explanation for experimental observations.

Other possible mechanisms for the generation of wheezing lung sounds were considered by Gavriely *et.al.* (1984). Of these, the only one consistent with the experimental observations described above (besides flutter) is vortex resonance, the resonance of vortices shed from a sharp

edge or constriction with the natural frequency of the compliant airway wall, thus exciting oscillations. It appears, however, that there is more evidence to support flutter as the cause of wheezing lung sounds.

§1.4 *Organization of the remainder of the dissertation*

In the preceding we have outlined the experimentally observed behavior of compliant tubes and the evidence linking this to the lung airways. In particular, we observed support for the theory that wheezing lung sounds are symptomatic of flutter of the airway walls. In the next chapter we review the theoretical work providing insight on the problem of oscillatory instabilities in fluid-conveying compliant tubes and channels. We develop a model of a collapsed lung airway or flexible tube in Chapter 3, solutions for which are obtained in Chapters 4 and 5. In Chapter 6 we compare results obtained with these models with tube experiments and forced expiratory wheezes. In Chapter 7 we conclude our analysis with a final discussion of the results obtained.

CHAPTER 2: LITERATURE REVIEW

§2.1 Overview

Given the wide range of physiological and engineering applications involving flow through compliant tubes, it comes as no surprise that there is an expansive body of literature involving the theoretical analysis of such systems. In this chapter we review the more relevant of these works.

For flow through collapsible tubes there is a volume of work with lumped parameter and one-dimensional models. Lumped parameter models (*e.g.* Conrad 1969; Katz *et.al.* 1969) condense the global effects of the tube geometry and fluid flow into an equation for a simple time-dependent variable, and illustrate the coupling of effects within the system, but are otherwise of limited application. One-dimensional models consider the fluid variables and tube cross-sectional area to be functions of time and distance along the tube; these are found through solution of the fluid equations, supplemented by a 'tube law' relating the tube cross-sectional area to the transmural pressure. These models have been applied to the analysis of steady tube collapse (Shapiro 1977) and to unsteady behavior (Kamm and Shapiro 1979) and flow-induced oscillations (Cancelli and Pedley 1985) in the absence of inertia. However, while these studies have been fundamental in understanding the behavior of collapsible tubes, they do not include investigations of the flutter instability. We therefore do not review this field here, and instead refer the interested reader to the review of Kamm and Pedley (1989).

While we are specifically interested in studying the behavior of compliant fluid-transporting tubes (or channels), there is considerable overlap between the nature of the flutter instability in such systems and that for flows over single compliant plates. Our review therefore

covers work on both subjects, and while we use the distinction between the geometries to discriminate between studies, the chapter sections are divided according to other criteria that are more significant in determining the characteristics of the instabilities in the system. It is perhaps not coincidental that these differences correspond roughly to the motivations for the studies. Before continuing with the review proper we briefly summarize these motivations and outline the organization of the remainder of the chapter.

In §2.2 we review some of the earliest investigations of the stability of flows with compliant boundaries, which were inspired by the experimental work of Kramer (1960) on drag reduction by use of surface compliance. The observation of oscillations in pipelines and other structures spurred investigation of the stability of inviscid flow through tubes and over panels; we consider this in §2.3. In §2.4 we describe channel studies motivated by interest in both engineering and physiological applications, which clarify some of the behavior seen previously. Some recent work on the stability of flow over a compliant plate and the possibility of drag reduction by use of a compliant surface are reviewed in §2.5. Finally in §2.6 we briefly consider some of the other approaches in the analysis of the behavior of systems involving flow past compliant structures, including forcing and full numerical simulations. In §2.7 we conclude our review in the context of the present work.

Clearly the investigation of such stiff structures as pipelines will proceed from a slightly different viewpoint than will work on the more flexible tubes that are found in physiological applications. Even for tubes that are not for flow rates of general interest susceptible to the collapse phenomenon seen in more flexible tubes, however, the stability analysis of the flutter instability may proceed in a similar manner to that for more flexible systems, and as a result insight may be gained from considering these studies.

§2.2 *Early work and instability types*

The pioneering work on the interaction of flows with compliant structures is that of Benjamin and Landahl, who in the early 1960s considered the stability of flow over a compliant panel. In that the Tollmien-Schlichting instability is due to viscosity, which is confined to a narrow boundary layer near the wall, Benjamin (1960) observed that wall flexibility should have a significant effect on the instability. His and later work (Landahl 1962, Benjamin 1963) confirmed this, and also showed that there are in addition to the viscous fluid instability other wall-fluid instabilities which arise as a direct result of wall compliance and which may exist in the absence of viscosity; these include the instability corresponding to the channel flutter in which we are interested. Benjamin and Landahl classified these instabilities as Types A, B or C waves according to the change of the total kinetic and elastic energy in the system necessary for their growth. Type A instabilities are negative energy waves in the sense that these energies decrease as the amplitude of the wave increases; Type B are precisely the opposite, and for Type C waves the energy remains unchanged. The stability of Types A and B waves is thus determined by the net effect of non-conservative forces in the system while Type C waves are destabilized by the unidirectional transfer of energy from the fluid to the wall by conservative forces, and are analogous to the Kelvin-Helmholtz instability of superposed fluids. Type C waves arise as the coalescence of a Type A and a Type B wave, and are the only type of instability possible in a conservative system. The Tollmien-Schlichting instability may be classified as Type A. As the growth of Type A waves requires a decrease in system energy such waves will be destabilized by wall damping, while, conversely, Type B waves will be stabilized. Miles (1957) demonstrated that for a shear flow over a wavy wall there may exist a component of fluid pressure in phase with the slope of the wall; this pressure component may do work on, and thus add energy to, the

wall. Through this effect, the addition of viscosity to the problem may stabilize Type A waves and destabilize Type B waves. Dissipative processes do not affect the stability of Type C waves, but do cause a slight decrease in their growth rate.

Benjamin and Landahl showed that as the wall flexibility is increased the Tollmien Schlichting instability (TSI) is stabilized. To postpone the onset of instability, however, it is also necessary to avoid the destabilization of the other wave types, so that the compliant surface must be chosen with care to obtain any significant improvement in stability (Landahl 1962). A similar stabilization of the TSI was seen by Hains and Price (1962) for Poiseuille flow through a flexible channel. A good review of this early work appears in Benjamin (1964).

§2.3 *Work with finite length panels and pipes in potential flow*

We next consider work on the stability of systems consisting of compliant panels or tubes of finite length with potential flows. As the flows are inviscid no information is gained on the behavior of the TSI, but the nature of the wall-fluid flutter instability may be examined.

Weaver and Unny (1970) considered the stability of a system with potential flow over a two dimensional flexible plate of finite length. They found a divergence instability as the flow speed is increased, that is, an instability with zero phase speed; physically divergence may take the form of a stationary or slowly moving, growing wave train on the flexible surface. At onset this is a mode one instability, meaning that a single wave spans the entire surface, but Weaver and Unny predicted that at higher flow speeds oscillations may be seen, followed by a second divergence mode. However, in that they used linear theory it is not clear that their conclusions regarding the behavior of the system following the onset of instability are valid. The addition of damping to the wall has little effect on the instability. Similar results were seen by Kornecki

(1974), Kornecki *et. al.* (1976) and Ellen (1973).

The results for finite length tubes conveying potential flows are similar to those for panels. Weaver and Unny (1973) and Kornecki (1974) examined the behavior of such systems and determined that the instability is again divergent at criticality, with flutter occurring only at higher flow speeds, if at all (though, again, the use of linear theory calls into question conclusions drawn following the onset of instability). This flutter is a 'coupled mode' instability arising from the coalescence of two divergence modes; the manner in which this coupling takes place was elucidated by Païdoussis and Issid (1974), who considered the problem with a more accurate pipe model. Depending on the choice of wall characteristics the flutter instability may or may not be present, though when present it is always preceded by divergence. Païdoussis and Issid's work also includes a review of the literature on the problem of the stability of flow in flexible pipes.

§2.4 *Work with channel flow*

A channel may be seen as a two dimensional model of a tube, but there are additional physical considerations that suggest that the channel geometry is worthy of attention. Weaver and Païdoussis (1977) observed that the flutter instability seen in tubes is not the classical shell flutter mode in which the tube flattens alternately in the two perpendicular directions normal to the tube axis, but rather a 'flapping flutter' that occurs after the tube has flattened somewhat to become oval. This flapping flutter then involves the oscillation of the longer opposing walls of this oval either in or out of phase with one another, and its nature suggests that it might be appropriate to model the tube as a channel. A similar conclusion may be reached on consideration of the nature of the collapse and oscillation of the flexible tubes appearing in physiology; these tubes are more flexible than those considered by the authors mentioned in §2.3, so that there may be dramatic

changes in their cross-sectional geometry, as noted in §1.2. In this case a circular tube model is not representative of the actual tube geometry, and it may be more appropriate to instead model the central (flat) section of the collapsed tube (which is that which oscillates) as a channel.

Motivated by their observation, Weaver and Païdoussis considered a channel with flexible walls conveying an inviscid flow. They used two wall models, one with inertia, bending stiffness and damping, and another consisting of two parallel plates with constrained edges but infinite length (so that the channel was in this case essentially three dimensional, but without side walls). In either case they found a divergence instability for both the symmetric and antisymmetric flutter modes (in which the channel walls oscillate out of or in phase with one another, respectively), followed by coupled mode flutter. Again, only linear theory was considered, so that their demonstration of flutter remains inconclusive. They compared these results with experiments and found qualitative agreement. (It should be noted that Weaver and Païdoussis used the method of images to find the fluid velocity; however, while this results in an expression involving an infinite sum, they included only the first two terms, so that their solution allows cross-flow at the walls of the channel.) Matsuzaki and Fung (1977) considered a similar problem, with inviscid flow through a channel with a flexible section of finite length, modelled using the von Kàrmàn plate equations, and also found a divergence instability.

Grotberg and Davis (1980) considered the channel flow problem (with flexible walls of infinite length) as a model of a collapsed lung airway, theorizing that wheezing lung sounds may be symptomatic of a flutter oscillation in the airway walls. They used two wall models that included inertia and either bending stiffness or elastance, respectively, and found a flutter instability unless wall damping was also included in the wall, in which case instability appeared at lower flow speeds and was divergent. This is consistent with the results of Weaver and

Païdoussis (1977), as the latter considered only damped walls. Grotberg and Davis showed also that results obtained in the two dimensional geometry are consistent with one dimensional studies (e.g. Shapiro, 1977). The drop in critical flow speed with the addition of damping was first explained by Landahl (1962), who showed that without wall damping there is preceding the appearance of instability a state of unstable equilibrium (neutral stability) that is broken through the addition of damping, thereby reducing the critical flow speed. A similar drop in critical flow speed may be obtained by including fluid viscosity in the absence of wall damping; this results in the appearance of a flutter instability. This observation was made for flow over a compliant plate by Carpenter (1984), and may be seen for channel flow with the Grotberg and Reiss (1984) model (*c.f.* below).

The appearance of divergence only in systems with wall damping appears at first sight to contradict the results seen in §2.3, in which irrespective of whether the walls were damped the instability was divergent at onset. This difference is, however, due to another fundamental difference between the systems being considered in §2.3 and above, namely the finite length of the flexible section. Lucey and Carpenter (1992, 1993) addressed this issue when considering flow over a finite length compliant plate, and showed that in the case of a finite geometry there are always end effects that influence the system in the same manner as damping in the infinite-length case.

In all of the analyses thus far considered, a divergence instability is seen at criticality. However, in physical systems flutter is observed; to address this discrepancy, Grotberg and Reiss (1982, 1984) added a hydraulic friction term to the potential flow through a channel to approximate the effect of viscosity. (Grotberg and Shee (1985) showed that this is consistent with the full Orr-Sommerfeld system when viscosity and wall damping are taken to zero and their ratio

is $O(1)$.) They found that the addition of fluid friction results in the reappearance of the flutter instability, and through a weakly non-linear analysis showed also that the bifurcation to flutter is supercritical and hence stable. The recovery of a flutter instability with the addition of viscosity is due to the fact that viscosity stabilizes Type A wall-fluid instabilities (as noted in §2.2) while destabilizing those of Type B. The introduction of wall damping to the inviscid system destabilizes the Type A wave, leading to a divergence instability; the addition of viscosity may restabilize this wave (and destabilize the Type B wave), resulting in an oscillatory instability. The Grotberg and Reiss channel model was reconsidered with the addition of fluid compressibility by Grotberg and Shee (1985), who found generally slight corrections to the incompressible case. To show that the wheezing lung sounds that Grotberg and Davis (1980) first set out to describe are in fact due to flutter of the airway walls, Grotberg and Gavriely (1989) compared the results obtained with the Grotberg and Reiss model with experiments involving flow through flexible tubes, and found good agreement between theory and experiments.

Webster *et al.* (1985) experimentally and theoretically examined flow through a model of the trachea, a three sided duct covered with a compliant tensioned membrane. Their theoretical model was a two-dimensional channel with one compliant boundary; the flow was taken to be potential and the wall undamped. Due to the singular influence of damping on this type of system, the relevance of this analysis to physical situations might be questioned, but they reported good agreement with their experiments.

§2.5 *Additional work on flow over compliant plates*

The possibility of the stabilization of the Blasius boundary layer by a compliant plate was reconsidered by Carpenter and Garrad (Garrad and Carpenter 1982, Carpenter and Garrad 1985,

1986). They considered flow over a flexible plate with linear wall properties, and allowed for the effect of a 'fluid substrate' in a reservoir behind the plate. Garrad and Carpenter (1982) examined a compliant plate of finite length, with an inviscid substrate fluid of infinite depth, and a potential flow with corrections to simulate the effect of a laminar or turbulent boundary layer. Using the Galerkin method, they found for the laminar case a divergence instability, and for the turbulent case flutter. The persistence of the divergence instability here even with the inclusion of viscosity is reasonable, as the flexible surface had finite length, which may promote the divergence instability.

Carpenter and Garrad (1985, 1986) subsequently performed an in depth analysis of the linear stability of the infinite length system both with and without a viscous substrate fluid, considering both the Tollmien-Schlichting and wall-fluid instabilities (in the 1985 and 1986 papers, respectively). Approximate analytical methods were used to examine how different physical effects alter the stability of the different waves, thereby illustrating the behavior of the wave types of Benjamin and Landahl. The linear stability analysis of the TSI was carried out numerically to account for the full effects of viscosity, using a shooting algorithm. For the flutter instability this numerical solution was supplemented by an analytical analysis using Benjamin's (1963) approximation to the pressure fluctuation caused by a boundary layer. They then addressed the question of whether Kramer's (1960) experiments could have shown significant postponement of the transition to turbulence, and concluded that this was in fact a possibility. Their 1985 paper also includes a review of the literature on the theoretical and experimental stability analyses for flow over a flat plate. Other such reviews are those of Gad el Hak (1986) and Riley *et.al.* (1988).

More recently, Carpenter and Gajjar (1990) formulated a general multi-deck asymptotic

theory for the stability of the Type B (travelling wave) flutter instability in flow over a compliant plate of infinite length. This is significantly less computationally intensive than the solution of the full Orr-Sommerfeld system, but is limited to this flutter instability and the case in which the critical layer (where the phase speed of the disturbance becomes equal to the flow speed of the base flow) is distinct from the viscous boundary layer at the wall.

Additional investigations of the linear stability of a flow over a compliant surface are those of Duncan *et.al.* (1985) and Evrensel and Kalnins (1985, 1988). Duncan *et.al.* considered a potential flow with a phase correction to the perturbation pressure to simulate a boundary layer, while Evrensel and Kalnins in 1985 considered a potential flow, and in 1988 a fully viscous profile. The (linear) stability calculations in each case differ from those of Carpenter and Garrad (1985, 1986) primarily in the wall model chosen; these authors consider the wall to be an elastic or viscoelastic solid of finite depth and solve the appropriate equations for the behavior of such a material to determine the wall motion. Pierucci and Morales (1990) considered the equivalent problem for the TSI in plane Poiseuille flow with elastic (undamped) walls, but their conclusions are questionable due to their assumption that the critical wave number remains unchanged with the introduction of wall compliance.

§2.6 Other approaches

In addition to the stability analyses described in the preceding sections, other methods have been used to obtain a better understanding of the nature of the coupling of flow to compliant structures and relevant applications. In this section we briefly review some of these studies.

Walsh *et.al.* (1991) modelled expiratory flow in the trachea with a geometry consisting of two concentric cylinders, the inner of which has an undamped, untethered flexible wall. Using

curved-shell flutter theory with one-dimensional inviscid fluid equations, they considered the axial displacements of the wall to be much larger than the lateral displacements. With these assumptions, they found a long-wave flutter instability.

Brazier-Smith and Scott (1984) considered the linear analysis of an inviscid flow over a temporally forced undamped plate with bending stiffness. As the system is both undamped and forced it is unstable, and the resulting instability was studied to determine whether it is absolute or convective. Carpenter and Garrad (1986) compared their results with those of Brazier-Smith and Scott by calculating the group velocity of the disturbance to the system as the derivative of the phase speed with respect to wave number, and found good agreement. Lucey and Carpenter (1992) presented a similar but numerical analysis for an inviscid flow over a forced compliant plate of finite length. They were concerned exclusively with the divergence instability, which was isolated through consideration of the energy of the system.

A full numerical solution of the Navier Stokes and compliant wall equations was obtained by Domaradzki and Metcalfe (1987) for flow over a flexible plate, and used to determine the nature of the distribution and dissipation of energy for the different wave types of Benjamin and Landahl. For Type A waves the energy dissipation has a local maximum near the wall, while for Type B waves there is little energy activity there. Type A waves are stabilized primarily by the boundary layer region of fluid, while wall dissipation is the main stabilizing factor for Type B waves. These observations are clearly representative of the general characterizations of the given wave types.

Sen and Arora (1988) approached the problem of flow over a compliant wall by using a kinematic formulation of the wall boundary conditions that permits analysis of the flow without specification of the specific material properties of the wall. These properties may then be back

calculated given the wall dynamics. By thus separating the nature of the wall model from the actual analysis of the flow, they proposed that walls with optimum stabilization capabilities could be determined. A general understanding of the instability for flows with compliant boundaries was also the objective of Yeo and Dowling (1987), who reconsidered many of the fundamental stability theorems for inviscid flow over a rigid surface to extend their validity to the case of a compliant wall.

Recently, there have been a few non-linear studies of the TSI for Poiseuille flow in a channel. Rotenberry and Saffman (1990) undertook a weakly non-linear analysis of the instability and derived a Ginzburg-Landau equation for the amplitude of the bifurcating solution. The walls considered were simple elastic membranes (with allowance for damping), and they found that when these are sufficiently flexible the bifurcation to the TSI goes from being subcritical, as is the case for a channel with rigid walls, to supercritical. Rotenberry and Saffman also proved an extension of Squire's theorem for Poiseuille flow in a compliant channel. Rotenberry (1992) considered the same channel system with the addition of tension to the channel walls, and inferred the criticality of the bifurcation from the shape of the curve of disturbance energy as a function of Reynolds number. He concluded that while sufficiently flexible walls may render the bifurcation supercritical, the magnitude of the supercritical branch is in fact very small, so that for finite but small distances from the base Poiseuille solution the bifurcation appears subcritical. Thus wall flexibility does not quantitatively change the character of the TSI.

§2.7 *Conclusions*

These studies show that the effects of wall and fluid damping are significant in determining the nature of the flutter instability, and that their influence is often singular in nature.

Thus our model is developed to accurately include these effects, and is two-dimensional to allow for the effect of transverse variation in the flow speed in the channel (which has not been previously considered in channel studies of the flutter instability). The similarity between previous results for and methods used in the study of more rigid (uncollapsed) pipes and collapsible tubes suggests that the channel model we develop will also be applicable to a wide range of systems, though we are specifically interested in its application to the lung airways and wheezing lung sounds.

CHAPTER 3: MODEL DERIVATION

§3.1 *Derivation of nondimensional equations and boundary conditions*

To model a partially collapsed flexible tube we consider a two-dimensional channel with compliant walls; through this flows an incompressible Newtonian fluid. In this chapter we derive the linear stability equations for this system with a basic state consisting of a flat walled channel and a given laminar flow.

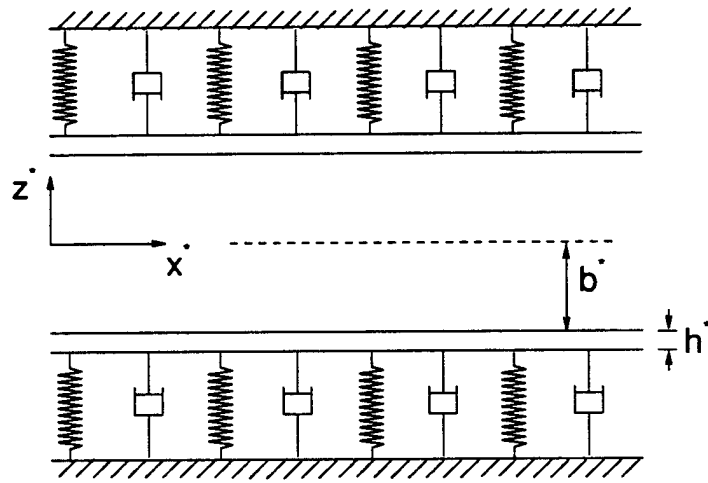


Figure 3.1 Flexible walled channel system. Walls are spring supported and damped, and a coordinate system is fixed to the channel midline; dimensions are as shown.

The system under consideration is shown in figure 3.1. The walls of the channel are damped flexible plates supported by an array of springs attached to a rigid backing; it is assumed that this continuous array of linear springs models the elastance of the tube and the material supporting it. We define a coordinate system centered in the channel with axial and transverse

coordinates x^* and z^* . As indicated, the half channel width is b^* , so that the undisturbed location of the walls is $z^* = \pm b^*$. Denoting the (x^*, z^*) location of a point on the lower wall as $U^* = (U^*, W^*)$, the nonlinear von Kármán plate equations governing the normal and tangential motion of the wall are

$$\begin{aligned} \rho_w^* h^* \frac{\partial^2 W^*}{\partial t^{*2}} + 2\rho_w^* h^* G^* \frac{\partial W^*}{\partial t^*} - \frac{12D^*}{h^{*2}} \left(\frac{\partial U^*}{\partial x^*} \frac{\partial^2 W^*}{\partial x^{*2}} + \frac{\partial^2 U^*}{\partial x^{*2}} \frac{\partial W^*}{\partial x^*} + \left(\frac{\partial W^*}{\partial x^*} \right)^2 \frac{\partial^2 W^*}{\partial x^{*2}} \right) + \\ D^* \frac{\partial^4 W^*}{\partial x^{*4}} - T^* \frac{\partial^2 W^*}{\partial x^{*2}} - E^* (W^* + b^*) + (S^{*N} - S_{EXT}^{*N}) = 0 \end{aligned} \quad (3.1)$$

and

$$\begin{aligned} \rho_w^* h^* \frac{\partial^2 U^*}{\partial t^{*2}} + 2\rho_w^* h^* H^* \frac{\partial U^*}{\partial t^*} - \frac{12D^*}{h^{*2}} \left(\frac{\partial^2 U^*}{\partial x^{*2}} + \right. \\ \left. \frac{\partial^2 W^*}{\partial x^{*2}} \frac{\partial W^*}{\partial x^*} \right) + (S^{*T} - S_{EXT}^{*T}) = 0 \end{aligned} \quad (3.2)$$

(Sapir and Reiss 1979), where ρ_w^* is the density of the wall material, h^* the wall thickness, G^* and H^* the coefficients of normal and tangential damping in the wall, D^* the flexural rigidity of the plate, T^* the imposed longitudinal tension, E^* the spring constant (elastance) of the spring supports, and S^{*N} and S^{*T} the normal and tangential stresses on the wall, respectively, with subscript 'ext' indicating stresses acting from the region external to the wall. As written, these equations apply to the lower wall of the channel. In the development that follows, we for simplicity treat only the equations for the lower wall; in all cases similar equations apply at the upper wall. In equations (3.1, 2) and those following, a superscripted asterisk indicates a dimensional variable.

The motion of the fluid is given by the Navier-Stokes equations, in vector form

$$\rho^* \left(\frac{\partial \mathbf{u}^*}{\partial t^*} + \mathbf{u}^* \cdot \nabla^* \mathbf{u}^* \right) = -\nabla^* p^* + \nu^* \nabla^{*2} \mathbf{u}^* \quad (3.3)$$

and

$$\nabla^* \cdot \mathbf{u}^* = 0 \quad (3.4)$$

where $\mathbf{u}^* = (u^*, w^*)$ is the fluid velocity vector in the x^*-z^* plane, ∇^* the two-dimensional (2D) gradient operator, ∇^{*2} the 2D laplacian, and ρ^* , p^* and ν^* the fluid density, pressure and viscosity, respectively. The fluid must satisfy the kinematic and no slip conditions at the wall,

$$\mathbf{n} \cdot \mathbf{u}^* = \mathbf{n} \cdot \frac{\partial \mathbf{U}^*}{\partial t^*} \quad \text{and} \quad \boldsymbol{\tau} \cdot \mathbf{u}^* = \boldsymbol{\tau} \cdot \frac{\partial \mathbf{U}^*}{\partial t^*}, \quad (3.5)$$

where \mathbf{n} and $\boldsymbol{\tau}$ are unit vectors normal and tangential to the wall. Hereafter we denote partial differentiation with subscripts.

Equations (3.1-5) are nondimensionalized using a velocity scale \hat{u} , length scale L , time scale $T_0 = L / \hat{u}$ and pressure scale $\pi = \rho^* \hat{u}^2$; we generally take $L = b^*$ (the half channel width) and $\hat{u} = (E^* b^* / \rho)^{1/2}$, an elastic wave speed of the wall. Introducing the nondimensional variables $\mathbf{U} = (U, W) = \mathbf{U}^* / L$, $\mathbf{u} = (u, w) = \mathbf{u}^* / \hat{u}$, $t = t^* / T_0$, $(x, z) = (x^*, z^*) / L$ and $p = p^* / \pi$ (and noting that the nondimensional stresses are $S^{N,T} = S^{*N,T} / \pi$), equations (3.1) and (3.2) become

$$\begin{aligned} MW_{tt} + 2GW_t - d(U_x W_{xx} + U_{xx} W_x + (W_x)^2 W_{xx}) \\ + BW_{xxx} - TW_{xx} + E(W + \frac{b^*}{L}) + (S^N - S_{EXT}^N) = 0 \end{aligned} \quad (3.6)$$

and

$$MU_{tt} + 2HU_t - d(U_{xx} + W_{xx} W_x) + (S^T - S_{EXT}^T) = 0. \quad (3.7)$$

Nondimensional parameters appearing in (3.6) and (3.7) are $M = (\rho_w^* h^* / \rho^* L)$, $G = M L G^* / \hat{u}$, $H = M L H^* / \hat{u}$, $d = 12 D^* / h^{*2} L \rho^* \hat{u}^2$, $B = D^* / L^3 \rho^* \hat{u}^2$, $T = T^* / L \rho^* \hat{u}^2$, and $E =$

$E^* L / \rho^* \hat{u}^2$ ($= 1$ for the scaling indicated above). These parameters are respectively the wall to fluid mass ratio, and the non-dimensional wall characteristics: normal and tangential damping, bending stiffness, flexural rigidity, imposed longitudinal tension, and elastance.

The stresses in (3.6) and (3.7) are found from consideration of the fluid stress tensor $\underline{\sigma}$, in terms of which $S^N = \mathbf{n} \cdot \underline{\sigma} \cdot \mathbf{n}$ and $S^T = \boldsymbol{\tau} \cdot \underline{\sigma} \cdot \mathbf{n}$. Assuming deflections of the plate to be small, these are

$$S^N = -p + \left(\frac{2w_z}{R_w} \right) \quad \text{and} \quad S^T = \frac{(u_z + w_x)}{R_w}, \quad (3.8)$$

where $R_w = \hat{u} L / \nu$ is the Reynolds number. We have chosen the notation R_w to emphasize that this Reynolds number, due to our choice of \hat{u} as a wall elastic wave speed, is related to the wall elastance.

It is convenient to rewrite the Navier-Stokes equations (3.3) and (3.4) in stream function form to eliminate the fluid pressure. Nondimensionalizing as above and introducing a stream function Ψ , where $(u, w) = (\Psi_z, -\Psi_x)$ (so that the continuity equation (3.4) is automatically satisfied), equation (3.3) becomes the vorticity equation

$$\nabla^2 \Psi_t - \frac{1}{R_w} \Delta^2 \Psi = \Psi_x \nabla^2 \Psi_z - \Psi_z \nabla^2 \Psi_x, \quad (3.9)$$

where Δ^2 is the two-dimensional biharmonic operator, $(\partial_x^4 + 2 \partial_x^2 \partial_z^2 + \partial_z^4)$. The unit vectors \mathbf{n} and $\boldsymbol{\tau}$ in (3.5) are

$$\mathbf{n} = \frac{1}{(W_x^2 + 1)^{1/2}} (-W_x, 1) \quad \text{and} \quad \boldsymbol{\tau} = \frac{1}{(W_x^2 + 1)^{1/2}} (1, W_x), \quad (3.10)$$

so that on introduction of the stream function, the kinematic and no slip conditions (3.5) become

$$\begin{aligned} -W_x \Psi_z - \Psi_x &= -W_x U_t + W_t \quad \text{and} \\ \Psi_z - W_x \Psi_x &= U_t + W_x W_t, \quad \text{at } z = \pm 1. \end{aligned} \quad (3.11)$$

§3.2 System linearization and simplification

A basic solution for the system defined by equations (3.6-7), (3.9) and (3.11) has flat walls ($U = 0$, $W = \pm 1$) and a given stream function Ψ_0 corresponding to the flow profile being considered (discussed below). Implicit in this base state is the assumption of a pressure gradient external to the flexible walls to maintain the flat walled configuration. We assume that the base flow is parallel, that is, that Ψ_0 is a function of z only, and write $d\Psi_0 / dz = u_0(z)$, where $u_0(z)$ is the base axial flow velocity in the channel.

To determine the stability of this base state we use linear stability theory and introduce perturbations (U', W') and ψ to the base wall position and stream function respectively. In the usual manner, we write these disturbance quantities in normal modes, so that

$$\begin{aligned} (U, W) &= (0, -1) + (U', W') = (0, -1) + (\chi, \omega) \exp(ik(x - ct)) \\ \Psi &= \Psi_0 + \psi' = \Psi_0 + \varphi(z) \exp(ik(x - ct)). \end{aligned} \quad (3.12)$$

Plugging these into the governing equations and linearizing in perturbation quantities, linearized stability equations are obtained. The vorticity equation (3.9) becomes the Orr-Sommerfeld equation,

$$k(u_0 - c)(\varphi'' - k^2\varphi) - k u_0'' \varphi + \frac{i}{R_w}(\varphi^{iv} - 2k^2\varphi'' + k^4\varphi) = 0, \quad (3.13)$$

and the kinematic and no slip conditions (3.10) become

$$-ikc\chi = \varphi' + u_0'\omega \quad \text{and} \quad \varphi = (c - u_0)\omega, \quad (3.14)$$

where u_0 and φ are, after linearization, evaluated at $z = \pm 1$. Using (3.14) to eliminate the wall

variables from (3.6) and (3.7), we obtain after substituting (3.8) for the fluid stresses (and eliminating the pressure in (3.8) using (3.3))

$$(-(kc)^2 M - 2ikcG + Bk^4 + Tk^2 + E)k\phi + k(c - u_0)(u_0'\phi + (c - u_0)\phi') - \frac{i(c - u_0)}{R_w}(\phi''' - 3k^2\phi') = 0 \quad (3.15)$$

and

$$(-(kc)^2 M - 2ikcH + dk^2)((u_0 - c)\phi' - \phi u_0') - \frac{ikc(u_0 - c)}{R_w}(\phi'' + k^2\phi) = 0. \quad (3.16)$$

Again, consistent with linearization, (3.15) and (3.16) are evaluated at $z = -1$.

By assuming disturbances to be divisible into 'symmetric' and 'antisymmetric' modes, we may restrict attention to the lower half of the channel. For symmetric disturbances the channel walls oscillate out of phase with one another (in a varicose shape) so that the disturbance stream function must satisfy conditions of no cross flow at the midline; for antisymmetric disturbances the walls are in phase (a sinuous shape) and we require no axial flow at the midline. These conditions are

$$\phi = \phi'' = 0 \quad (\text{symmetric}) \quad \text{or} \quad \phi' = \phi''' = 0 \quad (\text{antisymmetric}). \quad (3.17)$$

Equation (3.13) with boundary conditions (3.15-17) constitutes an eigenvalue problem for the disturbance stream function ϕ and eigenvalue c . The real and imaginary parts of c are the phase speed and growth rate, respectively, of the disturbance; instability thus sets in when the imaginary part of c becomes positive, and it is of interest to determine the conditions for which this occurs. The sign of the real part of c determines whether the disturbance travels upstream (negative sign) or downstream (positive sign), and the product of the wave number k and the real

part of c (over 2π) gives the frequency of the oscillations. For simplicity we assume that tangential wall inertia and damping may be neglected, that is, that we may discard the first two terms in the tangential boundary condition (3.16); comparison of the numerical solution with the resulting modified boundary condition with those using the full condition shows the two to be indistinguishable. If the tangential stress is also omitted from equation (3.16) we recover the no slip condition used by Benjamin (1960) and others, which does not include the effect of horizontal wall motion.

§ 3.3 *Specification of the base flow profile*

To complete the specification of the Orr-Sommerfeld system derived in §3.2, a base flow profile must be chosen. As a solution for flow in a channel, this will be either a developing (boundary layer) or fully-developed (Poiseuille) flow; we are interested in modelling short tubes, and so are concerned with the developing flow profile. However, there is no closed form solution for the corresponding stream function; as a result there are a large number of approximate solutions. These may be divided into four general categories: integral methods (Schiller 1922; Campbell and Slattery 1963); models linearizing the inertial terms in the Navier-Stokes equations (Langhaar 1942; Sparrow *et.al.* 1964); numerical solutions of the boundary layer (Bodoia and Osterle 1961) or full equations (Brandt and Gillis 1964; Wang and Longwell 1964); and axially patched or asymptotic solutions (Schlichting 1934; Van Dyke 1970; Wilson 1970, 1971). A good summary of these categories and solution methods appears in Schmidt and Zeldin (1969).

We approximate the developing profile in two ways: first, by using a uniform (plug) profile, and second, by solving the boundary layer equations using either finite difference or perturbation methods. For the flow regimes in which we are interested the flow is uniform over

most of the channel, with nonuniformity being restricted to a small region (boundary layer) near the wall. The flow is thus quantitatively similar to a plug flow over most of the channel width, so that it may be hoped that meaningful predictions may be obtained from the analysis of this much simpler flow; this analysis appears in Chapter 4. Of course, the results so obtained must be evaluated carefully, as the plug flow does not satisfy the no slip conditions at the wall.

Our finite difference solution uses a second order scheme with a nonuniform grid to solve the boundary layer equations; full details of the method appear in Appendix A. This solution is able to provide the flow profile at any location in the channel up to and including the point of fully developed flow, but more difficult to use in the Orr-Sommerfeld system as any change in the velocity of the base flow requires that the flow profile be recalculated. However, the numerically determined profile is useful for evaluating the perturbation solution, which we use in our stability calculations.

We follow Schlichting (1934) in the development of a perturbation solution for developing channel flow. A uniform flow is assumed at the channel inlet that, as it progresses down the channel, assumes a profile with growing boundary layers at either wall. For short distances from the channel inlet these boundary layers form in the same manner as the Blasius solution for flow over a flat plate, with the caveat that mass conservation requires that the flow in the central region of the channel accelerate to compensate for the decreased flow at the walls. Thus for the upstream portion of the channel the difference between the channel and flat plate geometries may be incorporated as a perturbation to the Blasius profile.

We therefore model the channel flow using the steady boundary layer equations, in stream-function form

$$\Psi_y^* \Psi_{x^*y^*} - \Psi_x^* \Psi_{y^*y^*} = \dot{U}^* \dot{U}_x^* + v^* \Psi_{y^*y^*y^*} \quad (3.18)$$

Here ψ^* is the dimensional form of the base flow stream function Ψ_0 , $\dot{U}^*(x^*)$ is the velocity field outside of the boundary layer and a new transverse coordinate $y^* = b^* + z^*$ has been introduced to mimic the transverse coordinate usually used for flow over a single plate. The stream function ψ^* is written as a perturbation expansion that will at leading order recover the Blasius solution,

$$\psi^* \sim S^* b^* (\epsilon f_1(\eta) + \epsilon^2 f_2(\eta) + \epsilon^3 f_3(\eta) + \dots), \quad (3.19)$$

where $\epsilon \equiv (v^* x^* / b^{*2} S^*)^{1/2}$, S^* is the velocity of the initial (uniform) flow, and $\eta = y^* / (\epsilon b^*)$ is the similarity variable for flow over a flat plate. The free stream velocity $\dot{U}^*(x)$ may be determined from mass conservation, as follows. For the flow rate at the inlet to be equal to that at any point downstream, we must have $S^* b^* = \dot{U}^*(b^* - \delta_1^*)$, where δ_1^* is the displacement thickness of the boundary layer. By definition

$$\delta_1^* \dot{U}^* = \int_0^{b^*} (\dot{U}^* - u^*) dy^* = \epsilon b^* \int_0^{\eta_1} (\dot{U}^* - S^* (f_1' + \epsilon f_2' + \dots)) d\eta, \quad (3.20)$$

where η_1 is a point outside of the boundary layer. Using the requirement for constant flow rate to eliminate δ_1^* from (3.20), we obtain, after a little rearranging,

$$\dot{U}^* \sim S^* (1 + \epsilon K_1 + \epsilon^2 K_2 + \dots), \quad \text{where} \quad (3.21)$$

$$K_n = K_{n-1} \eta_1 - f_n(\eta_1) \quad (K_0 \equiv 1).$$

Using the expansions for ψ^* and \dot{U}^* in equation (3.18), we obtain on collecting powers of ϵ a series of problems for the f_n , the first three of which are

$$\begin{aligned} 2f_1''' + f_1 f_1'' &= 0, \\ 2f_2''' + f_1 f_2'' - f_1' f_2' + 2f_1'' f_2 &= -K_1, \quad \text{and} \\ 2f_3''' + f_1 f_3'' - 2f_1' f_3' + 3f_1'' f_3 &= -2f_2 f_2'' + (f_2')^2 - K_1^2 - 2K_2. \end{aligned} \quad (3.22)$$

Boundary conditions for (3.22) are $f_n(0) = f'_n(0) = 0$ and $f'_n \rightarrow K_{n-1}$ as $\eta \rightarrow \infty$, which require that ψ^* satisfy the no slip condition at the channel wall and match with the outer flow \dot{U}^* at the upper edge of the boundary layer.

The first of equations (3.22) is that for Blasius flow over a plate; this and the problems for the correction terms are solved in a straightforward manner using a multiple shooting routine (DBVPMS from IMSL). The base flow u_0 is then given by

$$u_0(z; x) \sim S (f'_1(\eta) + \epsilon f'_2(\eta) + \epsilon^2 f'_3(\eta) + \dots), \quad (3.23)$$

where by definition, $\epsilon(x) = x^{1/2} / (R_w S)$ and $\eta = (z + 1) / \epsilon(x)$. In the derivation of the Orr-Sommerfeld system, u_0 was assumed to be a function of z only; we thus evaluate ϵ for a fixed value of $x = x_0$ to eliminate the dependence on the axial coordinate. Because ϵ varies as $x_0^{1/2}$ it is then necessary to impose a downstream limit on x_0 to maintain the validity of the perturbation solution for u_0 . Following Schlichting we choose to restrict x_0 so that ϵ is sufficiently small that the successive terms of the solution for u_0 remain well ordered, that is, $f'_1 > \epsilon f'_2 > \epsilon^2 f'_3$. This requires that ϵ be less than 0.1455, or by extension that we choose $x_0 < (0.1455)^2 R_w S$. If additional terms are included in the expansion for u_0 the downstream constraint on x_0 becomes more severe. (e.g., Collins and Schowalter 1962 cite $\epsilon < 0.0707$ ($x_0 < 0.005 R_w S$) for a seven term expansion.)

The solution (3.23), normalized by the magnitude of S , is shown in figure 3.2. In 3.2a u_0 and f'_1 (the Blasius solution) are plotted as functions of z and compared with the finite difference solution to the boundary layer equations, for a representative set of parameter values. The agreement between the perturbation and numerical solutions is seen to be good. In 3.2b the values of f'_1 , $\epsilon f'_2$ and $\epsilon^2 f'_3$ are shown for the same choice of parameters.

The advantage of using the perturbation solution for u_0 (3.23) arises from its formulation

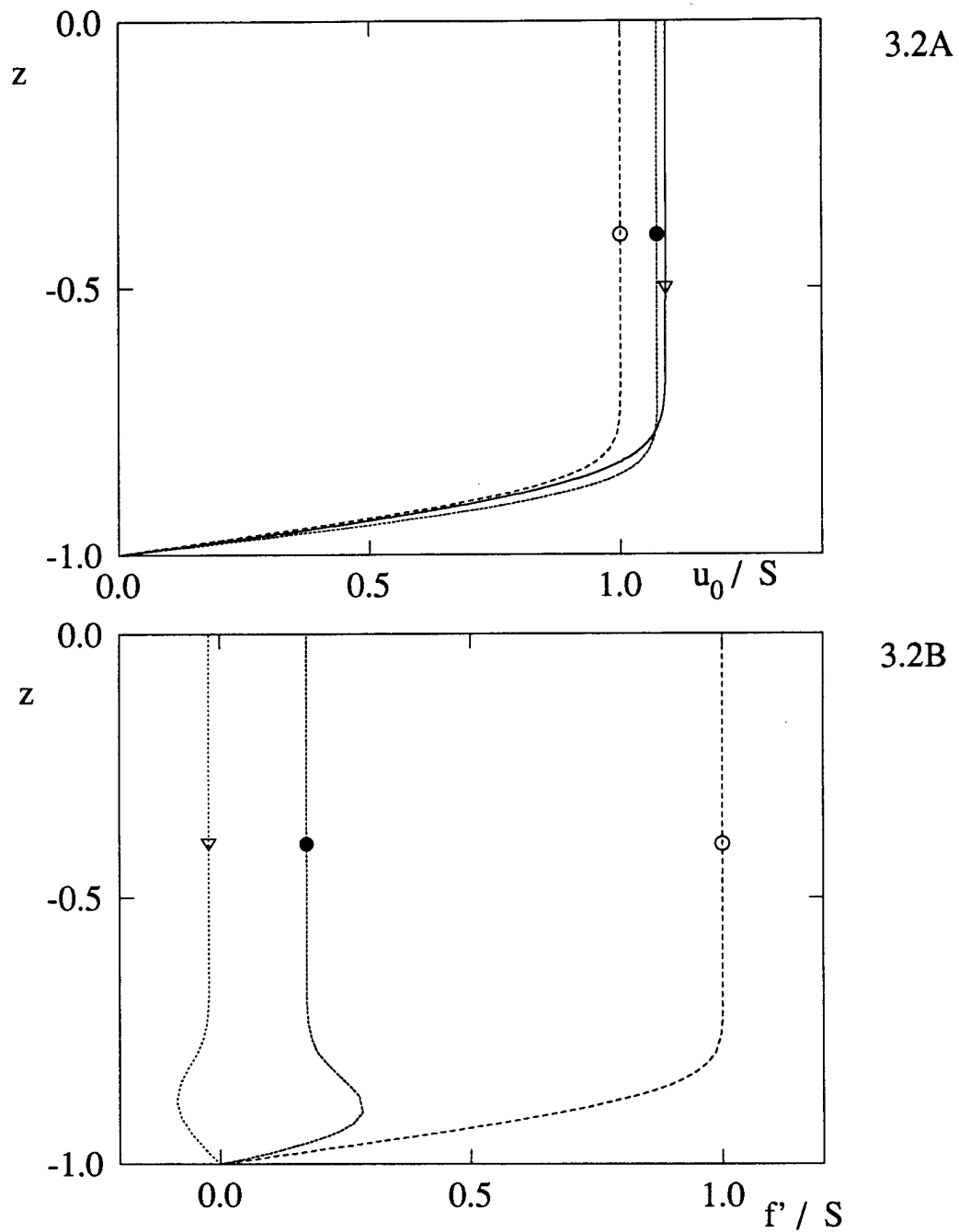


Figure 3.2 Solutions for developing channel flow (3.2A): ∇ finite difference;
 \bullet perturbation solution. Blasius profile (\circ) is shown for comparison.
 3.2B shows the different terms in the perturbation solution: \circ f_1' ;
 \bullet $\epsilon f_2'$; ∇ $\epsilon^2 f_3'$. $x_0=1$, $R_w=2230$, $S=0.22$.

in terms of the Blasius similarity variable. With the velocity profile tabulated as a function of this independent variable, the value of u_0 may be found for any given position (x_0, z) by calculating the value of η corresponding to that point (at the Reynolds number and flow speed being considered) and then interpolating using a cubic spline routine (from Press *et.al.* 1990) to find the corresponding value for u_0 . Solutions to the stability problem (3.13), (3.15-17) with the perturbation solution for u_0 are obtained analytically for long waves and numerically for disturbances with arbitrary wavelengths in Chapter 5.

CHAPTER 4: ASYMPTOTIC AND EXACT SOLUTIONS FOR A PLUG FLOW BASE STATE

§4.1 *Introduction and equations*

The analytical study of the Orr-Sommerfeld equation for non-uniform base velocity profiles is a difficult task even for the case of a system with rigid walls, as it involves the solution of a non-constant coefficient, complex valued, fourth order eigenvalue problem. To facilitate the development of an analytical solution, we therefore choose to approximate the developing flow profile with a uniform (plug) flow, as indicated in §3.3. In this case, it is possible to solve the Orr-Sommerfeld system using the method of matched asymptotic expansions to obtain an explicit solution for the eigenfunction ϕ and eigenvalue c . As the problem with plug flow has constant coefficients, it is also possible to obtain an exact solution, which determines the eigenfunction and eigenvalues implicitly. We present the matched asymptotic and exact solutions in §4.2 and §4.3, respectively, and show results for both cases in §4.4.

For a plug base flow with nondimensional flow speed S , the Orr-Sommerfeld equation (3.13) becomes

$$k(S - c)(\phi'' - k^2\phi) + \frac{i}{R_w}(\phi^{(iv)} - 2k^2\phi'' + k^4\phi) = 0. \quad (4.1)$$

At the wall ($z = -1$), boundary conditions on ϕ are (3.15) and (3.16), or

$$\begin{aligned} &(-(kc)^2 - 2ikcG + Bk^4 + Tk^2 + 1)k\phi + \\ &(S - c)^2 k\phi' + \frac{i(S - c)}{R_w}(\phi''' - 3k^2\phi') = 0 \end{aligned} \quad (4.2)$$

and

$$dk\phi' + \frac{ic}{R_w}(\phi'' + k^2\phi) = 0, \quad (4.3)$$

and at the midline ($z = 0$) ϕ must satisfy symmetry or antisymmetry conditions (3.17),

$$\phi = \phi'' = 0 \quad (\text{symmetric}), \quad \text{or} \quad \phi' = \phi''' = 0 \quad (\text{antisymmetric}). \quad (4.4)$$

In the equations following, we denote the term $-(kc)^2 M - 2ikcG + Bk^4 + Tk^2 + 1$ appearing in (4.1) as Δ , a function of k and c .

§4.2 Asymptotic solution

The plug base flow introduced in §4.1 is valid in the limit of Reynolds number $R_w \rightarrow \infty$, so that it is appropriate to expand ϕ and c in power series in the small parameter $\epsilon \equiv R_w^{-1/2}$, as

$$\begin{aligned} \phi &\sim \phi_0 + \epsilon\phi_1 + \epsilon^2\phi_2 + \dots \\ c &\sim c_0 + \epsilon c_1 + \epsilon^2 c_2 + \dots \end{aligned} \quad (4.5)$$

Plugging (4.5) into (4.1) and letting ϵ go to zero, we obtain the leading order problem

$$k(S - c_0)(\phi_0'' - k^2\phi_0) = 0 \quad (4.6)$$

with midline boundary conditions (4.4). Because in the limit $\epsilon \rightarrow 0$ the two highest derivatives in (4.1) are lost, the perturbation is singular and it is not possible for this reduced problem to satisfy all of the boundary conditions. A boundary layer is introduced to admit the effect of viscosity at the wall, so that the solution to the outer problem must satisfy only the midline conditions; the inner (boundary layer) solution satisfies the conditions at the wall and matches to the outer solution at the edge of the boundary layer. Equation (4.6) is the Raleigh equation (see, *e.g.*, Drazin and Reid 1981); to consider inviscid stability we would require that ϕ solve this and the first of either the symmetric or antisymmetric boundary conditions (4.4), and then demand that

the normal boundary condition at the wall (4.2) be satisfied.

The solution of (4.6) when the wave number k is non-zero and the leading order phase speed c_0 is not equal to the flow speed S is, up to an arbitrary multiplicative constant,

$$\varphi_0 = \sinh(kz) \quad \text{or} \quad \varphi_0 = \cosh(kz) \quad (4.7)$$

(for symmetric or antisymmetric disturbances, respectively). If the wave number k or the difference $S - c$ is small ($O(\epsilon^2)$), it is no longer possible to construct an asymptotic solution differing significantly from the exact solution presented in §4.3, and we thus do not deal with these possibilities here (*c.f.* §4.3). The solution (4.7) is in fact the exact solution to (4.1) for the region away from the wall, so that all correction terms φ_n ($n > 0$) are identically zero.

To find the inner solution, a new independent variable ζ is introduced to stretch the boundary layer near the wall. With the small parameter $\delta(\epsilon)$ defining the boundary layer width, ζ is defined by $\zeta = (1 + z) / \delta(\epsilon)$. We choose δ to retain the highest derivative term in the Orr-Sommerfeld equation as ϵ tends to zero, which requires $\delta(\epsilon) = \epsilon$; this choice in fact motivates the use of ϵ as our expansion parameter. Rewriting (4.1) in terms of the inner variable ζ and letting $\Phi(\zeta) = \varphi(z)$, we obtain

$$(\Phi^{(iv)} - ik(S - c)\Phi'') + \epsilon^2 k^2(ik(S - c)\Phi - \Phi'') + \epsilon^4 k^4 \Phi = 0. \quad (4.8)$$

Similarly rewriting the wall boundary conditions (4.2) and (4.3) gives

$$(k(c - S)^2 \Phi' - i(c - S)\Phi''') + \epsilon k \Phi \Delta + 3i\epsilon^3 k^2(c - S)\Phi' = 0 \quad (4.9)$$

and

$$dk\Phi' + \epsilon ic\Phi'' + \epsilon^3 ik^2 c\Phi = 0, \quad (4.10)$$

both at $\zeta = 0$. These give two boundary conditions on Φ ; the inner solution must also match with

the outer solution ϕ at the edge of the boundary layer. This matching condition is formulated mathematically below.

Expanding Φ in powers of ϵ as

$$\Phi \sim \Phi_0 + \epsilon \Phi_1 + \epsilon^2 \Phi_2 + \dots \quad (4.11)$$

and introducing this and the expansion for c (4.5) into the inner equation and boundary conditions, a series of problems for Φ_n ($n = 0, 1, \dots$) are found at successive orders in ϵ . At leading order,

$$\mathcal{L}\Phi_0 = 0, \quad \text{where} \quad \mathcal{L} \equiv (S - c_0) \frac{d^4}{dz^4} - i k (S - c_0)^2 \frac{d^2}{dz^2}, \quad (4.12)$$

with boundary conditions

$$R_1 \Phi_0 = 0, \quad \text{where} \quad R_1 \equiv k(c_0 - S) \frac{d}{dz} - i \frac{d^3}{dz^3}, \quad \text{at} \quad \zeta = 0, \quad (4.13)$$

and

$$dk\Phi_0'(0) = 0. \quad (4.14)$$

Equation (4.12) is homogeneous with constant coefficients, and has the general solution

$$\Phi_0 = a_{01} + a_{02}\zeta + a_{03}e^{\beta_- \zeta} + a_{04}e^{\beta_+ \zeta}, \quad (4.15)$$

where $\beta_{\pm} \equiv \pm (ik(S - c_0))^{1/2}$. To match with the outer solution we use the method of intermediate limits (Kevorkian and Cole 1981) and introduce the intermediate variable $\xi = (1 + z)/\eta$ (where $\epsilon |\ln \epsilon| \ll \eta(\epsilon) \ll 1$, with $\eta(\epsilon) \rightarrow 0$ as $\epsilon \rightarrow 0$). Rewriting (4.15) and (4.7) in terms of ξ and then reexpanding (4.7) for small η , we obtain

$$\Phi_0 = a_{01} + a_{02} \frac{\eta \xi}{\epsilon} + a_{03} e^{\beta \cdot \frac{\eta \xi}{\epsilon}} + a_{04} e^{\beta \cdot \frac{\eta \xi}{\epsilon}} \quad \text{and} \quad (4.16)$$

$$\Phi_0 = \gamma(k) - \eta k \xi \gamma'(k) + \frac{1}{2} (\eta k \xi)^2 \gamma''(k) + \dots,$$

where for notational convenience the term $\gamma(k) = -\sinh(k)$ or $\cosh(k)$ (for symmetric or antisymmetric disturbances, respectively) has been introduced. The appropriate matching condition is then

$$\lim_{\substack{\epsilon \rightarrow 0 \\ \xi \text{ fixed}}} (\Phi - \phi) = 0, \quad (4.17)$$

which requires that $a_{01} = \gamma(k)$ and $a_{02} = a_{04} = 0$. The tangential boundary condition (4.14) then demands that the constant a_{03} also be zero, so that

$$\Phi_0 = \gamma(k). \quad (4.18)$$

The normal boundary condition (4.13) is trivially satisfied by (4.18), and the eigenvalue c_0 remains undetermined; the leading order dispersion relation is found at $O(\epsilon)$.

With (4.18), we have at $O(\epsilon)$

$$\mathcal{L} \Phi_1 = 0, \quad (4.19)$$

$$R_1 \Phi_1 = -\Delta_0 k \gamma, \quad (4.20)$$

(where $\Delta_0 = \Delta(k, c_0)$), and

$$dk \Phi_1'(0) = 0. \quad (4.21)$$

Equation (4.19) for Φ_1 is the same as (4.12) for Φ_0 , so that, after applying the first order matching condition

$$\lim_{\substack{\epsilon \rightarrow 0 \\ \zeta \text{ fixed}}} \frac{1}{\epsilon} (\Phi - \phi) = 0 \quad (4.22)$$

and the tangential boundary condition (4.21) we find

$$\Phi_1 = -k\gamma'(k)\zeta + \frac{k\gamma'(k)}{\beta_-} e^{\beta_- \zeta}. \quad (4.23)$$

The normal boundary condition (4.20) then becomes after a little algebraic manipulation a quadratic in c_0 which may be solved to give the leading order dispersion relation

$$c_0 = \frac{S - iGP(k)}{1 + MkP(k)} \pm \frac{1}{1 + MkP(k)} \left[(S - iGP(k))^2 - \frac{(1 + MkP(k))(S^2 - (Bk^4 + Tk^2 + 1)P(k))}{k} \right]^{1/2}. \quad (4.24)$$

Here $P(k)$ is defined by $P(k) \equiv \gamma(k) / \gamma'(k)$ ($= \tanh(k)$ or $\coth(k)$ for symmetric and antisymmetric disturbances, respectively). As the limit of ϵ going to zero corresponds to the limit of no viscosity, (4.24) is simply the inviscid dispersion relation for the problem (see, *e.g.* Grotberg and Reiss 1984, setting their viscous correction f to zero).

To find the first (viscous) correction to this dispersion relation it is necessary to continue to order ϵ^2 . Using the expressions for Φ_0 and Φ_1 , (4.18) and (4.22), and collecting terms of $O(\epsilon^2)$, Φ_2 must satisfy the inhomogeneous equation

$$\mathcal{L}\Phi_2 = ik^2 c_1 \gamma' \beta_- e^{\beta_- \zeta} + (2k^2 - ik^3(S - c_0))\gamma \quad (4.25)$$

with boundary conditions

$$R_1 \Phi_2 = \frac{ic_1 k \gamma'}{\beta_-^2} + \Delta_0 \frac{k^3 \gamma'}{\beta_-} + 2k^3 c_1 (Mk c_0 + iG)\gamma \quad (4.26)$$

and

$$dk\Phi_2'(0) = -ikc_0\gamma'\beta_- . \quad (4.27)$$

A particular solution for (4.25) is found using the method of undetermined coefficients to be

$$\Phi_{2p} = -\frac{ik^2c_1\gamma'(k)}{2\beta_-^2}\zeta e^{\beta_-\zeta} + \frac{1}{2}k^2\zeta^2\gamma(k), \quad (4.28)$$

so that, after matching and applying (4.27) as at earlier orders,

$$\Phi_2 = \left(\frac{ik^2c_1\gamma'(k)}{2\beta_-^3} - \frac{ic_0\gamma'(k)}{d}\right)e^{\beta_-\zeta} - \frac{ik^2c_1\gamma'(k)}{2\beta_-^2}\zeta e^{\beta_-\zeta} + \frac{1}{2}k^2\zeta^2\gamma(k). \quad (4.29)$$

Inserting (4.29) into the normal boundary condition (4.26) gives the first correction to the dispersion relation,

$$c_1 = \frac{M(kc_0)^2 + 2ikc_0G - (Bk^4 + Tk^2 + 1)}{2\beta_-(S - (MkP(k) + 1)c_0 - iGP(k))}. \quad (4.30)$$

Recalling that $\beta_- = -(ik(S - c_0))^{1/2}$, it appears at first sight that this expression is singular as S approaches c_0 . However, because of the definition of c_0 (4.24), in this case the numerator of (4.30) goes to zero more rapidly than $(S - c_0)^{1/2}$, and there is no singularity. A singularity may still arise if the remaining term in the denominator, $S - (MkP(k) + 1)c_0 - iGP(k)$, vanishes, which for $G=0$ (an undamped wall) and c_0 strictly real occurs as the flow speed S approaches the value $(MkP(k) + 1)c_0$. The leading order dispersion relation is inviscid, so that when there is no wall damping c_0 will in fact be real valued until the onset of instability, and the denominator may thus be expected to go to zero for some value of flow speed. When wall damping is included, as it will be in all physical applications, this term becomes complex valued, so that it is unlikely that it will completely vanish. For small wall damping, however, the imaginary part

of c_0 is small, and the imaginary part of this term will also be small; thus for lightly damped walls the denominator may become sufficiently small for c_1 to become $O(\epsilon^{-1})$ and the asymptotic expansion may thus break down.

Because the results for the asymptotic solution developed in this section and those for the exact solution in §4.3 are similar, we defer further discussion of the dispersion relation (4.24, 4.30) until §4.4.

§4.3 *Exact solution*

For plug flow the Orr-Sommerfeld equation (4.1) has constant coefficients, so that an exact solution may be obtained in terms of exponentials. Two of the four solutions are those of the inviscid (outer) solution derived above, $\sinh(kz)$ and $\cosh(kz)$ (which are appropriate for symmetric and antisymmetric disturbances, respectively). To determine the remaining two (viscous) solutions, let $\phi = e^{mkz}$; inserting this into (4.1) gives

$$k^3(S - c)(m^2 - 1) + \frac{i}{R_w} k^4(m^4 - 2m^2 + 1) = 0. \quad (4.31)$$

Recognizing that $m = \pm 1$ correspond to the inviscid solutions already isolated, and assuming $k \neq 0$ (we return to this possibility below), the general solution for ϕ is then given by

$$\phi = A_1 g(kz) + A_2 g(kmz), \quad \text{where} \quad m^2 = 1 + \frac{iR_w}{k}(S - c), \quad (4.32)$$

and we have taken $g(x) = \sinh(x)$ or $\cosh(x)$ according to whether symmetric or antisymmetric disturbances are being considered.

For simplicity of analysis, we assume that the tangential boundary condition at the wall may be replaced by that corresponding to no horizontal motion, $(u_0(-1) - c)\phi' - u_0'(-1)\phi = 0$ (c.f.

§3.2), as this assumption makes little difference to the solution obtained. (This is verified with the numerical solution of the full system formulated in chapter 5.) Application of this condition and the normal wall boundary condition (4.2) yields a second order linear homogeneous system for the coefficients A_1 and A_2 ,

$$\begin{bmatrix} g(-k)\Delta & g(-km)\Delta - (S-c)^2 km g'(-km) \\ (S-c)g'(-k) & (S-c)m g'(-km) \end{bmatrix} \begin{bmatrix} A_1 \\ A_2 \end{bmatrix} = 0. \quad (4.33)$$

To obtain (4.33) the relation $g'''(kx) = k^2 g'(kx)$ has been used. The eigenvalue c must be chosen to zero the determinant of the coefficient matrix on the left hand side, which gives the dispersion relation

$$km(S-c)g'(-km)g'(-k) \times \left(\Delta \left[\frac{P(-km)}{km} - \frac{P(-k)}{k} \right] - (S-c)^2 \right) = 0. \quad (4.34)$$

In (4.34), as in the asymptotic solution, $P(x)$ has the value $\tanh(x)$ or $\cotanh(x)$ for symmetric or antisymmetric disturbances. Solutions of this dispersion relation are $c = S$, $c = S - i k \text{Re}^{-1}$, and c chosen to zero the parenthesized term in the relation. The first two of these possibilities always yield stability, so that it is the last that is of interest. Values of c zeroing the parenthesized term are found in a straightforward manner using a numerical root finder (DNEQNF from IMSL). Note, however, that $c = S$ is also a solution for this expression (when $c = S$, $m = 1$, and terms involving P cancel); this results in some difficulty in the numerical resolution of other roots when they approach S .

Information about the limit of infinite channel width for (4.34) may be obtained by scaling lengths in the problem on $L = L_w \equiv (D^*/E^*)^{1/4}$, instead of b^* (c.f. §3.1). After appropriately redefining the wall and fluid parameters (R_w , M , etc.; note that $B=1$ for $L=L_w$), the

dispersion relation (4.34) is changed only through the introduction of a factor of (b^*/L_w) in the arguments of g and P . As seen in §4.4, symmetric disturbances are the least stable, and we thus consider $P(x) = \tanh(x)$ here. In the limit of infinite channel width, $(b^*/L_w) \rightarrow \infty$, so that $P(kmb^*/L_w)$ and $P(kb^*/L_w)$ both go to 1. The parenthesized term in (4.34) thus becomes

$$\left(\Delta \left[-\frac{1}{km} + \frac{1}{k} \right] - (S - c)^2 \right) = 0, \quad (4.35)$$

where S and c in (4.35) are scaled on $\hat{u} \equiv (E^* L_w / \rho^*)^{1/2}$ and k on L_w^{-1} . Assuming that c is real (*i.e.* that points being considered lie on the neutral stability curve) and squaring once to get rid of the square root in the definition of m , (4.35) becomes on separating real and imaginary parts

$$\begin{aligned} k^2 q^3 + 2 R_w \Delta_I q^2 - 2 k \Delta_R q - \frac{2 R_w}{k} \Delta_R \Delta_I &= 0 \quad \text{and} \\ R_w k q^4 - 2 R_w \Delta_R q^2 - 2 k \Delta_I q + \frac{R_w}{k} (\Delta_R^2 - \Delta_I^2) &= 0. \end{aligned} \quad (4.36)$$

In (4.36) $q = S - c$ and $\Delta = \Delta_R + i \Delta_I$. Equations (4.36) are solved using Newton's method (we again use DNEQNF from IMSL); results are shown in §4.4.

If the wave number k goes to zero, the Orr-Sommerfeld equation degenerates to $\varphi^{(iv)} = 0$, and the boundary conditions at the wall to $i \operatorname{Re}^{-1} (S - c) \varphi''' = 0$ and $(S - c) \varphi' = 0$. For symmetric disturbances the only non-trivial solution is $c = S$, which is stable. For antisymmetric disturbances the only eigenfunction is trivial, and hence stable; this corresponds to the movement of the fluid across the midline of the channel as a solid body. Thus, unlike the case of a developing flow profile (*c.f.* Chapter 5) the limit $k \rightarrow 0$ is not of interest for the purposes of determining the onset of instability.

§4.4 Results

The asymptotic dispersion relation (4.24), (4.30) has two roots, the flutter modes of the system. At zero flow speed these have equal growth rates and phase speeds of equal magnitude but opposite sign; the root with positive phase speed we call root 1 and the other root 2. As the flow speed is increased, root 2 is slowed until a flow speed S_D , at which it reverses direction and travels downstream. In an undamped system (when wall damping G and viscosity ϵ are 0) the phase speeds of roots 1 and 2 coalesce at a higher flow speed, S_F , at which point the growth rates of the roots split from zero to become positive and negative, heralding instability; this transition is shown in figure 4.1. As noted in Chapter 2, the addition of wall damping breaks the unstable equilibrium existing for flow speeds S between S_D and S_F , so that instability appears for root 2, at $S = S_D$. The addition of viscosity may restabilize the system so that flutter reappears, at a flow speed larger than S_D , as shown by Grotberg and Reiss (1982, 1984); this is shown in figure 4.2, which shows root 2 of the asymptotic and exact dispersion relations.

The agreement between the asymptotic and exact solutions is clearly very good in figure 4.2, but this changes when the wall damping is decreased slightly, as in figure 4.3 (which shows roots 1 and 2 of the dispersion relation in 4.3A and B, respectively). For this case the exact solution shows that the wall damping is no longer sufficient to destabilize root 2 (which for S between S_D and S_F is Type A, as defined by Benjamin 1963 and Landahl 1962, and discussed in Chapter 2), so that root 1 (which is Type B) is instead that which goes unstable. The asymptotic solution, however, still predicts stability for root 1 and instability for root 2. Figure 4.4 shows the more physical case of lower wall damping, for which the singularity anticipated in the asymptotic solution is seen. This singularity may be expected any time the wall damping is small; however, in the cases in which we are interested, air flow in flexible tubes and the lung airways,

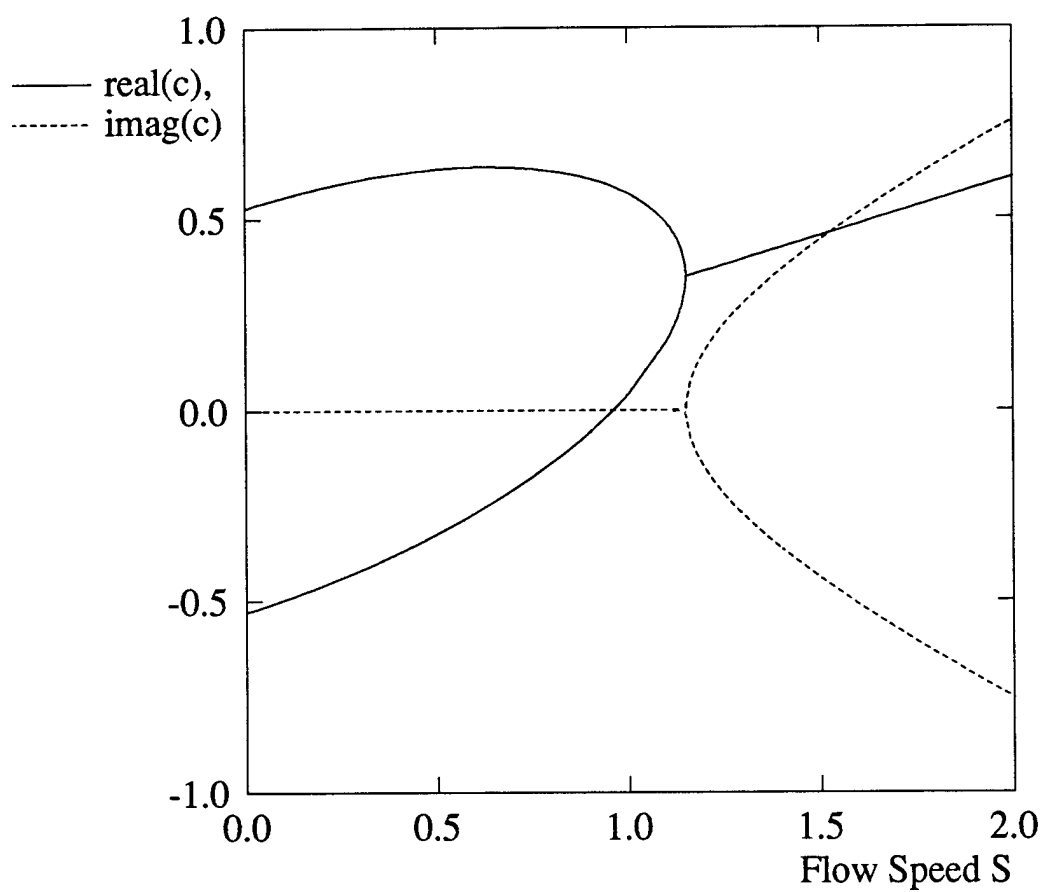


Figure 4.1: Plug flow dispersion relation for undamped system. Solid curve gives $\text{real}(c)$, dashed, $\text{imag}(c)$. $M=10$, $B=5$, $T=0$, $k=0.5$.

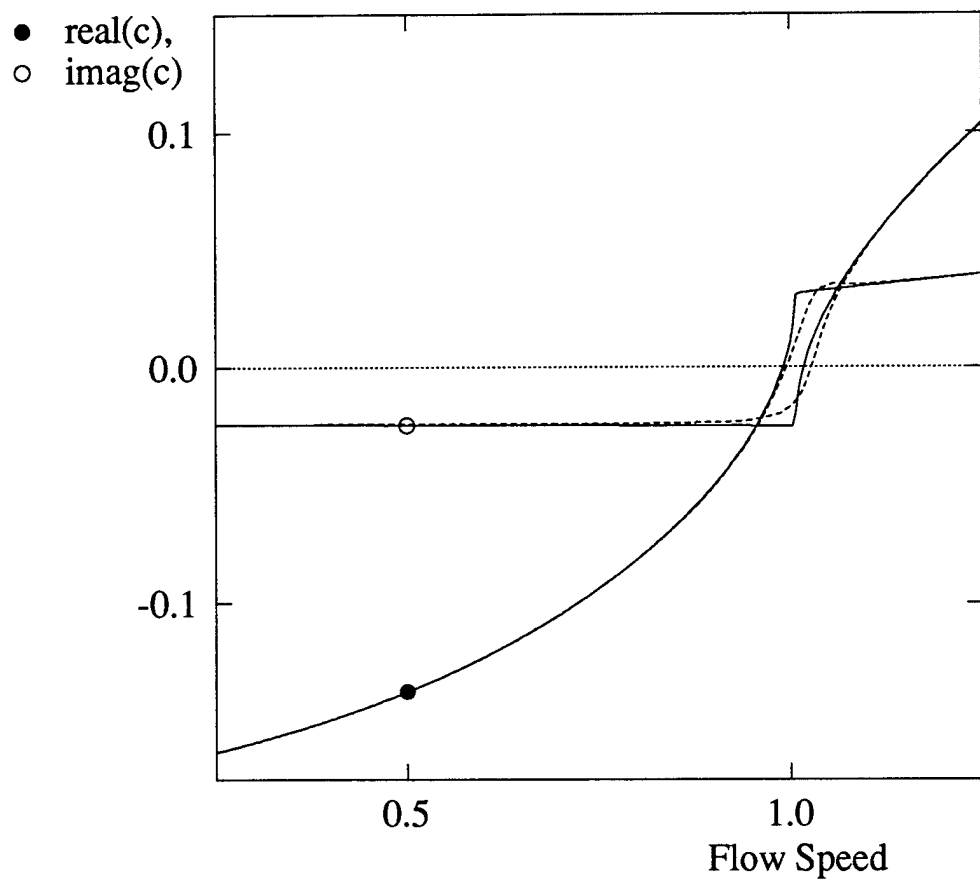


Figure 4.2: Plug flow dispersion relation for damped system, root 2, showing exact (solid curves) and asymptotic (dashed curves) solutions. • $\text{real}(c)$; ○ $\text{imag}(c)$. $M=3190$, $B=542$, $T=0$, $G=16$, $R_w=2230$, $k=0.1$

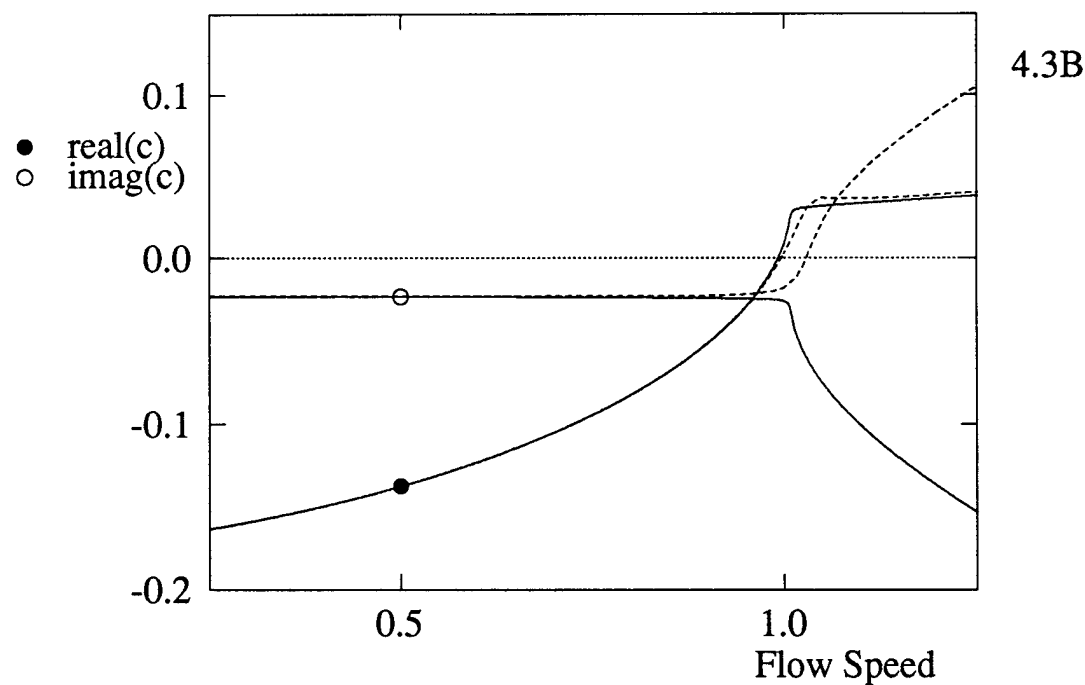
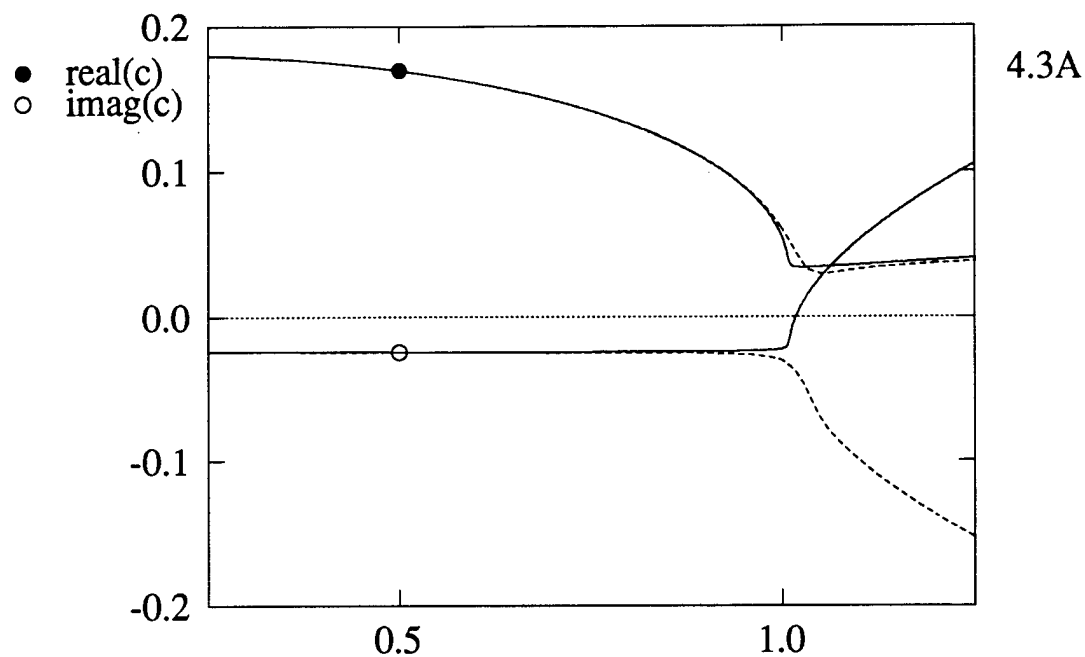


Figure 4.3: Plug flow dispersion relation, showing difference between exact (solid curves) and asymptotic (dashed curves) solutions. • real(c); ○ imag(c). 4.3A shows root 1, 4.3B root 2. $M=3190$, $B=540$, $T=0$, $G=15$, $R_w=2230$, $k=0.1$.

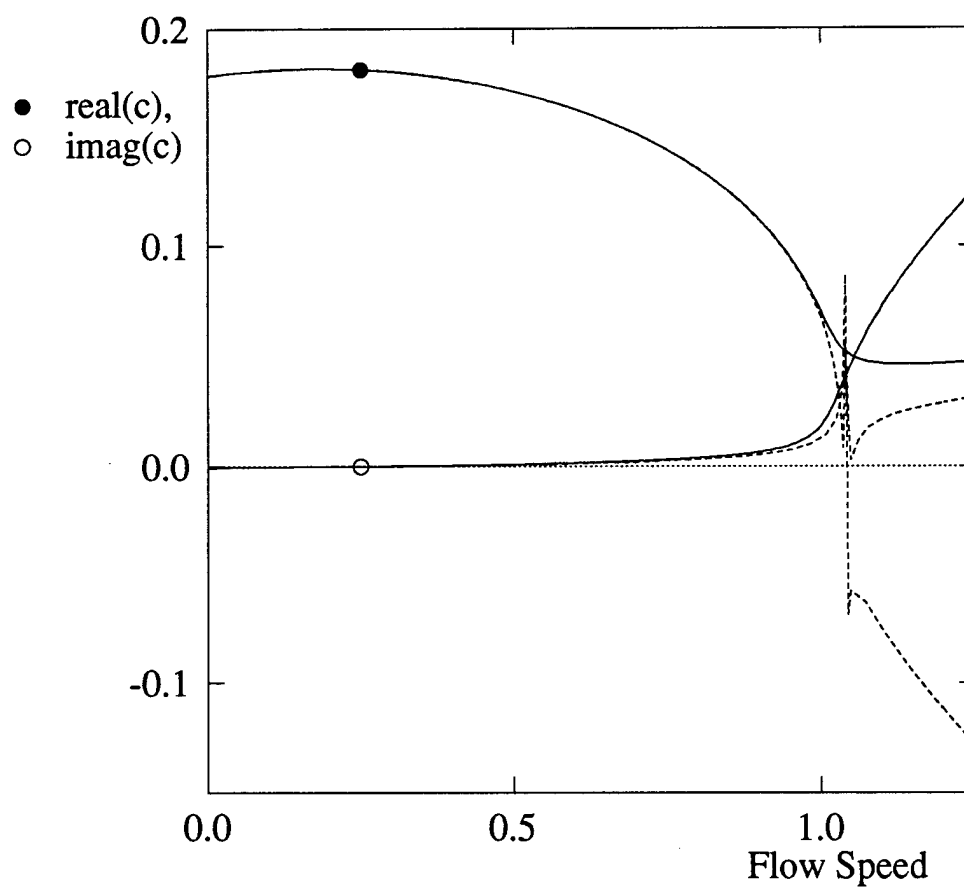


Figure 4.4: Plug flow dispersion relation, showing singularity in asymptotic solution. Solid curve gives exact solution, dashed, asymptotic. \bullet $\text{real}(c)$; \circ $\text{imag}(c)$. Root 1. $M=3190$, $B=542$, $T=0$, $G=0.054$, $R_w=2230$, $k=0.1$.

the solution remains valid for flow speeds up to and including the onset of instability.

The discrepancy between the behavior of the exact and asymptotic solutions of the problem as wall damping is decreased is a direct result of the assumptions used in the formulation of the latter. As the expansion parameter ϵ in the asymptotic solution goes to zero the problem becomes inviscid, so that at leading order the solution is that for inviscid flow. Implicit in this expansion, therefore, is the assumption that the effects of viscosity may be included as a small correction to the inviscid result, an assumption that is clearly not true in figure 4.3. Thus as long as wall damping is sufficiently large (by comparison with viscosity) to maintain the stability of root 1 (the Type B flutter mode) the asymptotics agree well with the exact solution. However, when the wall damping is smaller, so that root 1 is unstable, there is an order one discrepancy between the viscous and inviscid solutions for larger flow speeds, and the asymptotics may no longer be able to accurately model the system. Nonetheless, for walls with sufficiently small damping and large mass ratios (as in figure 4.4 and noted above), the asymptotic solution is able to accurately predict instability for root 1 before the appearance of the singularity, and before the predicted behavior for roots 1 and 2 differs significantly from that in the exact solution. For cases of interest, root 1 becomes unstable as shown in figure 4.4, before instability is seen for root 2.

In figure 4.5 we show curves of neutral stability (lines along which the growth rate of the disturbances vanish) for the plug flow base state, for symmetric (4.5A) and antisymmetric instabilities (4.5B). These give the flow speed at which instability appears as a function of wave number; points below (above) the curve are stable (unstable). The minima of the curves give the flow speed S_{cr}^F at which flutter appears, and the corresponding critical wave number k_{cr} . Comparing 4.5A and B shows that the symmetric mode is the least stable, which is generally true. In both 4.5A and B curves for both the exact and asymptotic solutions are plotted, and give

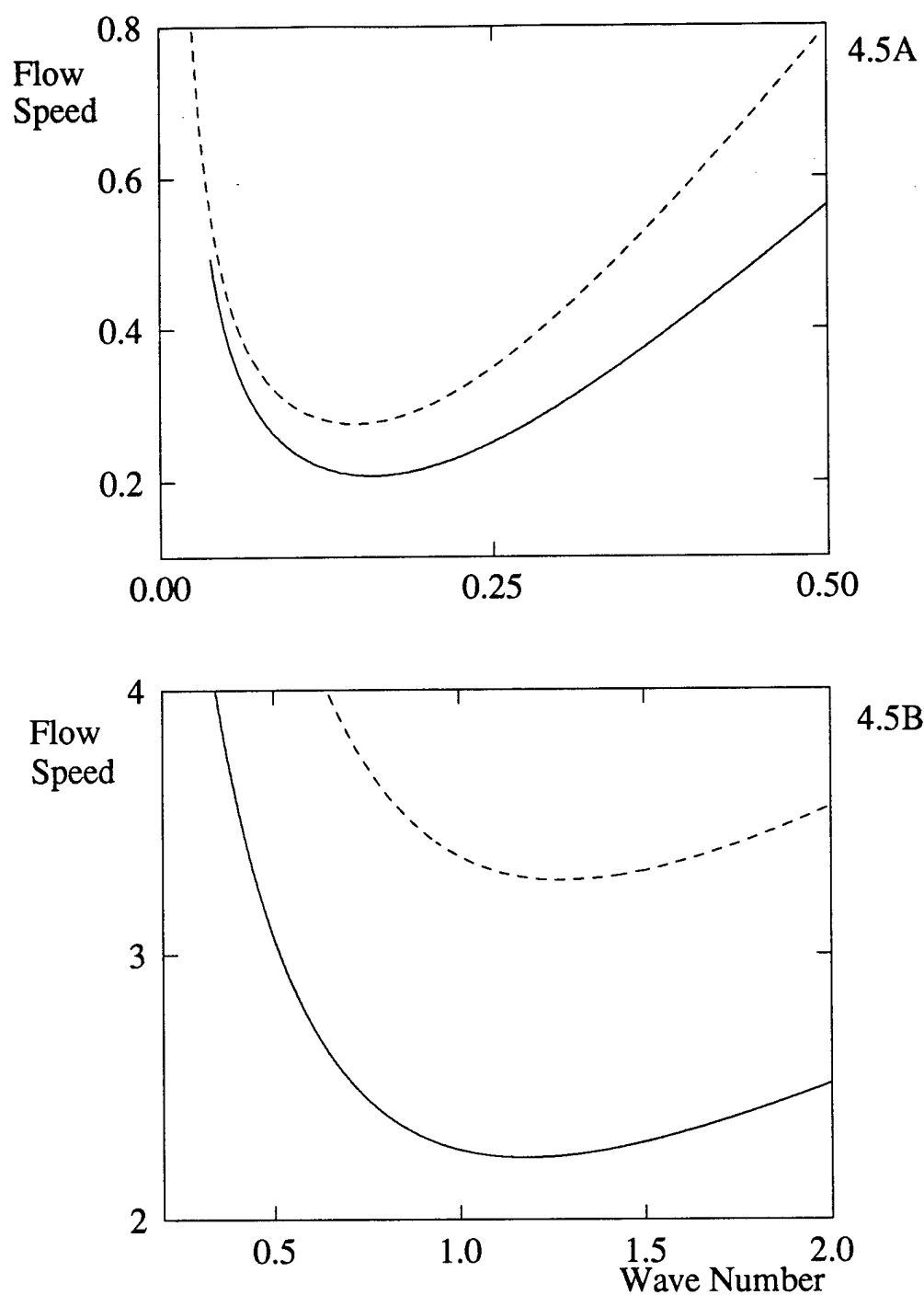


Figure 4.5: Neutral stability curves for plug flow, symmetric disturbances (4.5A) and antisymmetric disturbances (4.5B). Solid curves give exact solution, dashed, asymptotic. $M=3190$, $B=542$, $T=0$, $G=0.054$, $R_w=2230$.

similar but not identical results; the agreement between the two is, however, better for the symmetric mode than the antisymmetric mode. In that the symmetric disturbances become unstable before antisymmetric ones the larger discrepancy in the latter case is physically immaterial. Both symmetric and antisymmetric disturbances are seen to be stable for long wave lengths (small k), as noted in §4.3.

Several neutral stability curves, for different values of the wall damping G and mass ratio M , are shown in figure 4.6. Note that because the mass ratio appears in the definition of G , to isolate the effect of variation of M it is in this case necessary to allow G to change while holding $\hat{G} (\equiv b^* G^* / \hat{u})$ fixed. As the symmetric mode is unstable first, these curves are for the symmetric instability. For both values of the mass ratio shown (indicated by filled and open symbols, respectively), increasing the wall damping is stabilizing, which may be expected as the instability is for these parameter values a Type B instability, which is stabilized by wall damping. Increasing \hat{G} also increases the wavelength of (decreases k for) the instability. For the larger mass ratio (filled symbols), the instability moves to still smaller k . For smaller values of the wall damping, increasing the mass ratio is destabilizing, which is consistent with the fact that the flutter instability is destabilized by wall inertia. As both the wall damping and M are increased, however, the wavelength of the instability becomes long enough that the system is stabilized by the band of long-wave stability noted above and in §4.3; thus for sufficiently large wall damping increasing the wall inertia is in fact stabilizing. This is shown in figure 4.7 by plotting just the minima of the neutral stability curves, S_{CR}^F , for different values of the wall damping G . For the smaller (more physically relevant) values of the wall damping increasing M is destabilizing, but this is not the case for more heavily damped walls. This figure also compares the results for the exact and asymptotic solutions; the two are seen to agree reasonably well, with the same essential

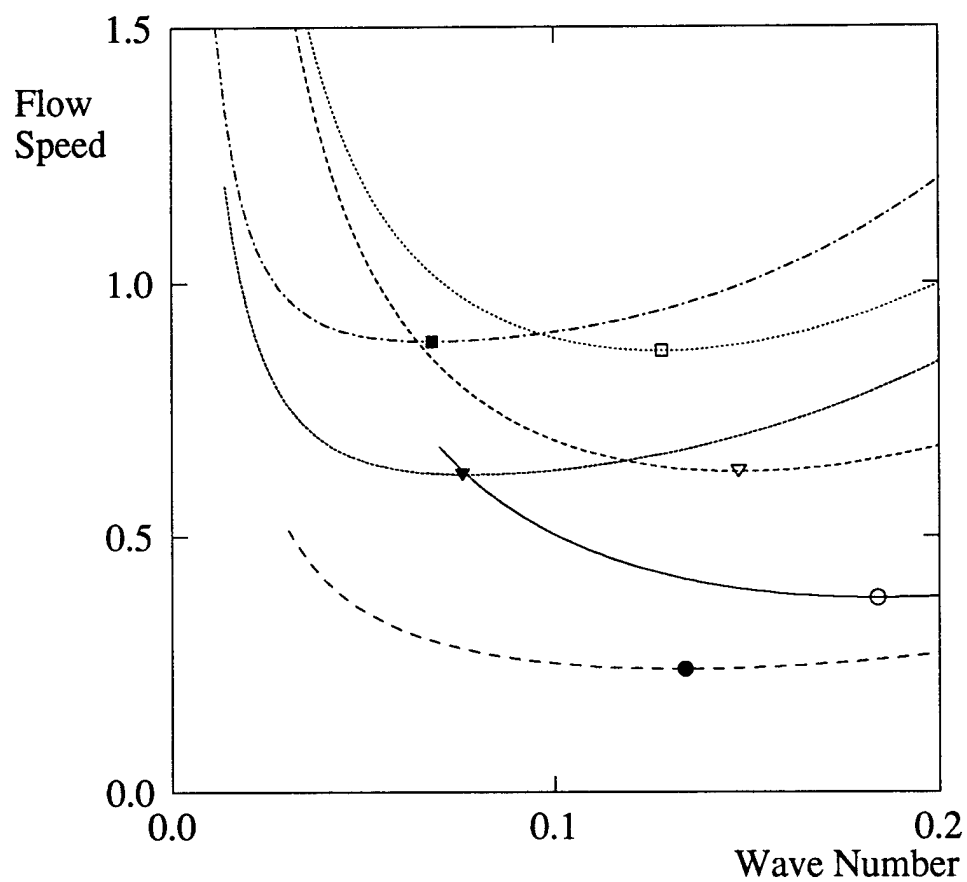


Figure 4.6: Plug flow neutral stability curves for different M , G , showing long wave stabilization. Open symbols give $M=500$, filled, $M=5000$; $\circ \hat{G} \times 5000 = 0.1567$; $\nabla \hat{G} \times 5000 = 1.567$; $\square \hat{G} \times 5000 = 4.702$. Symbols are located at the minima of the neutral stability curves. $B=542$, $T=0$, $R_w=2230$. ($\hat{G} \equiv b^* G^* / \hat{u}$)

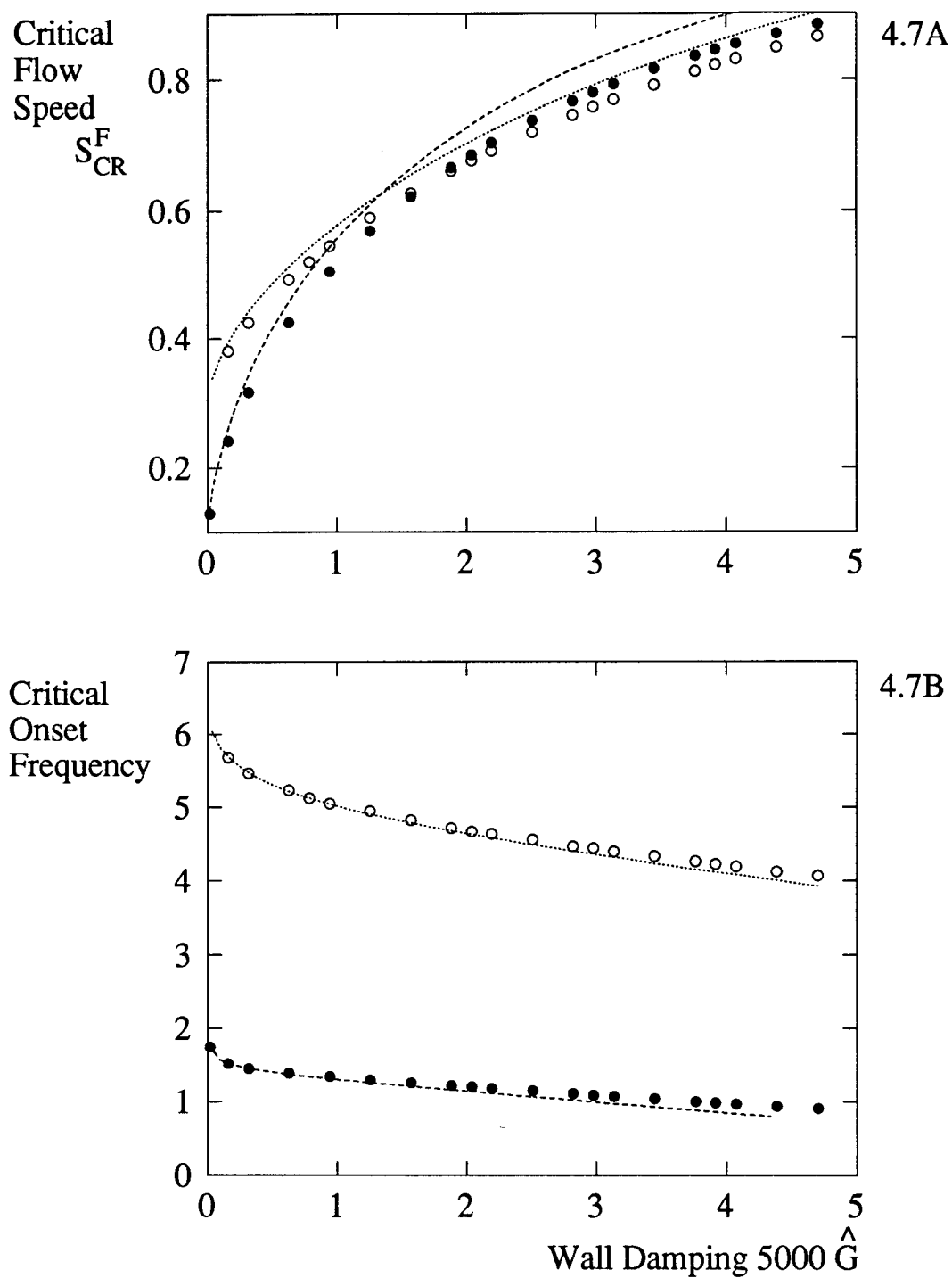


Figure 4.7: Plug flow critical flow speed S_{CR}^F (4.7A) and flutter frequency (4.7B) as functions of wall damping. \circ $M=500$, exact solution; \bullet $M=5000$, exact solution. Dashed and dotted curves give asymptotic solution for $M=500$ and $M=5000$, respectively. $B=542$, $T=0$, $R_w=2230$.

features being present in either case, though the values of S_{CR}^F differ slightly. As a result, subsequent figures show only the exact solution, with the understanding that the asymptotic result may be expected to retain the same features for slightly different critical flow speeds. Figure 4.7B shows how the variation of G and M affects the flutter frequency at the onset of instability; increasing either of the wall mass or the wall damping decreases the frequency, which in either case is consistent with physical intuition and observation. This also shows that the predictions for the critical flutter frequency made by the asymptotic and exact solutions are in very close agreement. Thus if the flutter frequency is the object of interest, the asymptotic solution (which is explicit and hence easier to use) may be used with little or no loss of accuracy.

Figure 4.8 shows how variation of the wall elastance and bending stiffness B changes the stability of the system, by plotting (in 4.8A) S_{CR}^F as a function of the wall elastance E (nondimensionalized on $(\rho^* v^{*2} / b^{*3}) \times 10^4$) for different values of B . For this figure S_{CR}^F is scaled on $(v^* / b^*) \times 10^2$, and the frequency (shown in 4.8B) on v^* / b^{*2} . Increasing E or B stabilizes the flutter instability, and increases the frequency. The frequency increases approximately as $E^{1/2}$, which is consistent with the results of Grotberg and Reiss (1984). In that the flutter instability depends fundamentally on wall elastance, the increase in S_{CR}^F with increasing E is as expected; in the limit of infinite E (a rigid wall), the flutter instability ceases to exist.

In figure 4.9, we show the effects of variation in the half channel width b , for different values of the wall elastance E . For later comparison with the results presented in Chapter 5, we scale velocity on $(v^* / x_0^*) \times 10^2$, length on x_0^* and frequency on (v^* / x_0^{*2}) , where x_0^* is a fixed distance from the mouth of the channel. (We have chosen x_0^* to be equal to the width of the channels considered in figures 4.1-8.) As the half channel width is increased, the effective viscosity in the channel decreases, which stabilizes the flutter instability, as seen in figure 4.9A.

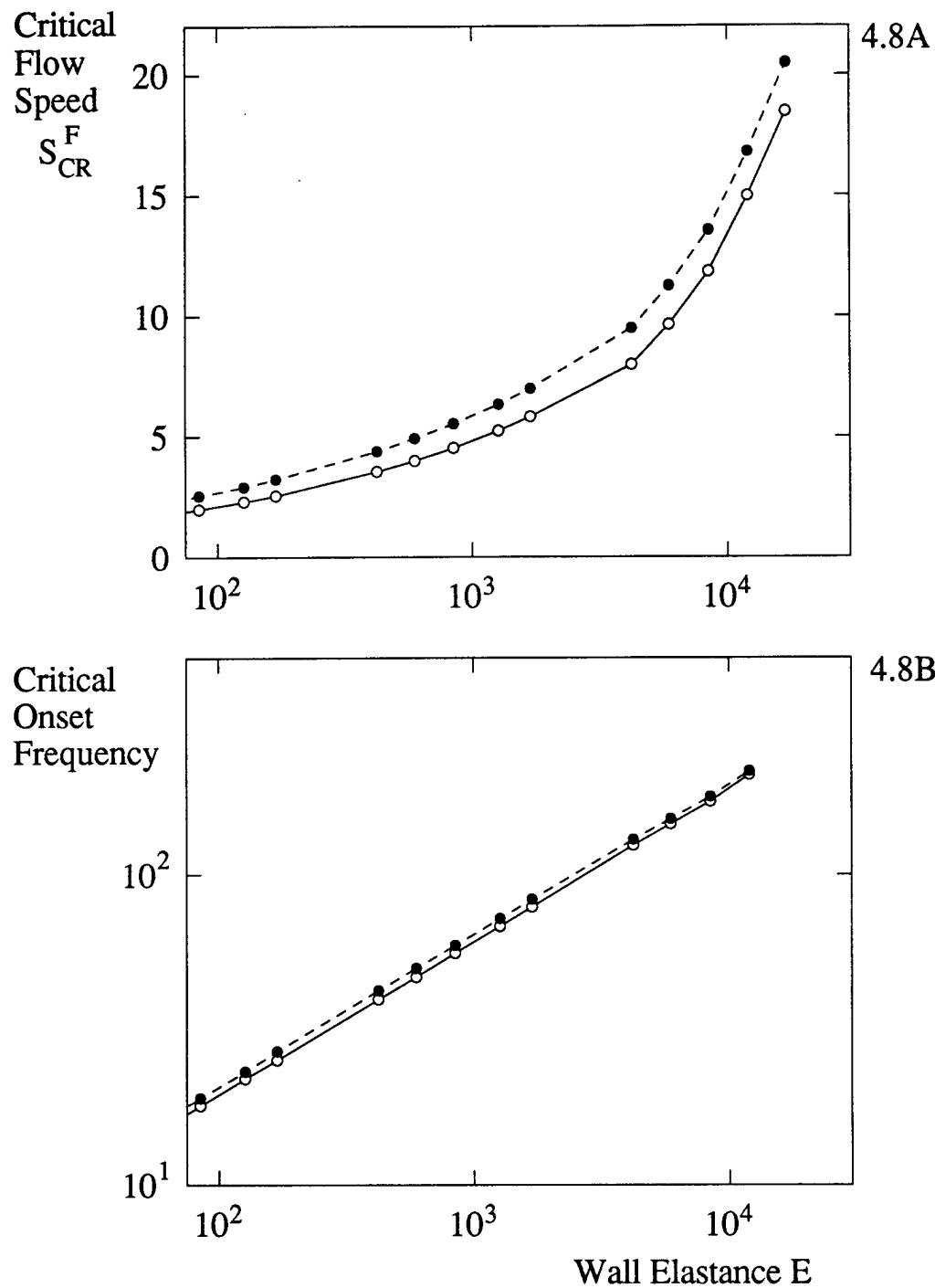


Figure 4.8: Plug flow S_{CR}^F (4.8A) and flutter frequency (4.8B) as functions of wall elastance for $B = 2.688 \times 10^4$ (\circ) and $B = 2.688 \times 10^5$ (\bullet). E^* scaled on $(\rho^* v^* / b^{*3}) \times 10^4$, flow speed on $(v^* / b^*) \times 10^2$, and frequency on (v^* / b^{*2}) . Other parameters as figure 4.4, modified for scaling.

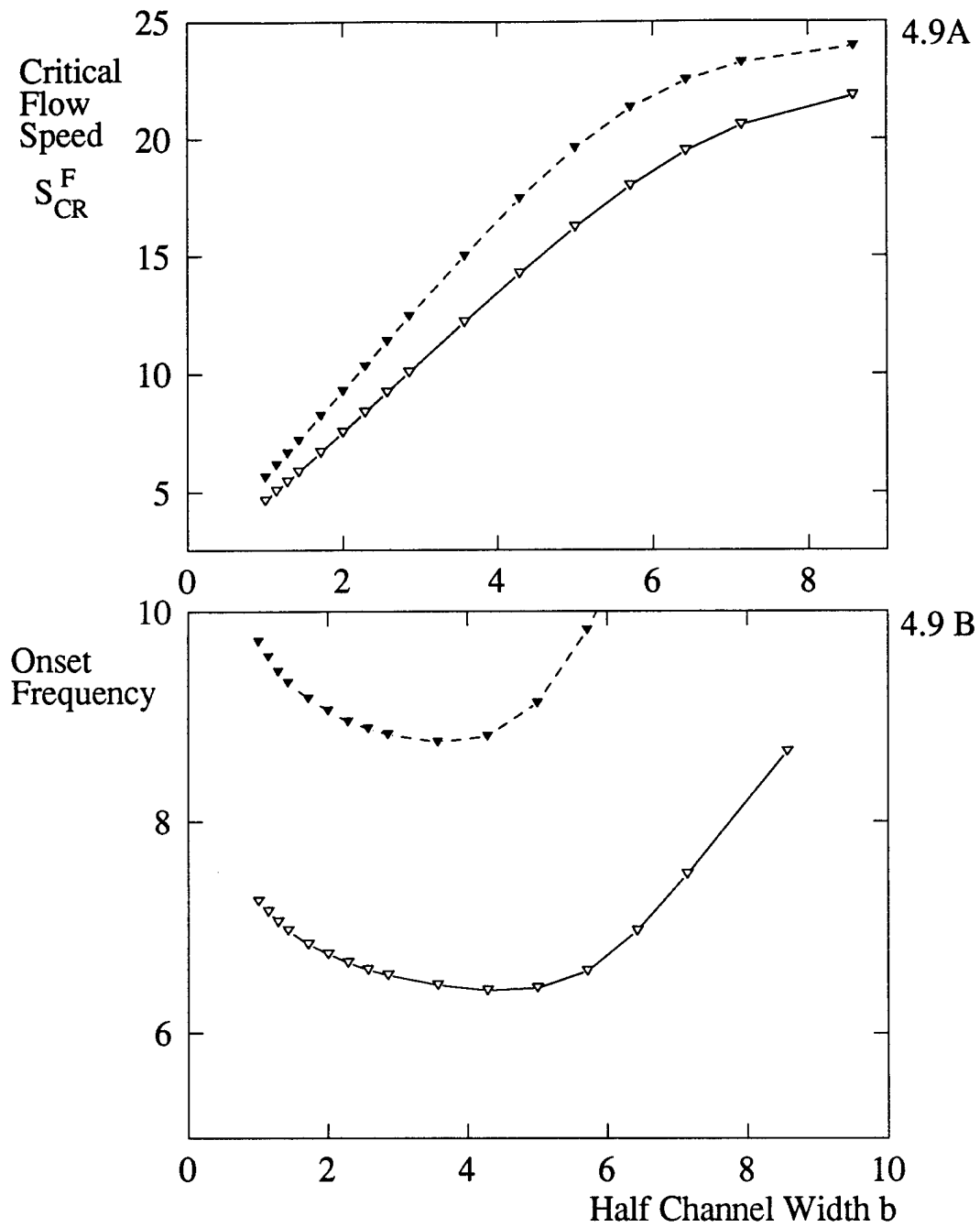


Figure 4.9: Plug flow S_{CR}^F (4.9A) and flutter frequency (4.9B) as functions of half channel width b^* / x_0^* for $E^* / (\rho^* v^{*2} / x_0^{*3}) \times 10^4 = 500$ (∇) and $E = 900$ (\blacktriangledown). Velocity and frequency scaled on $(v^* / x_0^*) \times 10^2$ and (v^* / x_0^{*2}) . x_0^* chosen = b^* in figure 4.4; other parameters as figure 4.4, modified for scaling.

In the limit of very wide channels the critical flow speed levels off, as seen at the end of the channel widths shown. Increasing the wall elastance is, as seen in figure 4.8, stabilizing. In figure 4.9B the frequency of the flutter instability at onset is shown as a function of the half channel width. This shows that as the half channel width is increased through moderate values, the flutter frequency decreases, but that for very large channel widths it increases again. This change in behavior may be understood by considering the neutral stability curves giving figure 4.9, which are shown in figure 4.10. These show curves for increasing b , along with the infinite channel limit (obtained from equations (4.36)). As b is increased, the neutral stability curves agree with the infinite b limit for disturbances with longer wavelengths (smaller wave numbers). Thus the critical wave number k_{CR} , which initially decreases with increasing b , reverses to increase towards the infinite channel limit for very wide channels. This increase results in the increase in flutter frequency shown in figure 4.9B. There is, of course, always a difference between the finite and infinite channel width curves for very long waves. Note that the channel widths relevant to physical tubes (*e.g.* those of the experiments of Gavriely *et.al.* 1989) are $b < 4$ in figure 4.9.

As we are specifically interested in pulmonary applications, it is useful at this juncture to consider the effects we have discussed above specifically in this context. Wheezing lung sounds are thought to be symptomatic of airway flutter (Grotberg and Davis 1980); thus the characteristics that distinguish the lungs of wheezing patients from healthy subjects should relate to those effects that destabilize the flutter instability. We saw above that these destabilizing effects include reduction of the wall elastance and bending stiffness, and reduction of the half channel width. All of these do correspond to the characteristics of asthmatic or lung obstructed patients' airways, which have more flexible walls and are narrower than those of healthy subjects. We directly compare our theoretical results with experimental observations in Chapter 6.

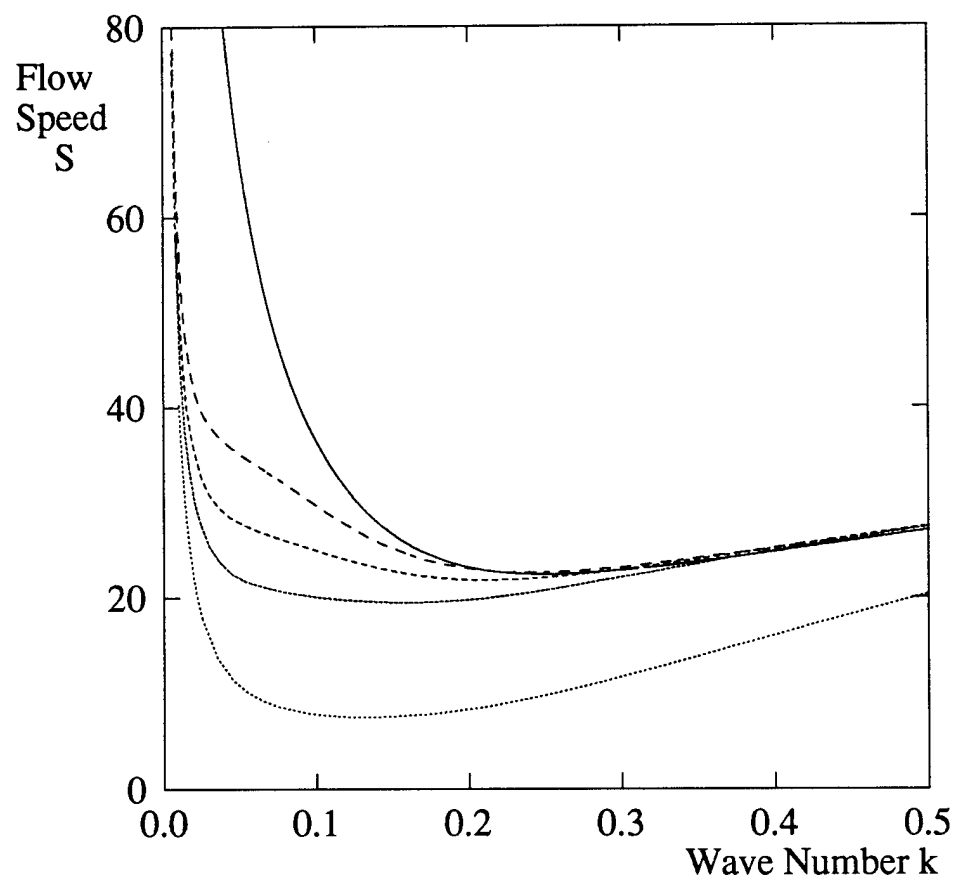


Figure 4.10: Plug flow neutral stability curves for different half channel widths. Dotted through solid curves are, respectively $b = 2, 6.4, 8.6, 11.4$ and infinite width. Scales and parameters as figure 4.9 ($E^* / (\rho^* v^{*2} / x_0^{*3}) = 500$).

CHAPTER 5: NUMERICAL AND ANALYTICAL SOLUTIONS FOR DEVELOPING BASE FLOW

§5.1 *Introduction and equations*

In this chapter we develop solutions to the Orr-Sommerfeld system derived in Chapter 3 with a developing base flow. An analytical solution is obtained for long wave disturbances in §5.2, and a numerical solution for disturbances of arbitrary wavelengths is formulated and tested in §5.3 and §5.4. Results are presented and compared with the plug flow solutions of Chapter 4 in §5.5, and a short discussion of the limit of infinite channel width, which turns out to be of mathematical interest, appears in §5.6. In Chapter 6 the solutions presented in this chapter are compared with experimental results. Both the analytical and numerical solutions presented below are general to flow profiles other than the developing flow, and we are therefore able to check our results through consideration of problems for which results are already known.

For flow profiles $u_0(z)$ satisfying the no slip boundary conditions, such as the developing flow solution (3.23), the Orr-Sommerfeld equation is

$$k(u_0 - c)(\varphi'' - k^2\varphi) - k u_0''\varphi + \frac{i}{R_w}(\varphi^{iv} - 2k^2\varphi'' + k^4\varphi) = 0 \quad (5.1)$$

and the boundary conditions (3.15) and (3.16) are

$$\begin{aligned} &(-(kc)^2 M - 2ikcG + Bk^4 + Tk^2 + 1)k\varphi + \\ &kc(c\varphi' + u_0'\varphi) - \frac{ic}{R_w}(\varphi''' - 3k^2\varphi') = 0 \end{aligned} \quad (5.2)$$

and

$$dk(c\varphi' + u_0'\varphi) + \frac{ic^2}{R_w}(\varphi'' + k^2\varphi) = 0, \quad (5.3)$$

both at $z = -1$. The midline boundary conditions (3.17) remain

$$\begin{aligned} \varphi(0) = \varphi''(0) = 0 & \quad (\text{symmetric}), \quad \text{or} \\ \varphi'(0) = \varphi'''(0) = 0 & \quad (\text{antisymmetric}). \end{aligned} \quad (5.4)$$

§5.2 Analytical solution for long waves

While it is in general difficult to solve the Orr-Sommerfeld system analytically, as indicated in Chapter 4, a solution for the case of long waves ($k \rightarrow 0$) is more tractable, and is developed in this section. We consider the limit of no horizontal wall motion here (*i.e.*, reduce (5.3) to $c\varphi' + u_0'\varphi = 0$ at $z = -1$) to simplify this analysis; comparison with the numerical solution (described in §5.3) shows that the results obtained are quantitatively the same as those obtained with the full boundary condition. In the following we do not *a priori* specify the base flow profile u_0 ; specific cases are considered after the derivation. For $k \ll 1$, let

$$\varphi \sim \varphi_0 + k\varphi_1 + \cdots \quad \text{and} \quad c \sim c_0 + kc_1 + \cdots. \quad (5.5)$$

Using these in the Orr-Sommerfeld equation (5.1) and letting $k \rightarrow 0$, we obtain

$$\varphi_0^{iv} = 0, \quad (5.6)$$

so that φ_0 is a cubic polynomial in z . Imposing the boundary conditions (5.4) and the leading order forms of (5.2) and (5.3), we find

$$\varphi_0 = z \quad \text{and} \quad c_0 = u_0'(z = -1). \quad (5.7)$$

Here we have normalized φ_0 so that $|\varphi_0(-1)| = 1$. The solution (5.7) is for symmetric disturbances; we address the antisymmetric mode below. We see from (5.7) that c_0 is strictly real,

and so must continue to the next order in k to evaluate the stability of the system.

At order k , the Orr-Sommerfeld equation (5.1) is

$$\phi_1^{iv} = -i R_w z u_0'' \quad (5.8)$$

and ϕ_1 is thus the sum of another cubic polynomial in z and a particular solution satisfying

$$\phi_{1P}''' = i R_w (u_0 - z u_0') \quad (5.9)$$

(after integration by parts once; further integration is dependent on the choice of the base flow u_0). Applying the boundary conditions (5.4) and the order k terms of (5.2), we find

$$\phi_1 = -\phi_{1P}(z=0) + B_1 z - \frac{\phi_{1P}''(z=0)}{2} z^2 + \frac{i R_w [1 - (u_0'(z=-1))^2]}{6 u_0'(z=-1)} z^3 + \phi_{1P}, \quad (5.10)$$

so that, from (5.3),

$$c_1 = i R_w \left(u_0'(z=-1) [\Phi_{1P}(z=0) - \frac{1}{2} \Phi_{1P}''(z=0) - \Phi_{1P}(z=-1) - \Phi_{1P}'(z=-1)] - \frac{1}{3 u_0'(z=-1)} [1 - (u_0'(z=-1))^2] \right), \quad (5.11)$$

where we have written $\phi_{1P} = i R_w \Phi_{1P}$ to make the imaginary character of c_1 explicit.

Equation (5.11) for c_1 is strictly imaginary, so that c_1 is the growth rate for the disturbance. To find the critical flow speed at which c_1 becomes positive, it is necessary to integrate the expression (5.9) for ϕ_{1P} . We consider two cases. For Poiseuille flow, $u_0 = 1.5 S (1 - z^2)$, and we may integrate to find ϕ_{1P} and evaluate (5.11) analytically, obtaining $c_1 = 0.067 i R_w (18 S^2 - 5)$. Instability appears at $S_{CR}^{LW} = 0.527$; at this point $c_0 = u_0'(-1) = 1.581$. These are in good agreement with the numerical solution (described below), which gives $S_{CR}^{LW} = 0.525$ and $c = 1.575$ (at $k = 0.001$). For developing flow (3.23) we numerically integrate (5.9)

using Simpson's rule, and find (for $R_w=2230$ and $x=1$) $S_{CR}^{LW} = 0.1387$ and $c_0 = 1.094$; again, these agree well with the values from the numerical solution of the full problem, $S_{CR}^{LW} = 0.1388$ and $c = 1.093$ (at $k = 0.001$). The existence of the long wave instability is also useful for the full numerical solution, as it gives starting points from which the stability calculation may proceed.

The effect of variation of the half channel width and wall elastance on the long wave stability boundary for developing flow is shown in figures 5.1 and 5.2, which show the long wave critical flow speed S_{CR}^{LW} and volumetric flow rate, $b S_{CR}^{LW}$, as functions of the half channel width and wall elastance. In both figures flow speeds and half channel width are scaled on (v / x_0^*) and x_0^* , respectively, to isolate the effect of changing b ; by showing curves for increasing Reynolds numbers \check{R}_w (defined as $\check{u} x_0^* / v^*$, where $\check{u} = (E^* x_0^* / \rho^*)^{1/2}$), the effect of increasing elastance is also seen. These figures show that the critical flow speed increases as channel width is decreased, but that the critical volumetric flow rate decreases. Increasing the wall elastance increases both the critical flow speed and flow rate, thus stabilizing the system significantly.

Note that the stability bounds derived above do not depend on the wall properties other than the elastance; the effects of the mass ratio M , bending stiffness B , *etc.*, appear in the stability calculation only at higher orders in k . As a result, variation of these wall parameters may stabilize the system only to the point at which the long wave instability is critical. Furthermore, it is possible to find wall parameters such that the long wave and finite wavelength instabilities become unstable at the same flow speed, resulting in a codimension two bifurcation point. This is shown in figure 5.1 by also showing the critical flow speed for flutter (the finite wavelength instability), S_{CR}^F , as a function of b ; the codimension two point occurs when this curve intersects that for the long wave instability. Variation of other system parameters changes S_{CR}^{LW} in the same manner as S_{CR}^F (*c.f.* §5.5).

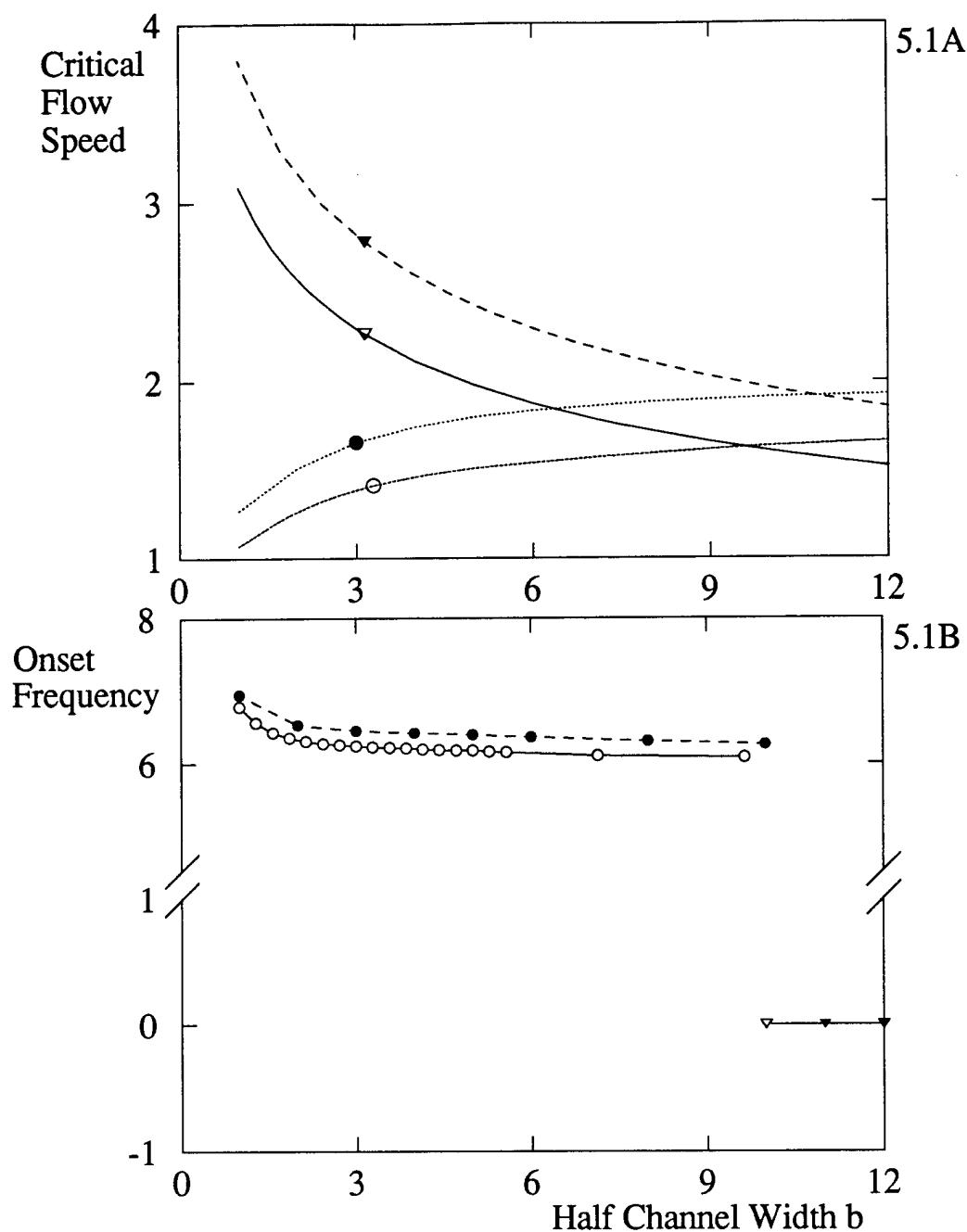


Figure 5.1: Critical flow speeds as functions of half channel width and elastance. b^* scaled on x_0^* , S^* on $(v^*/x_0^*) \times 10^2$. $\nabla, \blacktriangledown$: S_{CR}^{LW} ; \circ, \bullet : S_{CR}^F . Open symbols give $\check{R}_w = 2230$, filled $\check{R}_w = 3000$ (where $\check{R}_w \equiv (\hat{u} x_0^*/\nu)$ and $\hat{u} = (E^* x_0^*/\rho^*)^{1/2}$). Figure 5.1B shows the frequency (scaled on (v^*/x_0^{*2})) of the instability at onset. Other parameters as figure 5.7 ($M = 3190$), with modified scaling.

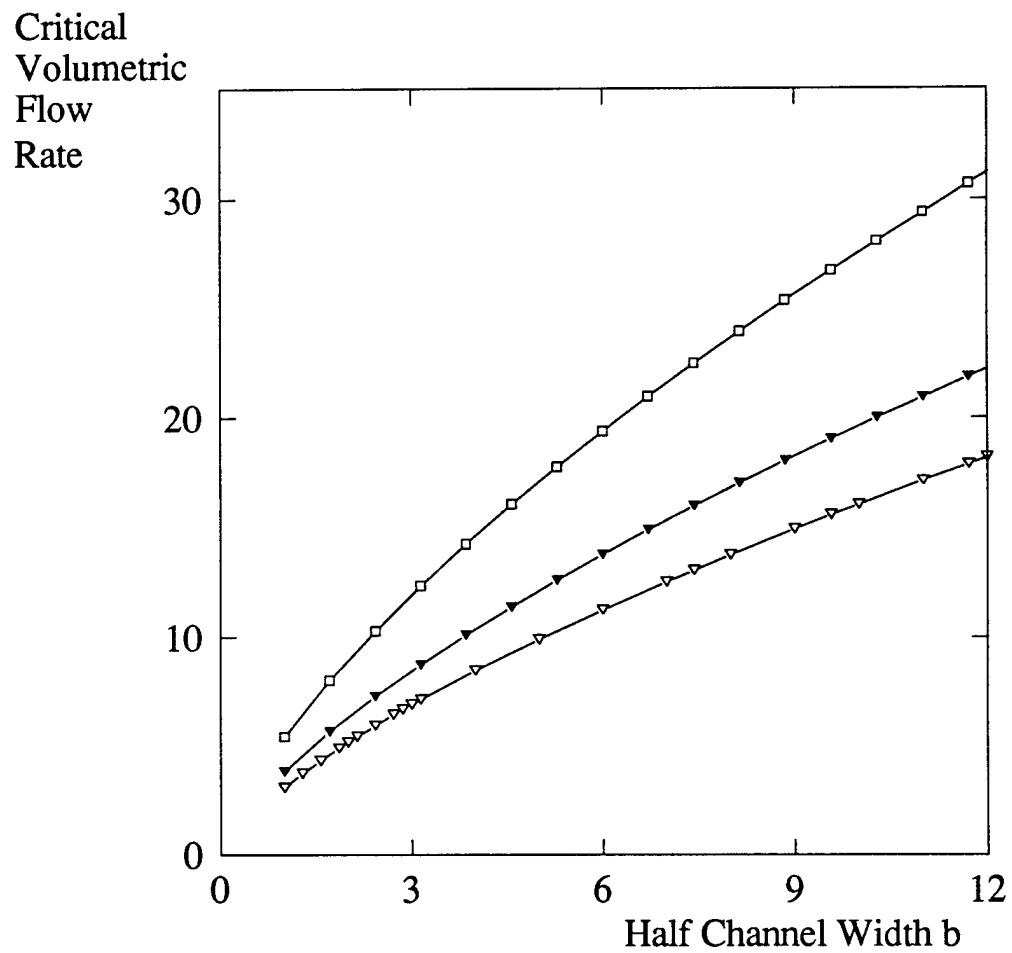


Figure 5.2: Critical volumetric flow rate for long wave instability as a function of half channel width and elastance. Scales and parameter values as in figure 5.1. ∇ $\check{R}_w = 2230$; \blacktriangledown $\check{R}_w = 3000$; \square $\check{R}_w = 5000$.

The above treatment was strictly for the case of symmetric disturbances. When antisymmetric disturbances are considered the analysis proceeds in much the same manner, with the midline boundary conditions replaced by the antisymmetric forms of (5.4). In this case the leading order term of the wall condition (5.2) and the second midline condition are redundant, so that the solution for the leading order antisymmetric eigenfunction and eigenvalue ϕ_{A0} and c_{A0} becomes a one parameter family of solutions,

$$\phi_{A0} = A_{A0} + D_{A0} z^2, \quad \text{and} \quad c_{A0} = \frac{(A_{A0} + D_{A0})}{2 D_{A0}} u_0'(z = -1), \quad (5.12)$$

(for normalization we may specify one of A_{A0} or D_{A0} ; when possible we take $A_{A0} = 1$) provided the free parameter D_{A0} is non-zero. If D_{A0} is zero the second wall condition, (5.3), requires $A_{A0} = 0$, and the solution for ϕ_{A0} is trivial. At $O(k)$, condition (5.2) becomes a condition on D_{A0} , and requires it to be zero. Thus the only eigenfunction is the trivial one, and there is no long wave antisymmetric instability. This is similar to the antisymmetric long wave limit for plug flow (§4.3); in the long wave limit the fluid may be moved as a solid body across the midline, resulting in a zero disturbance flow field.

It may be noted at this juncture that in the limit of long waves the assumption of locally parallel flow made in the derivation of the Orr-Sommerfeld equation is violated. Thus in this limit the developing flow result would be somewhat different if non-parallel effects were included; possible differences are considered in the discussion of Chapter 7. Clearly this is irrelevant for Poiseuille flow, and the similarity between the Poiseuille and developing flow stability results suggests that the developing flow result is at least qualitatively accurate. Note that if the wall boundary conditions (5.2, 5.3) are replaced by those for a rigid wall, $\phi(z=-1) = \phi'(z=-1) = 0$, the solution for either symmetric or antisymmetric disturbances is trivial, confirming

that the long wave limit does not correspond to the Tollmien-Schlichting instability.

§5.3 Numerical solution method

Because the Orr-Sommerfeld equation is notoriously stiff, standard linear shooting techniques that might otherwise be used to obtain a solution to the eigenvalue problem may fail, especially for high Reynolds numbers flows. We therefore develop in this section a multiple shooting algorithm with orthonormalization to solve (5.1) with boundary conditions (5.2-4) numerically. This orthonormalization method is similar to that proposed by Davey (1973), with modifications to allow for the more complicated boundary conditions introduced by the compliant wall.

Linear shooting methods solve a boundary value problem as an initial value problem, using superposition of solutions to satisfy the boundary conditions at the other end of the domain. To accomplish this numerically, (5.1) is written as a first order matrix equation for the vector $\mathbf{p} = (\varphi \ \varphi' \ \varphi'' \ \varphi''')^T$, as $\mathbf{p}' = \mathbf{D} \mathbf{p}$, where the entries of \mathbf{D} are found in the usual manner from (5.1). Boundary conditions (5.2) and (5.3) are written as vector conditions on \mathbf{p} , $\mathbf{B}_1 \cdot \mathbf{p} = 0$ and $\mathbf{B}_2 \cdot \mathbf{p} = 0$, where the k^{th} components of \mathbf{B}_1 and \mathbf{B}_2 are the coefficients of the $(k-1)^{\text{st}}$ derivatives of φ in (5.2) and (5.3), respectively. An 'initial condition', \mathbf{p}_M for \mathbf{p} is chosen to satisfy the midline boundary conditions (5.4) and integrated numerically, according to the vector form of (5.1), across the channel to obtain \mathbf{p} at the wall, \mathbf{p}_w . (We use the variable step Runge-Kutta routine DIVPRK from IMSL for the numerical integration.) Because the problem is linear, this integration may be written as a matrix operation, as $\mathbf{p}_w = \mathbf{R} \mathbf{p}_M$, where \mathbf{R} is the 'transfer matrix' for the problem. Note that the j th column of \mathbf{R} , \mathbf{r}_j , is found by integrating the j th basis vector \mathbf{e}_j (where $\mathbf{e}_1 = (1 \ 0 \ 0 \ 0)^T$, etc.) across the interval. The boundary conditions (5.2) and (5.3), in vector form, then

require

$$\begin{pmatrix} B_1^T \\ B_2^T \end{pmatrix} p_w = \begin{pmatrix} 0 \\ 0 \end{pmatrix}, \quad \text{or} \quad \begin{pmatrix} B_1^T \\ B_2^T \end{pmatrix} R p_M = \begin{pmatrix} 0 \\ 0 \end{pmatrix}. \quad (5.13)$$

Substituting r_j for the j th columns of R and plugging in the symmetric initial condition $p_M = A_1 e_2 + A_2 e_4$, (5.13) becomes

$$\begin{pmatrix} B_1 \cdot r_2 & B_1 \cdot r_4 \\ B_2 \cdot r_2 & B_2 \cdot r_4 \end{pmatrix} \begin{pmatrix} A_1 \\ A_2 \end{pmatrix} = \begin{pmatrix} 0 \\ 0 \end{pmatrix}. \quad (5.14)$$

For a non-trivial solution, then, the determinant condition

$$(B_1 \cdot r_2)(B_2 \cdot r_4) - (B_1 \cdot r_4)(B_2 \cdot r_2) = 0 \quad (5.15)$$

must be satisfied. This condition determines the eigenvalue c , which is iterated from an initial guess by a root finding algorithm until (5.15) holds. Clearly the same procedure may be applied for the antisymmetric case, replacing the basis vectors used in the initial condition with e_1 and e_3 .

This procedure will work unless the vectors r_2 and r_4 in (5.15) are parallel or nearly parallel, that is, unless the integration of e_2 and e_4 across the interval yields nearly the same solution. To see how this may occur, consider the simple system $\varphi'' - m^2 \varphi = 0$ with m large. The general solutions for φ are $e^{\pm mz}$, and any initial condition will be a linear combination of these. Thus as any general initial condition (that does not coincide exactly with the e^{-mz} solution) is integrated through positive values of z it will rapidly become dominated by the growing exponential, and solutions for differing initial conditions will thus soon become almost equal. The Orr-Sommerfeld system similarly has exponentially growing and decaying solutions, so that even though the initial conditions for the columns in the transfer matrix R are orthonormal, the

columns themselves may still be almost parallel. Furthermore, even if the integration of the different columns of the transfer matrix proceeds with high accuracy, the exponential growth will result in the magnitude of the columns becoming very large, so that the numerical roundoff error in the evaluation of the determinant may be significant. Systems exhibiting this type of behavior are described as stiff, and it is to address stiffness that orthonormalization is introduced.

Orthonormalization modifies the transfer matrix to make it better conditioned while at the same time maintaining the singularity of those columns that are used in the calculation of the determinant. This is accomplished by normalizing all of the columns of the matrix and orthonormalizing (using Gram-Schmidt orthonormalization) those two that appear in the determinant. If the columns of the transfer matrix \mathbf{R} are neither too nearly parallel nor too large in magnitude it may be possible to obtain a solution by altering \mathbf{R} in this manner. However, it is frequently not possible to accurately orthonormalize the transfer matrix for the entire interval; in these cases the interval of integration is divided into two or more smaller intervals. The solution \mathbf{p}_w at the endpoint of the interval is then the product of the transfer matrices for each of these intervals and the initial condition: for two subintervals, $\mathbf{p}_w = \mathbf{R}_2 \mathbf{R}_1 \mathbf{p}_M$. As \mathbf{R}_1 involves integration over a shorter domain, its columns will not be so large in magnitude nor so nearly parallel as those of the matrix \mathbf{R} ; it may thus be possible to orthonormalize \mathbf{R}_1 , as indicated above, to obtain a new matrix \mathbf{R}_1 . This modified matrix is next multiplied by \mathbf{R}_2 . This product will also have non-orthonormal columns, but the resulting matrix will again be better conditioned than the matrix \mathbf{R} . It may thus be possible to orthonormalize the product $\mathbf{R}_2 \mathbf{R}_1$ and use the resulting matrix to evaluate the required determinant. Clearly this procedure may be repeated over as many subintervals as necessary to obtain accurate results.

Note that because c and ϕ (and hence \mathbf{p}) are complex valued, the \mathbf{R}_j will likewise be

complex valued, and the dot product used in the orthonormalization must therefore be applicable to complex numbers. Two possible choices are $\mathbf{a} \cdot \mathbf{b} = a_j b_j^\dagger$ (where the dagger indicates complex conjugate, and repeated indices indicate summation over the index) or $\mathbf{a} \cdot \mathbf{b} = a_j b_j$. We use the second (complex valued) dot product, as it preserves the analyticity of the determinant and allows the use of a Muller's method to locate the eigenvalue (we use DZANLY from IMSL). Some care must be taken, however, as this analytic dot product may be zero when the vectors being multiplied are non-zero, but this never proved to be a problem.

Next suppose that there are more complicated boundary conditions at the channel midline; this occurs, for example, when we test our code by considering flow over a compliant plate. In this case it may not be possible to select an initial condition that corresponds to a linear combination of basis vectors, as was the case above. It will of course still be possible to write down two initial conditions, but they will in general be linear combinations of all four basis vectors, so that if we continue as before and orthonormalize those columns of the transfer matrix that contribute to the determinant, all four columns will be orthonormalized. However, while the orthonormalization of two columns of the matrix leaves the singularity of the determinant unchanged, this is not the case for three or more columns. To see this, consider the determinant condition (5.15), in matrix form

$$\text{Det} \begin{bmatrix} B_1 \cdot r_2 & B_1 \cdot r_4 \\ B_2 \cdot r_2 & B_2 \cdot r_4 \end{bmatrix} = 0. \quad (5.16)$$

Normalizing the column vectors r_j will clearly not alter the singularity of the determinant. Orthogonalization of the second and fourth columns of the transfer matrix results in the replacement of r_4 with $r_4 - (r_2 \cdot r_4) r_2 / (r_2 \cdot r_2)$; this is equivalent to adding a multiple of the first column of the determinant matrix (5.16) to the second, which also leaves the singularity of the

determinant unchanged. However, if three columns of the transfer matrix, say \mathbf{r}_2 , \mathbf{r}_3 and \mathbf{r}_4 , are orthogonalized, then \mathbf{r}_3 and \mathbf{r}_4 are transformed according to

$$\begin{aligned} \mathbf{r}_3 &\rightarrow \mathbf{r}_{3A} = \mathbf{r}_3 - [(\mathbf{r}_3 \cdot \mathbf{r}_2)\mathbf{r}_2 / (\mathbf{r}_2 \cdot \mathbf{r}_2)] \quad \text{and} \\ \mathbf{r}_4 &\rightarrow \mathbf{r}_4 - [(\mathbf{r}_4 \cdot \mathbf{r}_2)\mathbf{r}_2 / (\mathbf{r}_2 \cdot \mathbf{r}_2)] - [(\mathbf{r}_4 \cdot \mathbf{r}_{3A})\mathbf{r}_{3A} / (\mathbf{r}_{3A} \cdot \mathbf{r}_{3A})], \end{aligned} \quad (5.17)$$

and orthogonalization results both in taking a linear combination of the two columns of the determinant matrix and in the appearance in the determinant of factors of the third column of the transfer matrix. As the factors of \mathbf{r}_3 were not present in the original determinant, we may not expect that the singularity of the modified determinant will be that of the original. This analysis was simplified by the fact that we left the midline conditions in the form of basis vectors, but is readily extended to the more general case. Thus in order to use the orthonormalization scheme developed above we must be able to begin with initial conditions in the form of the basis vectors \mathbf{e}_j .

To accomplish this, a new variable $\mathbf{q} = \mathbf{H} \mathbf{p}$ is introduced, where the matrix \mathbf{H} is chosen to transform the boundary conditions at one end of the interval to a simple form such as $\varphi = \varphi' = 0$. With the vector operators giving the boundary conditions at either end of the interval written as \mathbf{B}_j and \mathbf{F}_j , the matrix \mathbf{H} is thus defined so that $\mathbf{F}_1 \cdot \mathbf{H}^{-1} = (1 \ 0 \ 0 \ 0)^T$ and $\mathbf{F}_2 \cdot \mathbf{H}^{-1} = (0 \ 1 \ 0 \ 0)^T$. This modified system is then solved as described above, bearing in mind that the integration routine and boundary conditions \mathbf{B}_j must be modified to take into account the transformation of the variable \mathbf{p} by \mathbf{H} .

§ 5.4 Comparison with known stability results

In geometries bounded by rigid plates we scale velocity on the flow speed of the base flow profile, and lengths on the half channel width (for channels) or the displacement thickness

Comparison with previous stability results, TSI

Case	Present work	Previous result
Plane Poiseuille Flow	$Re_{CR} = 5772.2, k_{CR} = 1.021$	$Re_{CR} = 5772.2, k_{CR} = 1.021$ ¹
Developing Channel Flow, x=100	$Re_{CR} = 9383, k_{CR} = 1.67$	$Re_{CR} = 9790$ ²
x=170	$Re_{CR} = 8330, k_{CR} = 1.34$	$Re_{CR} = 8420$ ²
Single Plate (Blasius) Flow	$Re_{CR} = 519.7, k_{CR} = 0.305$	$Re_{CR} = 520, k_{CR} = 0.301$ ³

Table V.i Comparison of critical Reynolds and wave numbers for TSI in flows with rigid boundaries. ¹: Hughes, in Drazin & Reid 1981 ²: Gupta & Garg 1981 (from their figure 1) ³: Jordinson 1970

(values of k_{CR} for the results of Gupta & Garg are difficult to obtain accurately from their figures and so are omitted.)

of the boundary layer (for flow over a single plate). For flow over a single plate the channel symmetry or antisymmetry conditions are replaced by the requirement that ϕ decay exponentially outside the boundary layer. The appropriate decay rates to require at this point are found from consideration of the Orr-Sommerfeld equation for large z , in which limit the equation has constant coefficients; solutions are thus decaying exponentials, as found in the exact solution for plug flow, with decay rates $m_1 = k$ and $m_2 = (k^2 + i k (1 - c) Re)^{1/2}$ (where $\text{real}(m_2) > 0$ to avoid growing solutions). The boundary conditions requiring that the eigenfunction decay exponentially with these decay rates are

$$\left(\frac{d}{dz} + k\right)\left(\frac{d^2}{dz^2} - m_2^2\right)\phi = 0 \quad \text{and} \quad \left(\frac{d}{dz} + m_2\right)\left(\frac{d^2}{dz^2} - k^2\right)\phi = 0 \quad (5.18)$$

(Carpenter and Garrad 1985). As indicated above, these conditions require that the problem be reformulated before the orthonormalization scheme may be applied.

Ranges of unstable wave numbers, unbounded flow,
single compliant plate

Reynolds Number	present work, range of unstable wavenumbers	C&G, range of unstable wavenumbers
4000	0.050 - 0.130	0.051 - 0.131
	0.142 - 0.344	0.146 - 0.343
4500	0.070 - 0.142	0.069 - 0.145
	0.158 - 0.380	0.159 - 0.380

Table V.ii Comparison of Blasius flutter roots from present and past work, scaled on maximum flow speed and boundary layer displacement thickness. C&G = results of Carpenter and Garrad (1986, from their figure 13). $E=0.5$ Nmm^{-2}

In table V.I we compare with previous work the stability results we obtain for the TSI for Poiseuille and developing channel flow, and for Blasius flow over a single plate, and in figure 5.3 compare the neutral stability curve we obtain for Blasius flow over a single rigid plate with that of Jordinson (1970). The agreement is seen in all cases to be very good; the lack of exact agreement with the developing channel flow results of Gupta and Garg (1981) is due to differences in the representation of the developing flow profile; while we use a perturbation

solution for the profile, they used a finite difference solution of the boundary layer equations.

The numerical solution of the Orr-Sommerfeld equation in a compliant channel may be checked by considering a plug base flow and comparing with the exact solution obtained in Chapter 4. The exact and numerical solutions for this case agree to the numerical precision used.

Finally we seek to duplicate the results of Carpenter and Garrad (1985, 1986) for Blasius flow over a compliant plate. Their results are also obtained using a multiple shooting algorithm with orthonormalization, with a polynomial approximation being used for the Blasius profile. In figure 5.4 points on their neutral stability curve for the TSI (obtained from their figure 11) are shown with the corresponding curve from our solution; in this figure we compare with their choice of wall elastance $E = 0.3 \text{ Nmm}^{-2}$ (see Carpenter and Garrad 1985). We also compare in table V.II ranges of unstable wave numbers for the travelling wave (Type B) flutter instability (Carpenter and Garrad 1986). For either instability the agreement between the present work and previous results is very good.

§5.5 Results

The flutter dispersion relation found numerically for developing flow is shown as a function of the flow speed S in figure 5.5. As with the plug flow base state considered in Chapter 4, there are roots travelling downstream and upstream for small S , which we call roots 1 and 2 respectively; root 1 is shown in figure 5.5. Root 2, as with the plug flow, slows and reverses direction as S is increased, becoming unstable only after the appearance of instability for root 1. The dispersion relation in 5.5 is for symmetric disturbances; that for antisymmetric disturbances is qualitatively similar. Neutral stability curves for both symmetric and antisymmetric disturbances are shown in figure 5.6, showing the symmetric mode to be the least

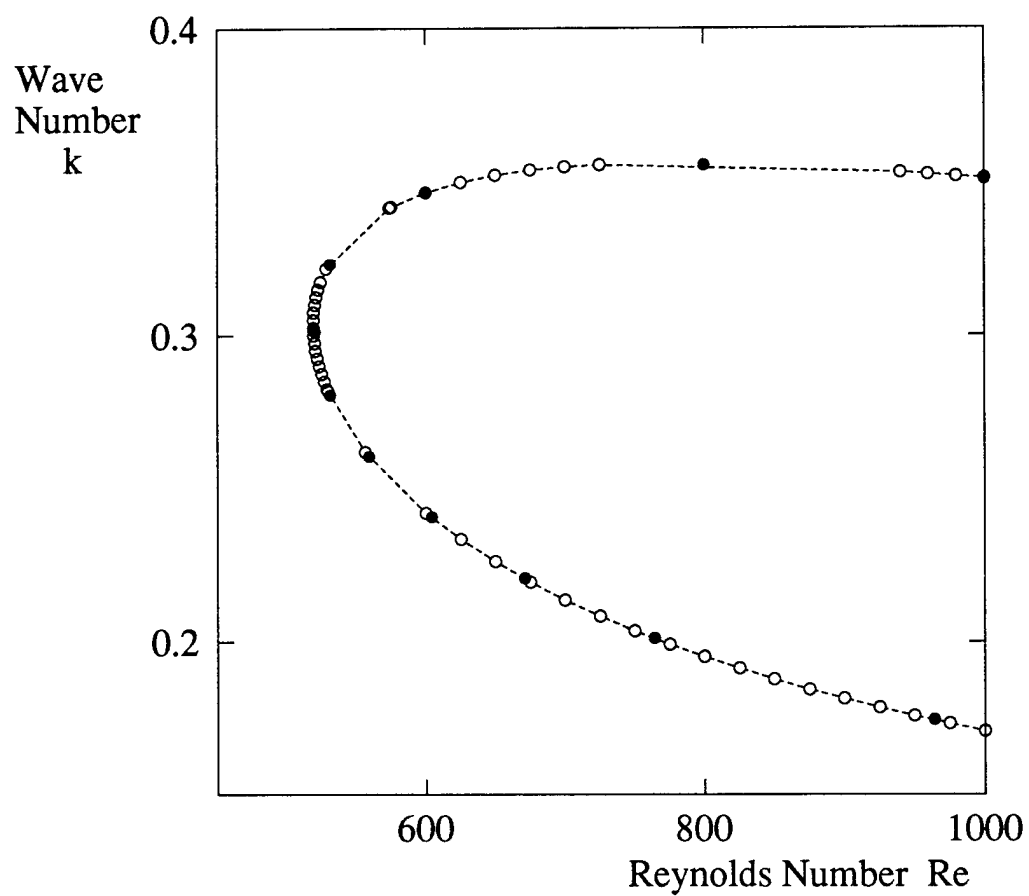


Figure 5.3: Neutral stability curve for Blasius flow over a single rigid plate, TSI.
○ present work; • Jordinson (1970)

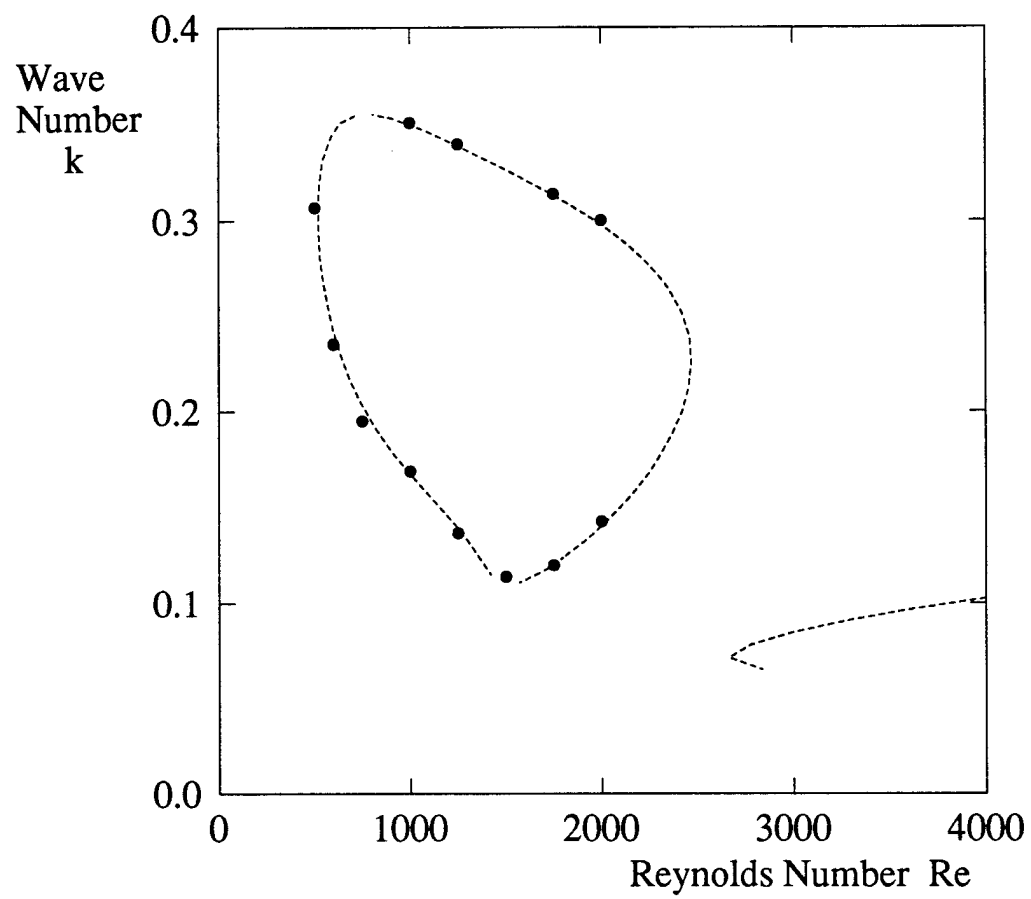


Figure 5.4: Neutral stability curve for Blasius flow over a single compliant plate, TSI. Dashed curve, present work; • Carpenter and Garrad (1985). (Elastance = 0.3Nmm^{-2})

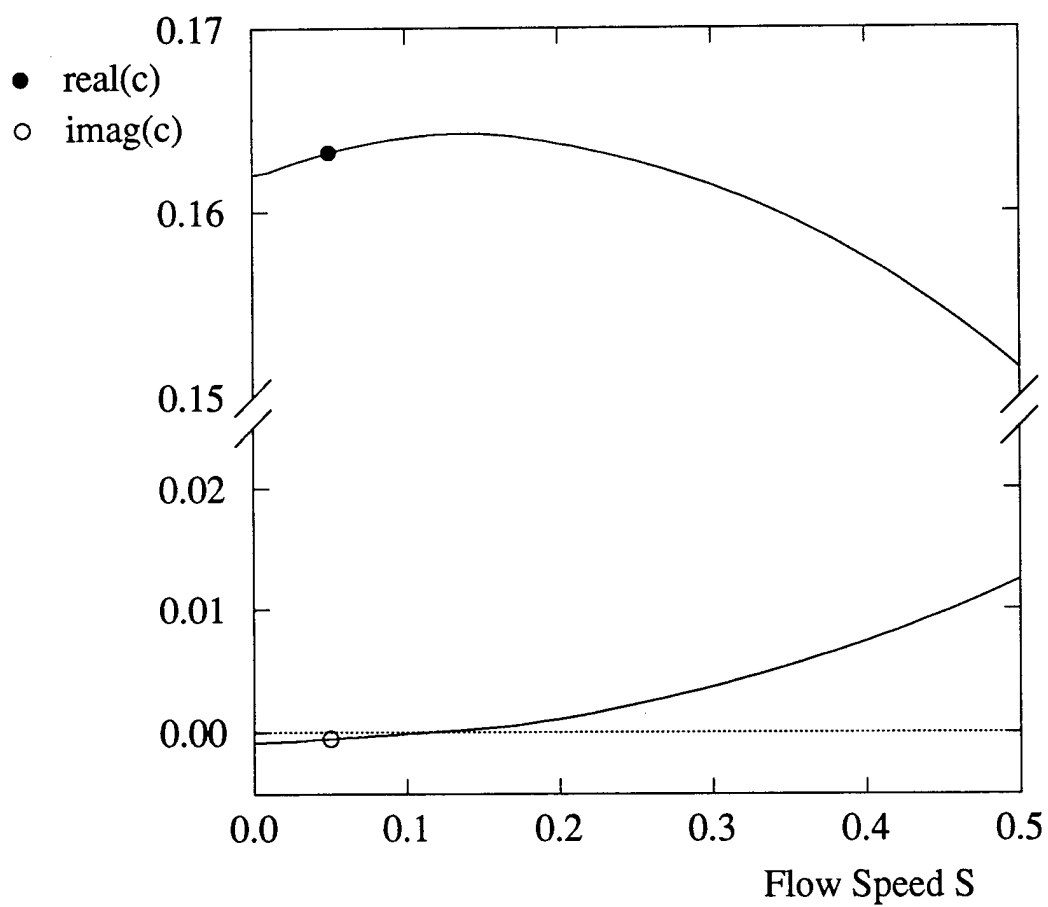


Figure 5.5: Developing flow flutter dispersion relation as a function of flow speed; root 1. $M = 1000$, $B = 50$, $T = 0$, $G = 0.2$, $d = 1000$, $R_w = 1000$, $k = 0.2$, $x_0 = 1.0$.

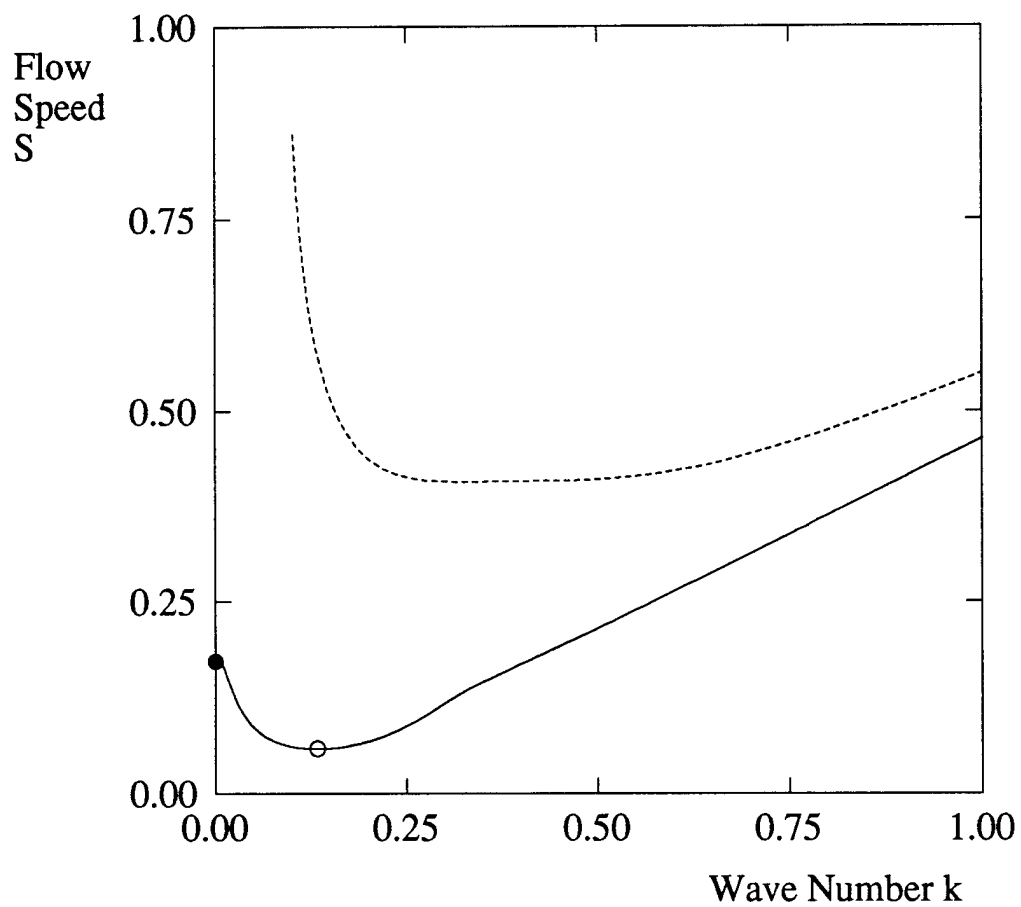


Figure 5.6: Neutral stability curves, flutter instability. Solid curve, symmetric mode; Dashed, antisymmetric. Solid dot gives long wave instability (S_{CR}^{LW}); open dot, flutter (S_{CR}^F). $M = 3190$, $B = 542$, $T = 0$, $G = 0.054$, $d = 882$, $R_w = 2230$, $x_0 = 2.0$.

stable. The long wave limit is shown on the symmetric curve as a solid dot; as shown in §5.2, there is no long wave instability for antisymmetric disturbances. We denote the absolute minimum of the (symmetric) neutral stability curve as S_{CR} and the corresponding value of the wave number as k_{CR} . The critical flow speed for the long wave instability (solid dot) we identify as S_{CR}^{LW} , and the local minimum for $k \neq 0$ (shown in 5.6 with an open dot) as S_{CR}^F , the critical flow speed for flutter. In figure 5.6 $S_{CR} = S_{CR}^F$. Comparison of the developing flow neutral stability curves in figure 5.6 with those for plug flow in figure 4.6 of Chapter 4 shows the qualitative difference that the long wave instability present in the developing flow is absent in the plug flow. The developing flow is also significantly less stable than the plug flow.

As was noted in §5.2, because the critical flow speed for the long wave instability depends on wall characteristics such as the mass ratio M , *etc.*, only at higher orders in k , it is possible by varying system parameters to stabilize the finite wavelength instability and make the long wave instability critical. This is shown in figure 5.7, in which neutral stability curves are shown for a number of different mass ratios. Reduction of the mass ratio M (*e.g.* by reducing the wall density) stabilizes the flutter instability (increases S_{CR}^F), so that the instability moves from non-zero to zero wave number as M is decreased. Once the long wave instability has appeared, further variation in M does not alter the onset flow speed of the instability, as discussed in §5.2 and below. This transition between the finite and long wavelength instabilities admits the appearance of a co-dimension two bifurcation point, occurring when the long wave and flutter instabilities have the same critical flow speed ($S_{CR} = S_{CR}^{LW} = S_{CR}^F$).

In figure 5.8A the effect of varying the wall damping G and mass ratio M on the system is shown by plotting S_{CR}^{LW} and S_{CR}^F as functions of G for two values of M . As G is increased or M decreased, the system is stabilized with respect to flutter (S_{CR}^F increases), but the long wave

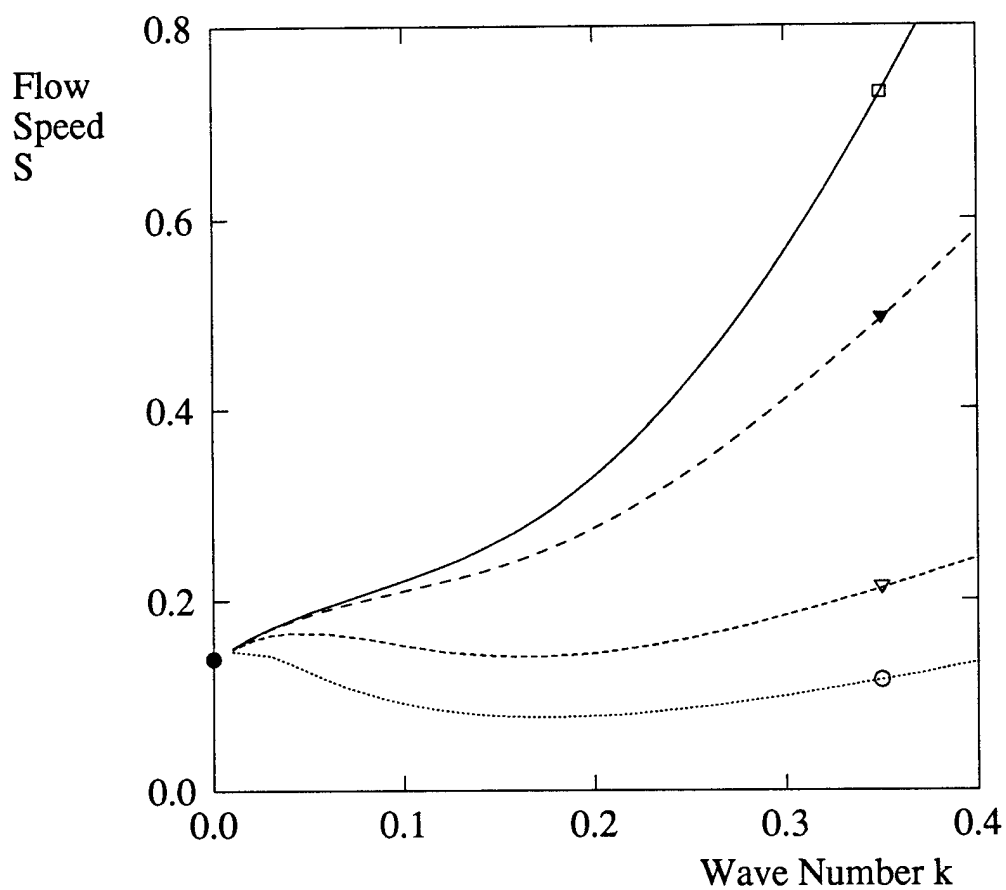


Figure 5.7: Neutral stability curves for different mass ratios, showing long wave and flutter instabilities. Solid dot gives long wave limit. \circ $M = 500$; ∇ $M = 100$; \blacktriangledown $M = 10$; \square $M = 1$. $B = 542$, $T = 0$, $\hat{G} \times 5000 = 0.0845$, $d = 882$, $R_w = 2230$, $x_0 = 1.0$. ($\hat{G} \equiv b^* G^* / \hat{u}$)

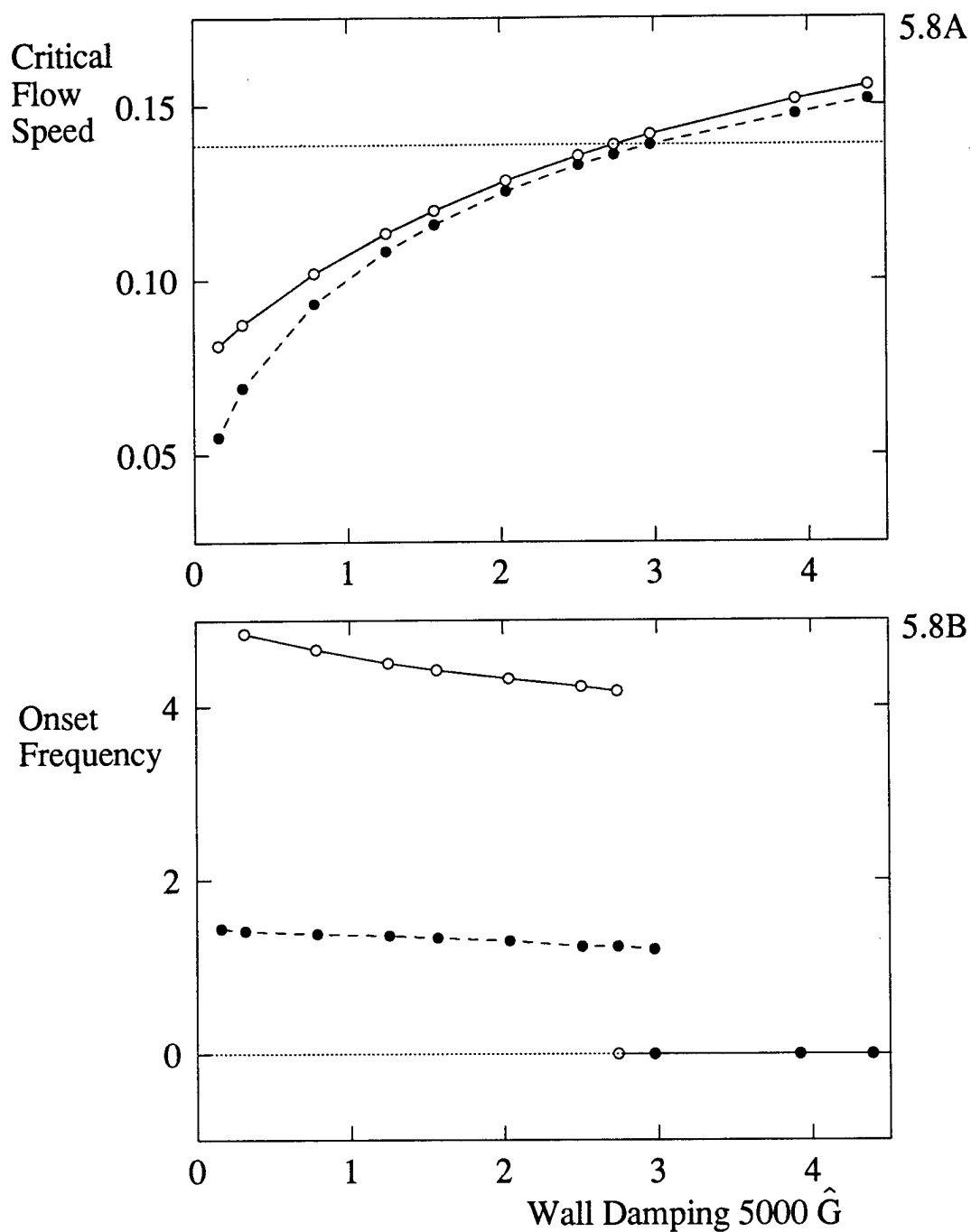


Figure 5.8: Critical flow speeds S_{CR}^{LW} and S_{CR}^F (5.8A) and frequency at S_{CR} (5.8B) as functions of wall damping and mass ratio. Dotted line gives S_{CR}^{LW} ; Symbols give S_{CR}^F in 5.8A and frequency in 5.8B: \circ $M = 5000$; \bullet $M = 500$. $B = 542$, $T = 0$, $d = 882$, $R_w = 2230$, $x_0 = 1.0$.

limit (S_{CR}^{LW}) is unchanged, so that for large wall damping stability is lost to the long wave instability. The stabilization of the flutter instability is consistent with its being Type B, and being stabilized by reduction of wall inertia. Note that 5.8A is qualitatively different than the behavior of the plug base flow shown in figure 4.7A and discussed in §4.4, for which the effect of increasing M could be stabilizing for large G because of the plug flow long wave stability. Figure 5.8B shows the frequency of the oscillations appearing for developing flow at S_{CR} . The behavior of the frequency is similar to that seen for plug flow (figure 4.7B), decreasing with increasing M or G , until the appearance of the long wave instability results in a discontinuous drop to zero frequency.

Figure 5.9A shows S_{CR}^F versus wall elastance E (nondimensionalized on $(\rho^* v^{*2} / b^{*3}) \times 10^4$) for two values of the wall flexural rigidity B . For the parameter values considered, $S_{CR} = S_{CR}^F$. The frequency of the oscillations appearing at S_{CR} is shown in figure 5.9B. Stiffening the wall by increasing either E or B increases both S_{CR} and the corresponding frequency of oscillations; this is similar to the results for plug flow (figure 4.8) and is expected physically. Note that the frequency in 5.9B, as that in 4.8B, increases approximately as $E^{1/2}$, consistent with the results of Grotberg and Reiss (1984). The inset plots in 5.9 show the difference between the values of S_{CR}^F for the two values of B (in 5.9A) and the corresponding difference in frequency (in 5.9B), showing that the effect of B is larger for larger wall elastance, for which the instability has shorter wavelength. This is as expected, and a similar effect may be obtained through variation of the wall tension T . Note that the second wall stiffness parameter, d , is not independent of B , varying only by a factor of 12 $(b^* / h^*)^2$; we have retained it as a second parameter only to facilitate comparison with the results obtained for the limit of no horizontal wall motion (which corresponds to $d^{-1} \rightarrow 0$). We find little difference between the cases $d^{-1} = 0$

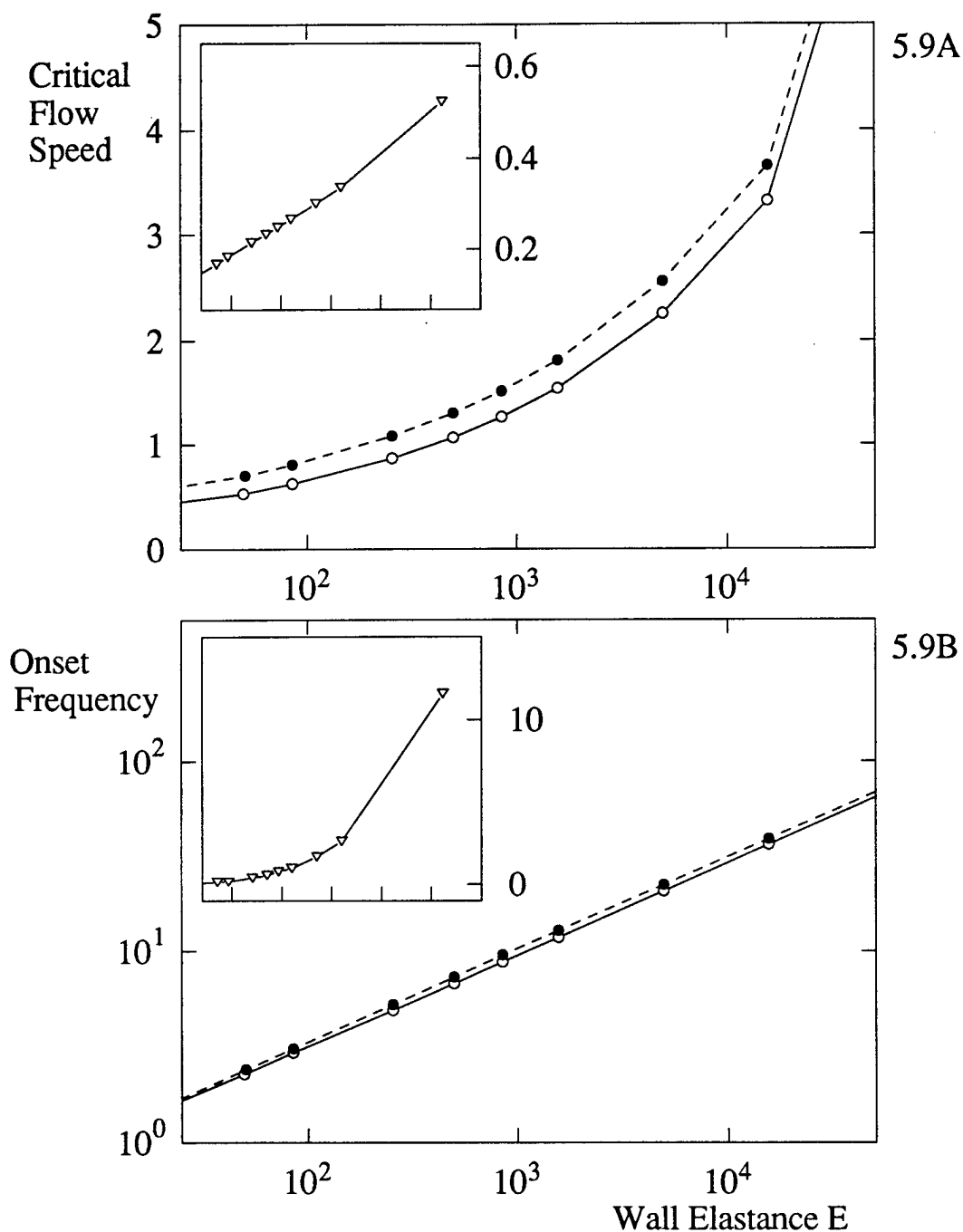


Figure 5.9: Critical flow speed $S_{CR} (= S_{CR}^F)$ (5.9A) and flutter frequency (5.9B) as functions of wall elastance E . Elastance scaled on $(\rho^* v^{*2} / b^{*3}) \times 10^4$, velocity on $(v^* / b^*) \times 10^2$, frequency on (v^* / b^{*2}) . \circ $B = 2.688 \times 10^4$; \bullet $B = 2.688 \times 10^5$. Inset plots give the difference between S_{CR} and f_{CR} for the two values of B , as a function of E . Other parameters as figure 5.7 ($M = 3190$), with modified scaling.

and $d^{-1} \neq 0$.

Because the half-channel width b^* also appears in the scaling of the problem, to examine the effect of changing b^* we scale the system as noted in §5.2, scaling lengths on x_0^* and velocities on $(v^* / x_0^*) \times 10^2$. Figure 5.10 shows the neutral stability curves for a number of different half channel widths b ; as b is increased, the effect of the second plate and hence of viscosity in the channel is decreased, which stabilizes the Type B flutter. However, as indicated in §5.2, the long wave instability continues to appear at lower flow speeds, so that for sufficiently wide channels instability will be lost to the long wave instability. This is seen in figure 5.1, which shows S_{CR}^{LW} and S_{CR}^F as functions of b ; we see that as b is increased past ≈ 9 the instability goes from the flutter to the long wavelength instability. This is particularly interesting in light of the experimental observations (Gavriely *et.al.* 1989) that flutter only occurs following tube collapse; we hypothesize that this tube collapse is the physical manifestation of the long wave instability and that flutter is then seen only when the channel width is reduced enough that it may become critical. As the wall elastance (\check{R}_w) is increased, the codimension two point moves to larger channel widths. This is consistent with physical observations of flutter in stiffer tubes, which do not collapse; the shift in the location of the codimension two point in this case is evidently sufficient to ensure the appearance of the flutter instability. With increasing half-channel width, the perturbation solution for the developing flow that we are using converges to Blasius flow over a single compliant plate, and the stability results for the single plate system (*e.g.* Carpenter and Garrad 1986) are recovered for the finite wave number instability. However, for long waves the effect of the opposing channel wall is always significant, so that the single plate limit is not reached; this is shown in figure 5.10 through the inclusion of a stability curve for Blasius flow over a single compliant plate. We discuss the effect of increasing channel width

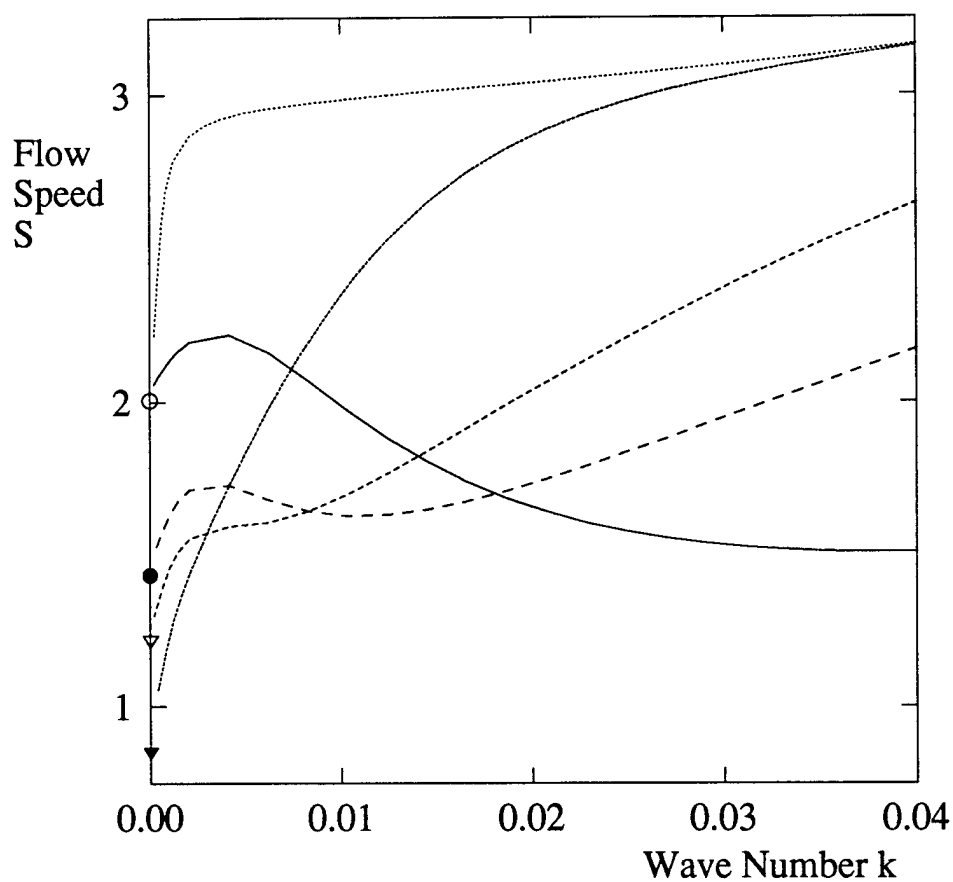


Figure 5.10: Neutral stability curves for different channel widths, showing long wave instability and comparison with Blasius flow over a single compliant plate. Lengths scaled on x_0^* , velocities on $(v^* / x_0^*) \times 10^2$. \circ $b = 4.82$; \bullet $b = 14.5$; ∇ $b = 24.1$; \blacktriangledown $b = 72.4$; dotted curve is for Blasius flow over a single compliant plate. Other parameters as figure 5.7 ($M = 3190$), with modified scaling.

in slightly greater detail in §5.6. Figure 5.1A may also be compared with figure 4.9A of Chapter 4, which shows S_{cr}^F for plug flow as a function of half channel width. The behavior of the critical flow speed is similar for either base flow, except for the long wave instability which is absent for plug flow. Comparing 5.1B and 4.9B, the change in flutter frequency is also similar for narrower channels; however, for wider channels, the effect of the long wave instability is seen for the developing flow while the plug flow long wave stability increases the plug flow frequency as discussed in §4.4.

Because increasing the Reynolds number of the flow is equivalent to decreasing the fluid viscosity, such an increase stabilizes the flutter instability. However, in the case of the developing profile, increasing the Reynolds number also changes the base flow profile, causing (for constant flow speed S and axial position x_0) a narrowing of the boundary layer at the wall. A similar effect may be obtained by decreasing x_0 ; this destabilizes the flutter instability. It is difficult to draw conclusions for wide ranges of axial positions, however, due to limitations imposed by the downstream limit of validity for our developing profile. Further, as points farther upstream are considered, non-parallelism in the flow may become significant; we return to this issue in the discussion in Chapter 7.

As noted in Chapter 4, the effects that we find destabilize the flutter instability correspond with the distinguishing characteristics of the lung airways of wheezing patients. For developing flow, however, there is also the long wave instability, which we expect is related to tube collapse, and hence flow limitation. As wide channels are more susceptible to the long wave instability than to flutter, this agrees with clinical observations that forced expiratory wheezes are only seen following flow limitation (Gavriely *et.al.* 1987). In Chapter 6 we compare the theoretical results from the developing flow model with experimental results.

§5.6 Discussion of the limit of infinite channel width

To consider results for very wide channels, it is convenient to investigate the effect of increasing channel width on the flutter dispersion relation shown in figure 5.5. In this figure the eigenvalue c is seen to change smoothly with increasing flow speed; however, as the half channel width b is increased, there appears near the point at which the base flow speed becomes equal to the phase speed of the disturbance an abrupt drop in the phase speed and upward bend in the growth rate of the disturbance. As b is increased still further, this becomes an actual discontinuity; this is shown in figure 5.11A. To illustrate this more clearly, figure 5.11B shows the eigenvalue in the complex c plane; in this form, $\text{imag}(c)$ is given as a function of $\text{real}(c)$, with flow speed S parameterizing the curves (only the region of parameter space about $S = \text{real}(c)$ is shown). The dependence of this behavior on the condition $S = \text{real}(c)$ is emphasized by scaling c on the maximum flow speed of the base flow, so that the line $S = \text{real}(c)$ lies along $\text{real}(c) = 1$. Similar behavior may be obtained by varying other system parameters; this occurs when the effective channel width is very large (*e.g.* the mass ratio M goes as $(b^*)^{-1}$, so that decreasing M may be interpreted as increasing the channel width, subject to variation of other parameter values).

To understand this behavior, it is useful to consider more specifically the characteristics of the Orr-Sommerfeld system in bounded and unbounded domains. In an unbounded domain, unlike the finite case, there are only a finite number of eigenvalues in the discrete spectrum (Miklavčič 1983), and these are supplemented by a continuous spectrum consisting of 'improper' eigenvalues having phase speeds equal to the maximum flow speed of the base profile and negative growth rates (Grosch and Salwan 1978; Craik 1991). As the Reynolds number of the

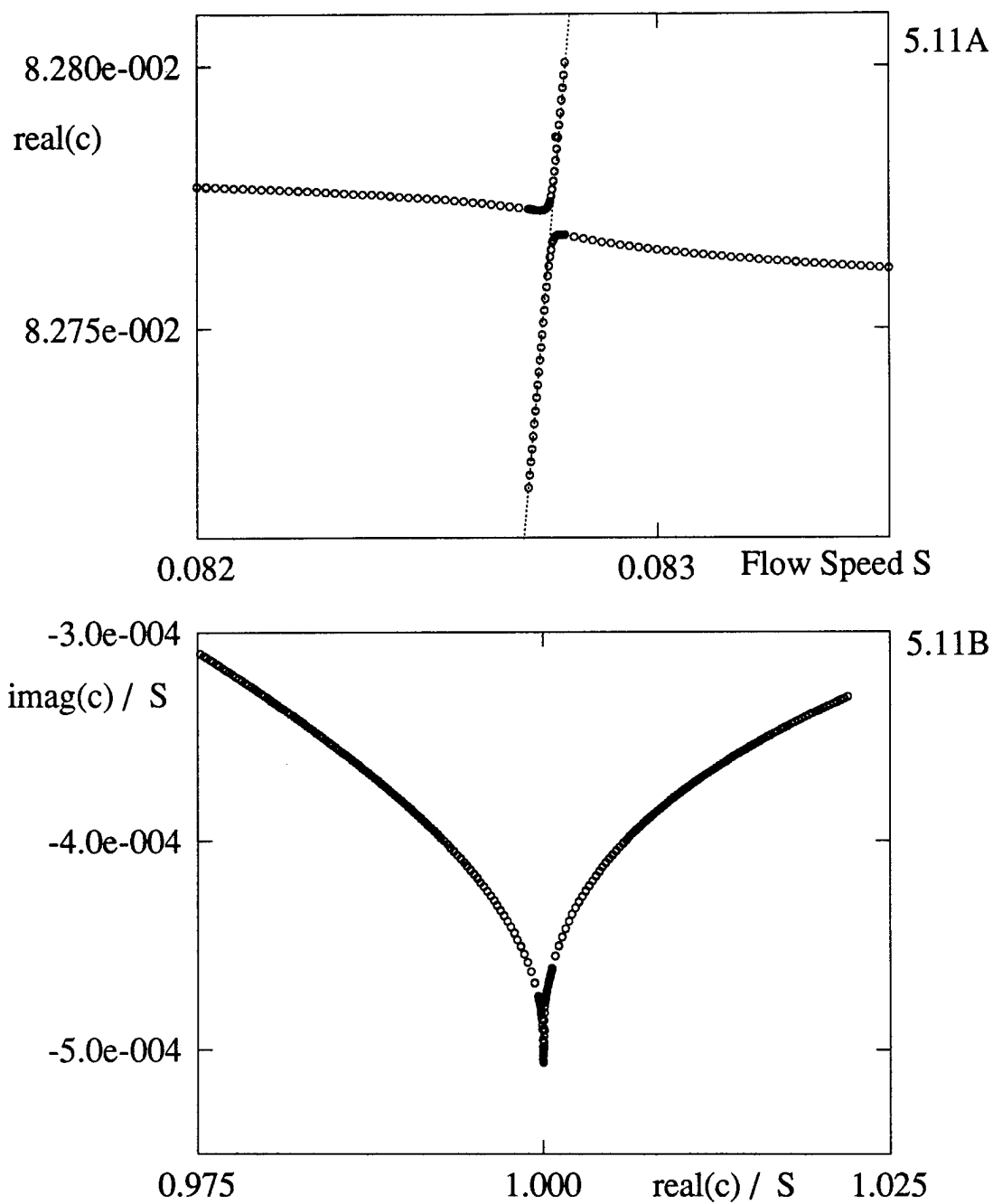


Figure 5.11: Dispersion relation for developing flow in a very wide channel, showing singularity at $S = \text{real}(c)$. Dotted line gives $S = \text{real}(c)$.

flow is increased, eigenvalues are added to the discrete spectrum, appearing sequentially at the line in the complex c plane giving the continuous spectrum (Mack 1976). For Blasius flow over a rigid plate, the only eigenvalues in the vicinity of the continuous spectrum are significantly damped, but this is not the case when a flexible wall is considered. In this case the Type B flutter mode (which is our root 1) may be critical, and may have a phase speed that approaches the speed of the base flow. The presence of the continuous spectrum then complicates matters, as it is difficult to accurately locate eigenvalues near the continuous spectrum (Carpenter and Garrad 1986). In a finite domain there is no continuous spectrum (Lin 1961), and this difficulty does not arise, but as the finite domain is modified to look more like the infinite case (when the channel width is increased, or other parameters varied to obtain a similar result) it may be expected that the numerical solution to the problem might encounter difficulties as the phase speed of the disturbance becomes similar to the flow speed of the base flow, as seen in figure 5.11.

CHAPTER 6: COMPARISONS WITH EXPERIMENTS

§6.1 Overview

As the motivation for this study is to model the oscillatory instabilities in the lung airways that lead to wheezing lung sounds, we would like to compare our theoretical predictions with actual experimental observations of such wheezing. However, the characteristics of the lung airways that we need to obtain the parameters in our model (M , B , *etc.*) are not known with any accuracy, making such comparison difficult. We therefore first consider the theoretical modelling of experiments with flexible tubes, in §6.2 - §6.4, and return to the issue of the lung in §6.5. In that Gavriely *et.al.* (1987, 1989) have demonstrated that the characteristics of both the collapse phenomenon and the sounds produced in such tubes are similar to those in the lung, this comparison may itself indicate that our model is applicable to the lung and shed insight on the lung experiments.

§6.2 Comparison with flutter in tube experiments

Gavriely *et.al.* (1989) experimentally investigated air-conducting flexible tubes, and found an oscillatory instability that followed tube collapse. Based on the characteristics they give for their tubes and flow ($h^*=0.19\text{cm}$, $b^*=0.07\text{cm}$ (after collapse, at the onset of flutter), $\rho_w^*=0.941\text{g/cm}^3$, $\rho^*=8\times 10^{-4}\text{g/cm}^3$, $v^*=0.225\text{cm}^2/\text{s}$, $T^*=0$, $G^*=1.72\text{s}^{-1}$, $E^*=5.86\times 10^5\text{ dyne/cm}^3$, and $D^*=Y^*h^{*3}/9$ (where Y^* =the Young's modulus)= 7621dyne cm), we find the following non-dimensional parameter values for our model: $M = 3190$, $B = 542$, $T = 0$, $G = 0.0542$, $d = 882$, and $R_w = 2230$. For the experimental case for which these parameter values were derived, the critical flow speed at which the oscillatory instability was first observed was 2670cm/s ; this value

was obtained by averaging the flow rate over the cross-sectional area of the tube. The symmetric instability appearing at this flow speed had a frequency of 300Hz.

To obtain results using our developing flow model, it is necessary not only to use the parameter values indicated above, but also to select an axial position at which to evaluate the developing flow profile. In the experiments a long (60cm) flexible tube was fastened at either end to a rigid pipe, and air flow through the tube was induced by a suction pump at the downstream end. As the driving pressure gradient was increased, collapse and flutter occurred at the downstream end of the tube. The development length for a tube is $x_{ENT} = 0.25 r^*{}^2 u_{AVG}^* / \nu^*$ (where r^* is the tube radius and u_{AVG}^* the average fluid velocity) (Schlichting 1955); for the experiment the uncollapsed tube radius $r^* = 0.325\text{cm}$, $\nu^* = 0.225\text{cm}^2/\text{s}$, and $u_{AVG}^* = 1600\text{cm/s}$, so that $x_{ENT} = 188\text{cm}$. Thus it is clearly appropriate to consider the flow in the collapsed tube section to be developing. However, the precise appearance of the profile is unclear, as when the flow enters the collapsed section it regains a more pronounced boundary layer character due to the constriction. We therefore calculate the stability of the system at several axial locations, and also compare with the results for fully developed flow; an additional comparison is then made with the predictions of the plug flow solution.

The predicted flutter frequencies for a developing flow at axial positions $x = 1, 2$ and 3 half channel widths (recall that it is necessary that we consider x_0 small for the for the developing profile to be valid; this requirement is slightly less stringent than $x_0 < 3$) are 312Hz, 311Hz, and 310Hz; for Poiseuille flow, 308Hz; and for plug flow, 333Hz. The numerical predictions for the viscous (developing or Poiseuille) profiles are thus all quite close to the experimental value, while the plug flow result is higher. That is should be larger than the numerical values is, however, reasonable from the trend, seen in the frequencies for the developing flow, of increasing

frequency with decreasing axial position.

The critical flow speeds S_{CR}^F corresponding to the frequencies above are for the developing flow 344cm/s, 417cm/s and 463cm/s (at $x_0 = 1, 2$, and 3); for Poiseuille flow, 540cm/s; and for plug flow, 1,488cm/s. It is not appropriate to directly compare the theoretical and experimental flow speeds, however, as the value measured experimentally (2670cm/s) is an average over a collapsed tube cross-section. As this cross-section is a dumbbell-like shape, the velocity in the central (channel) section of the collapsed tube (where the oscillations appear) will be lower than that in the outer lobes because of viscous resistance.

To estimate the degree to which the channel flow speed might differ from the experimentally measured cross-sectional average, we use the finite elements package FIDAP to calculate the velocity profile in a collapsed tube cross-section. This requires, however, knowledge of the dimensions of the collapsed tube section, which are not reported by Gavriely *et.al* (1989); dimensions that are given are the half-channel width (0.07cm) and cross-sectional area (0.2cm²). Flaherty *et.al.* (1972) numerically obtained shapes for collapsed tubes, to which the experimental dimensions might be matched, but their model is for a tube with walls of negligible width while in the experiments the width of the tube wall (0.19cm) was a substantial percentage of the uncollapsed radius (0.325cm). We therefore consider two approximate collapsed tube shapes based on the dimensions that are given and the results of Flaherty *et.al.*; the two differ in that the second is flatter, with smaller side lobes and a longer channel section. By considering the two, we obtain a qualitative estimate of how the tube shape may influence the flow speeds in the cross-section. As the imprecision in estimating the tube shape and dimensions itself prevents the velocity calculation from being quantitative, only fully developed flow is considered, as this results in an order of magnitude decrease in the required computational resources from those

necessary for the calculation of developing flow. Details of the FIDAP calculation appear in Appendix B. For the flow rate of the experiment ($533\text{cm}^3/\text{s}$), the average velocity in the channel section of the two shapes is found to be 1440cm/s and 1010cm/s , respectively. These calculations thus indicate that the velocity at the center of the collapsed tube section may be significantly lower than the cross-sectionally averaged value determined in the experiments, and thus that the actual channel flow speed in the experiments was likely to have been closer to our theoretical predictions.

An additional complication in this comparison arises from the geometry of the collapse itself, which results in both a constriction (in the transverse dimension of the channel) and expansion (out of the channel, into the side lobes of the dumbbell) of the tube. The TSI is stabilized for flow into a constriction (White 1974), but the effect of a lateral expansion (and the resulting three dimensionality of the flow) has not to our knowledge been investigated even for the TSI (let alone flutter). Neither of these effects are included in our model, and they may, along with the variation in flow speeds investigated above, reconcile the difference between the theoretical and experimental critical flow speeds.

§6.3 *Comparison with collapse in tube experiments*

Next, we seek to compare the experimentally observed flow speed at which tube collapse began with the long wave onset flow speed we find theoretically. It is difficult to determine the experimental value from Gavriely *et.al.* (1989), as they did not report the critical flow speeds for tube collapse. However, we estimate the beginning of collapse to be when the pressure - flow-rate relationship they show first deviates from the slow linear increase seen before collapse and flow limitation. From their figure 3.B, this gives a critical flow rate of approximately 27 l/min ,

or an average flow speed S_{CR}^{LWexp} (recalling that the uncollapsed tube radius was 0.325cm) of 1340cm/s. Reading from our figure 5.1, we find for this channel width that the long wave instability is critical, with S_{CR}^{LW} of about 680cm/s, or roughly half of the estimate from the experiments. Thus the developing flow model accurately predicts the existence of the long wave (collapse) instability. In that the comparison between the theoretical and experimental critical flow rates is at best qualitative, due to the nature of our experimental estimate and the fact that before collapse it may be less appropriate to model the tube as a channel, we conclude that there is evidence to support our hypothesis that tube collapse is related to the long wave instability.

§6.4 *The TSI in the tube experiments*

Two observations verify that the flutter instability investigated above is that which is relevant to the tube experiments. First, the experimentally observed instability is symmetric, while the TSI is antisymmetric, and second, we also numerically calculate the critical flow speed for the TSI to demonstrate that it occurs for much higher flow speeds. This critical Reynolds number (scaled on maximum flow velocity and half channel width) is $Re_{CR} = 5761$, which is equivalent to an average flow speed of approximately 18,500cm/s, which is far in excess of both the experimentally measured and theoretically predicted critical flow speeds for flutter. The frequency of the oscillation for the instability is 11,360Hz at criticality, which is again several orders of magnitude larger than the experimental or theoretical values. These calculations are for Poiseuille flow; the critical Reynolds numbers for the TSI in developing flows are much higher (Chen and Sparrow 1967).

§6.5 Comparison with wheezing in the lung

We now turn to the issue of modelling wheezing in the lung. For this comparison we consider experiments with forced expiratory wheezes (Gavriely *et.al.* 1987) for which wheeze frequencies and flow rates were reported. The subjects in this study executed forced expiratory maneuvers to produce wheezing sounds; a controlled suction pump was used to facilitate the production of the wheezes, which had frequencies of 580-2730Hz. The volume flow rate of the expirations was on the order of 1 l/s. Wheezes were measured with a tracheal microphone, but the actual location of the wheezes in the lung is not indicated. Kramen (1983) also investigated forced expiratory wheezes, though without mechanical forcing, and found them to occur between the trachea and lobar bronchi. The frequencies of the wheezes reported by Kramen are similar to those of Gavriely *et.al.*, as are those in the limited forced expiratory experiment of Hinchey and Snellen (1987).

To apply our theoretical models to these experiments, we need estimates for the physical characteristics of the airways in question. Dragon and Grotberg (1991) suggest for the trachea $r^* = 0.9\text{cm}$ (uncollapsed radius), $h^* = 0.05\text{cm}$, $\rho_w^* = 0.997\text{g/cm}^3$, $G^* = 5\text{s}^{-1}$, and E^* up to 2.8×10^7 dyne/cm², with $v^* = 0.15\text{cm}^2/\text{s}$ and $\rho^* = 0.00114\text{g/cm}^3$. For the bronchi, we expect the elastance E^* to be lower, and the radii r^* to be smaller; Olson *et.al.* (1970) give $r^* = 0.65\text{cm}$, 0.47cm and 0.36cm for the first three generations of bronchi. To estimate a Youngs modulus Y^* for the trachea, and collapsed 'channel-width' for the airways, we assume that the ratios Y^*/E^* (≈ 200) and b^*/r^* (≈ 0.215) for tube experiments (Gavriely *et.al.* 1989) may be applied to the lung. We find E^* and Y^* for the bronchi by decreasing the corresponding values for the trachea by a factor of 5 for each airway generation. Values of h^* for the bronchi are found by letting the ratio of h^* to r^* be the same as for the trachea. Finally, we take for the trachea $E^* = 1 \times 10^6$ dyne/cm². Our estimates for

parameter	Trachea	1° Bronchi	2° Bronchi	3° Bronchi
r^*	0.90cm	0.65cm	0.47cm	0.36cm
b^*	0.19cm	0.14cm	0.10cm	0.077cm
h^*	0.05cm	0.04cm	0.03cm	0.02cm
(1) ρ_w^*	0.997g/cm ³	0.9g/cm ³	0.9g/cm ³	0.9g/cm ³
(2) G^*	5s ⁻¹	5s ⁻¹	5s ⁻¹	5s ⁻¹
E^* (dyne/cm ²)	1×10 ⁶	2×10 ⁵	4×10 ⁴	8×10 ³
Y^* (dyne/cm ²)	2×10 ⁸	4×10 ⁷	8×10 ⁶	1.6×10 ⁶
\bar{u}	29,620cm/s	13,250cm/s	5,923cm/s	2,649cm/s
M	230	226	237	205
B	2.13	3.70	6.00	5.06
(3) T	0	0	0	0
G	7.38×10 ⁻³	0.0119	0.0200	0.0298
d	369	544	800	899
R_w	37,515	12,362	3,950	1,360

Table VI.i: Dimensional and non-dimensional parameters for lung airways. (1): density of the bronchi is assumed to be somewhat less than that of the trachea, but of similar magnitude. (2): wall damping is arbitrarily taken to be constant for all airway generations. (3): we initially assume zero longitudinal wall tension for all airways.

the airway characteristics and the corresponding dimensional and non-dimensional parameters used in our models are summarized in table VI.i.

In table VI.ii we present results from the developing and plug flow models of Chapters 4 and 5 for the parameter values indicated in table VI.i. Because of the crude nature of some of the estimates leading to those parameter values, we also show results for some other values. The values for the flutter frequencies in the table may be compared with the experimental values (580-

parameter set:	Trachea	1° Bronchi	2° Bronchi	3° Bronchi
Devel. Flow ($x_0=2$)	f_{CR}^*	1646Hz	1011Hz	619Hz
	S_{CR}^{F*}	2308cm/s	1183cm/s	593cm/s
	S_{CR}^{LW*}	2395cm/s	1634cm/s	878cm/s
Plug Flow	f_{CR}^*	1808Hz	1117Hz	687Hz
	S_{CR}^{F*}	9544cm/s	4350cm/s	1934cm/s
parameter set:	2° Bronchi†	2° Bronchi‡	2° Bronchi††	2° Bronchi‡‡
Devel. Flow ($x_0=2$)	f_{CR}^*	672Hz	896Hz	508Hz
	S_{CR}^{F*}	399cm/s	568cm/s	547cm/s
	S_{CR}^{LW*}	878cm/s	878cm/s	609cm/s
Plug Flow	f_{CR}^*	765Hz	1116Hz	607Hz
	S_{CR}^{F*}	1236cm/s	2005cm/s	2204cm/s

Table VI.ii: Theoretically predicted flutter frequencies and critical flow rates for the parameters indicated in table VI.i. †,‡: parameter values as 2° Bronchi, table VI.i, with †: $G^*=1s^{-1}$; ‡: $G^*=1s^{-1}$, $T=10$; ††: $E^*=2.041 \times 10^4$, $T=10$; ‡‡: $E^*=2.041 \times 10^4$, $T=10$.

2730Hz), and are seen to agree quite well. As noted in §6.2, it is difficult to compare our theoretically predicted critical flow speeds with experimental values, and this difficulty is even greater for the lung experiments, for which even the collapsed tube cross-sectional area is not known. It is worth noting, however, that flutter (rather than the long wave collapse) is predicted for the developing flow, consistent with our modelling already collapsed airways. If we assume that the ratio of collapsed to uncollapsed tube cross-sectional area ($A_{COL} / \pi r^{*2}$) is similar for the lung airways and tube experiments (of Gavriely *et.al.* 1989), we have $A_{COL}=1.53cm^2$ for the trachea, and $=0.80cm^2$, $0.42cm^2$ and $0.41cm^2$ for the first three generations of bronchi. For a 1 l/s

expiratory flow rate, then, the average flow speed through a collapsed trachea would be 653cm/s; through the bronchi (noting that there are 2, 4, and 7 bronchi in the first 3 generations of bronchi (Olson *et.al.* 1970)), 625cm/s, 595cm/s and 348cm/s, respectively. Based on the comparison with flutter in tube experiments (§6.2) and the imprecision in these estimates, we expect the theoretically predicted flow speeds for the developing flow to be on the order of or somewhat lower than these values, which we seen in Table V.ii to be the case. It is thus reasonable that the experimentally observed wheezing sounds were in fact the result of flutter in the lung airways.

CHAPTER 7: CONCLUSIONS AND DISCUSSION

§7.1 *Summary*

Motivated by the fluid dynamic flutter instability seen in flexible tubes and wheezing lung sounds, we have investigated the linear stability of a compliant channel conveying a developing flow. This flow profile was approximated by a plug flow, for which analytical solutions are possible, and with a perturbation solution (valid in the upstream region of the channel), based on the Blasius profile, for which we obtained analytical long wave results and numerical results for arbitrary wavelengths.

The study of the perturbation solution showed the existence of both a finite wavelength (flutter) and long wave (collapse) instability, which may appear independently or simultaneously, the latter case resulting in a codimension two bifurcation point from the base flow. The long wave instability is not present for our plug flow solution, as it requires a non-uniform base flow profile; for this reason it has not been seen in previous channel studies. We expect that the long wave instability corresponds to the tube collapse seen prior to oscillatory instabilities in tube experiments, and hence to flow limitation in tubes and the lung.

We have examined the effect of varying different parameters on the stability of the system and found, in particular, that effects destabilizing the flutter instability are those which would be expected to characterize the lungs of individuals who are more prone to wheezing, thus providing further corroboration for the theory that wheezing is symptomatic of airway flutter. Further, the long wave (collapse) instability is more likely to occur in wider channels, and is hence likely to appear before the flutter instability, as seen in experiments.

We thus conclude, in light of the good agreement between theoretically predicted and

experimentally observed flutter frequencies seen in Chapter 6, that we have further theoretical support for the causal relationship between airway flutter and wheezing lung sounds. We have also found qualitative support for collapse and flow limitation being the manifestation of a long-wave wall-fluid instability. In the remainder of this chapter we discuss some issues related to this work. In §7.2, we discuss the Tollmien-Schlichting (viscous fluid) instability, and in §7.3 the issue of nonparallelism in the base flow is considered. We conclude in §7.4 with a brief outline of some possible extensions of the present work.

§7.2 *Discussion of the Tollmien Schlichting instability*

It is clear from the investigation in §6.2 of the TSI in the context of the tube experiments of Gavriely *et.al.* (1989) that the TSI is not likely to appear for the thick walled, air-conveying tubes with which we are concerned for the present study. However, in other systems, *e.g.* when the ratio of wall and fluid densities are similar (so that the mass ratio is closer to unity), or the wall elastance is higher, the TSI may be significant. While this is not the case in the lung airways, it is for many engineering applications and for physiological applications such as blood flow. In the latter, however, the flows are likely to be fully developed, and in arterial flows significantly pulsatile. As noted in Chapter 2, the effect of compliant boundaries on the TSI for plane Poiseuille flow has been considered by Hains and Price (1962) and others, and nonlinear stability calculations have been done by Rotenberry and Saffman (1990) and Rotenberry (1992). However, the stability of pulsatile flows with compliant boundaries has to date not been considered.

§7.3 The effect of nonparallelism in the base flow

The derivation of the Orr-Sommerfeld equation, as indicated in Chapter 3, requires that the base profile considered be parallel, that is, a function only of the transverse coordinate. When we approximate the developing profile with a plug flow the nonparallelism in the base flow is moot, but this is not the case when a true developing profile such as our perturbation solution is considered. In this case we assume that the flow is locally parallel, so that transverse changes in the flow are small and may be neglected. This requires that we choose the axial position x_0 at which the profile is evaluated so that the change of the boundary layer thickness over a disturbance wavelength is small by comparison to the channel width. More precisely, it should be the case that $\delta(x_0 + \Delta x) - \delta(x_0) \ll 1$, where $\delta(x_0)$ is the boundary layer width (nondimensionalized on half channel width) a nondimensional distance x_0 downstream from the mouth of the channel and $\Delta x = 2\pi/k$ is the nondimensional disturbance wavelength. Similarity analysis of the boundary layer equations gives $\delta(x_0) \approx 5 (v^* x_0^* / \hat{u} b^2)^{1/2}$ (see, for example, Schlichting 1955); with this the condition for slow variation of $\delta(x_0)$ reduces in a straightforward manner to

$$\frac{2\pi}{k R_w S} \ll \frac{1}{25} \left(1 + 10 \left(\frac{x_0}{R_w S} \right)^{1/2} \right). \quad (7.1)$$

The requirement for the developing flow profile itself to be valid, *i.e.* that the axial position being considered be downstream of the leading edge of the channel wall, is $x_0 \gg (R_w S)^{-1}$ (Batchelor 1967), which is in general less stringent than (7.1). For the developing flow profile that we use, the axial position x_0 considered must also satisfy the requirement $x_0 < 0.02 R_w S$ (*c.f.* §3.3). We are not guaranteed in advance, however, that on satisfying this condition (7.1) will also be satisfied, and in the long wave limit ($k \rightarrow 0$) it will be impossible to satisfy (7.1). We therefore

consider here the effect of nonparallelism on the stability calculation. For the TSI non-parallel effects have been shown to be destabilizing for Blasius flow over a single wall (Gaster 1974, Saric and Nayfeh 1975, and others), and for developing flow in a channel (Garg and Gupta 1981). However, the introduction of non-parallelism also results in great sensitivity to the quantity used to measure instability (*e.g.* growth in axial or transverse velocity, kinetic energy, *etc.*), so that it is difficult to quantify the degree to which this is the case, and the magnitude of the effect may be less than was previously thought (Fasel and Konzelmann 1990). Further, as all of the previous studies have considered only the TSI, it remains to be shown how non-parallelism influences the channel wall-fluid instabilities. However, the previous studies suggest that the variation of the stability boundary due to the degree of non-parallelism present in the systems we consider may be fairly small, and a detailed numerical study for Blasius flow demonstrated that parallel flow results provide a good leading order approximation for the desired stability results (Fasel and Konzelmann 1990). We have therefore chosen not to undertake an analysis of the nonparallel problem here.

§7.5 *Directions for future work*

There are several extensions to the present work suggested by the discussions above and in Chapter 6. The influence of nonparallelism in both the base flow and collapsed tube geometry on the comparison between the theoretical and experimental results was seen in §6.2. It would thus be useful to include the effects of nonparallelism in the stability analysis of the channel flow that we considered. By including these effects in a multi-scale analysis (as Saric and Nayfeh 1975, for example), the present work would serve as the leading order result in a perturbative solution in small parameters measuring the degree of contraction of the tube and the

nonparallelism in the flow.

A more complete analysis of the developing flow field going into the collapsed tube section, by extending our FIDAP analysis, for example, would similarly clarify comparisons between theory and experiments. Such an investigation would show not only the nature of the actual flow profile in the collapsed channel section, but also the degree to which three dimensionality might enter into the flow.

The present stability code could readily be applied to investigate the stability of other physiological flows, such as blood flow. As noted above, however, arterial flows are significantly pulsatile, suggesting that the addition of an oscillatory component to the flow field would be physically relevant. For a small amplitude oscillatory component this could be incorporated as a perturbation to the present work.

Finally, we have considered only linear stability theory. To investigate the actual evolution of the instability a nonlinear analysis is required. This might be approached using a weakly nonlinear theory similar to the investigations of Grotberg and Reiss (1984, 1985), or could alternatively use a strongly nonlinear long wave analysis (Atherton and Homsy 1976). In the applications investigated in Chapter 6 even the flutter instability was found for fairly long wavelengths ($k \approx 0.1$), suggesting that a nonlinear long wave analysis may be useful in determining the nature of the transition between the long-wave and flutter instabilities.

REFERENCES

- Atherton, R.W., & G. M. Homsy. 1976. On the derivation of evolution equations for interfacial waves, *Chem. Engng. Communications* 2:57-77.
- Batchelor, G.K., 1967. *An Introduction to Fluid Dynamics*, Cambridge University Press.
- Benjamin, B. 1960. Effects of a flexible boundary on hydrodynamic stability, *J. Fluid Mech.* 9:513-532.
- Benjamin, T.B. 1963. The threefold classification for unstable disturbances in flexible surfaces bounding inviscid flows, *J. Fluid Mech.* 16:436-450.
- Benjamin, T.B. 1964. Fluid flow with flexible boundaries, from *Proceedings of the 11th International Congress on Applied Mathematics*, H. Görtler, Ed.
- Bodoia, J.R., & J.F. Osterle. 1961. Finite difference analysis of plane Poiseuille and Couette flow developments, *Appl. Sci. Res. A* 10:265-276.
- Brandt, A., & J. Gillis. 1964. Magnetohydrodynamic flow in the inlet region of a straight channel, *Phys. Fluids* 9(4):690-699.
- Brazier-Smith, P.R., & J.F. Scott. 1984. Stability of fluid flow in the presence of a compliant surface, *Wave Motion* 6:547-560.
- Campbell, W.D., & J.C. Slattery. 1963. Flow in the entrance of a tube, *J. Basic Engng.* 85:41-46.
- Cancelli, C., & T.J. Pedley. 1985. A separated-flow model for collapsible-tube oscillations, *J. Fluid Mech.* 157:375-404.
- Carpenter, P.W. 1984. The effect of a boundary layer on the hydroelastic instability of infinitely long plates, *J. Sound Vibration* 93(3):461-464.
- Carpenter, P.W., & J.S.B. Gajjar. 1990. A general theory for two- and three- dimensional wall-mode instabilities in boundary layers over isotropic and anisotropic compliant walls, *Theoret. Comput. Fluid Dynamics* 1:349-378.
- Carpenter, P.W., & A.D. Garrad. 1985. The hydrodynamic stability of flow over Kramer-type compliant surfaces. Part 1. Tollmien-Schlichting instabilities, *J. Fluid Mech.* 155:465-510.
- Carpenter, P.W., & A.D. Garrad. 1986. The hydrodynamic stability of flow over Kramer-type compliant surfaces. Part 2. Flow induced surface instabilities, *J. Fluid Mech.* 170:199-232.
- Chen, T.S., & E.M. Sparrow. 1967. Stability of the developing laminar flow in a parallel-plate channel, *J. Fluid Mech.* 30:209-224.

- Collins, M., & W.R. Schowalter. 1962. Laminar flow in the inlet region of a straight channel, *Phys. Fluids* 5:1122-1124.
- Conrad, W.A. 1969. Pressure-flow relationships in collapsible tubes, *IEEE Trans. Biomed. Engng.* 16:84-95.
- Craik, A.D.D. 1991. The continuous spectrum of the Orr-Sommerfeld equation: note on a paper of Grosch & Salwen, *J. Fluid Mech.* 226:565-574.
- Davey, A. 1973. A simple numerical method for solving Orr-Sommerfeld problems, *Q. J. Mech. Appl. Math.*, 26:401-411.
- Dawson, S.V., & E.A. Elliot. 1977. Wave-speed limitation on expiratory flow - a unifying concept, *J. Appl. Physiol.* 43(3):498-515.
- Domaradzki, J.A., & R.W. Metcalfe. 1987. Stabilization of laminar boundary layers by compliant membranes, *Phys. Fluids* 30(3):695-705.
- Dragon, C.A., & J.B. Grotberg. 1991. Oscillatory flow and mass transport in a flexible tube, *J. Fluid Mech.* 231:135-155.
- Drazin P.G., & W.H. Reid. 1981. *Hydrodynamic Stability*, Cambridge University Press.
- Duncan, J.H., A.M. Waxman., & M.P. Tulin. 1985. The dynamics of waves at the interface between a viscoelastic coating and a fluid flow, *J. Fluid Mech.* 158:177-197.
- Ellen, C.H. 1973. The stability of simply supported rectangular surfaces in uniform subsonic flow, *Trans. ASME J. Appl. Mech.* 40:68-72.
- Evrensel, C.A., & A. Kalnins. 1985. Response of a compliant slab to inviscid incompressible fluid flow, *J. Acoust. Soc. Am.* 78(6):2034-2041.
- Evrensel, C.A., & A. Kalnins. 1988. Response of a compliant slab to viscous incompressible flow, *Trans ASME* 55:660-666.
- Fasel, F., & U. Konzelmann. 1990. Non-parallel stability of a flat-plate boundary layer using the complete Navier-Stokes equations, *J. Fluid Mech.* 221:311-347.
- Flaherty, J.E., J.B. Keller., & S.I. Rubinow. 1972. Post buckling behavior of elastic tubes and rings with opposite sides in contact, *SIAM J. Appl. Math.* 23(4):446-455.
- Fletcher, C.A.J. 1991. *Computational techniques for fluid dynamics vol. II*, Springer-Verlag.
- Gad-el-Hak, M. 1986. Boundary layer interactions with compliant coatings: An overview, *Appl. Mech. Rev.* 39(4):511-523.

- Garg, V.K., & S.C. Gupta. 1981. Nonparallel effects on the stability of developing flow in a channel, *Phys. Fluids* 24(9):1752-55.
- Garrad, A.D., & P.W. Carpenter. 1982. A theoretical investigation of flow-induced instabilities in compliant coatings, *J. Sound Vibration* 85(4):483-500.
- Gaster, M. 1974. On the effects of boundary-layer growth on flow stability, *J. Fluid Mech.* 66:465-480.
- Gavriely, N., & J.B. Grotberg. 1988. Flow limitation and wheezes in a constant flow and volume lung preparation, *J. Appl. Physiol.* 64(1):17-20.
- Gavriely, N., Y. Palti, G. Alroy, & J.B. Grotberg. 1984. Measurement and theory of wheezing breath sounds, *J. Appl. Physiol.* 57(2):481-492.
- Gavriely, N., K.B. Kelly, & J.B. Grotberg. 1987. Forced expiratory wheezes are a manifestation of airway flow limitation, *J. Appl. Physiol.* 62(6):2398-2403.
- Gavriely, N., T.R. Shee, D.W. Cugell, & J.B. Grotberg. 1989. Flutter in flow-limited collapsible tubes: a mechanism for generation of wheezes, *J. Appl. Physiol.* 66(5):2251-2261.
- Grosch, C.E., & H. Salwan. 1978. The continuous spectrum of the Orr-Sommerfeld equation. Part 1. The spectrum and the eigenfunctions, *J. Fluid Mech.* 87:33-54.
- Grotberg, J.B., & S.H. Davis. 1980. Fluid-dynamic flapping of a collapsible channel: sound generation and flow limitation, *J. Biomech.* 13:219-230.
- Grotberg, J.B., & N. Gavriely. 1989. Flutter in collapsible tubes: a theoretical model of wheezes, *J. Appl. Physiol.* 66(5):2262-2273.
- Grotberg, J.B., & E.L. Reiss. 1982. A subsonic flutter anomaly, *J. Sound Vibration* 80:444-446.
- Grotberg, J.B., & E.L. Reiss. 1984. Subsonic flapping flutter, *J. Sound Vibration* 92(3):349-361.
- Grotberg, J.B., & E.L. Reiss. 1985. Secondary bifurcation of quasi-periodic solutions can lead to period multiplication, *SIAM J. Appl. Math.* 45(2):169-174.
- Grotberg, J.B., & T.R. Shee. 1985. Compressible-flow channel flutter, *J. Fluid Mech.* 159:175-193.
- Gupta S.C., & V.K. Garg. 1981. Linear spatial stability of developing flow in a parallel plate channel, *Trans. ASME*, 48:192-194.
- Hains, F.D., & J.F. Price. 1962. Effect of a flexible wall on the stability of Poiseuille flow, *Phys Fluids* 5:365

- Hinchey, M.J., & J.W. Snellen. 1987. Lung sounds and flow limitation, *J. Sound Vibr.* **116**(3):576-579.
- Hyatt, R.E. 1983. Expiratory flow limitation, *J. Appl. Physiol.* **55**:1-7.
- Jordinson, R. 1970. The flat plate boundary layer. Part 1. Numerical integration of the Orr-Sommerfeld equation, *J. Fluid Mech.* **43**:801-811.
- Kamm, R.D., & T.J. Pedley. 1989. Flow in collapsible tubes: A brief review, *J. Biomech. Engng.* **111**:177-179.
- Kamm, R.D., & A.H. Shapiro. 1979. Unsteady flow in a collapsible tube subjected to external pressure or body forces, *J. Fluid Mech.* **95**:1-78.
- Katz, A.I., Y. Chen, & A.H. Moreno. 1969. Flow through a collapsible tube. Experimental analysis and mathematical model, *Biophys. J.* **9**:1261-1279.
- Kevorkian, J., & J.D. Cole. 1981. *Perturbation Methods in Applied Mathematics*, Springer-Verlag.
- Kornecki, A. 1974. Static and dynamic instability of panels and cylindrical shells in subsonic potential flow, *J. Sound Vibration* **32**(2):251-263.
- Kornecki, A., E.H. Dowell, & J. O'Brien. 1976. On the aeroelastic instability of two-dimensional panels in uniform incompressible flow, *J. Sound Vibration* **47**(2):163-178.
- Kramen, S.S. 1983. The forced expiratory wheeze: its site of origin and possible association with lung compliance, *Respiration* **44**:189-196.
- Kramer, M.O. 1960. Boundary-layer stabilization by distributed damping, *J. Am. Soc. Naval Engrs.* **74**:341-348.
- Landahl, M.T. 1962. On the stability of a laminar incompressible boundary layer over a flexible surface, *J. Fluid Mech.* **13**:607-632.
- Langhaar, H.L. 1942. Steady flow in the transition length of a straight tube, *J. Appl. Mech.* **9** *Trans ASME* **64**:A55-58.
- Lin, C.C. 1961. Some mathematical problems in the theory of the stability of parallel flows, *J. Fluid Mech.* **10**:430.
- Lucey, A.D., & P.W. Carpenter. 1992. A numerical simulation of the interaction of a compliant wall and inviscid flow, *J. Fluid Mech.* **234**:121-146.
- Lucey, A.D., & P.W. Carpenter. 1993. On the difference between the hydroelastic instability of infinite and very long compliant panels, *J. Sound Vibration* **163**(1):176-81.

- Mack, L.M. 1976. A numerical study of the temporal eigenvalue spectrum of the Blasius boundary layer, *J. Fluid Mech.* **73**:497-520.
- Matsuzaki, Y. & Y.C. Fung. 1977. Stability analysis of straight and buckled two-dimensional channels conveying an incompressible flow, *Trans ASME J. Appl. Mech.* **44**:548-552.
- Miklavčič, M. 1983. Eigenvalues of the Orr-Sommerfeld equation in an unbounded domain, *Arch. Rational Mech. Analysis* **83**:221-228.
- Miles J.W. 1957. On the generation of surface waves by shear flows, *J. Fluid Mech.* **3**:185.
- Olson, D.E., G.A. Dart, & G.F. Filley. 1970. Pressure drop and fluid flow regime of air inspired into the human lung, *J. Appl. Physiol.* **28**(4):482-94.
- Païdoussis, M.P., & N.T. Issid. 1974. Dynamic stability of pipes conveying fluid, *J. Sound Vibration* **33**(3):267-294.
- Pierucci, M., & P.G. Morales. 1990. Effect of finite thickness flexible boundary upon the stability of a Poiseuille flow, *Trans. ASME* **57**:1056-1060.
- Press W.H., B.P. Flannery, S.A. Teukolsky, & W.T. Vetterling. 1990. *Numerical Recipes*, Cambridge University Press.
- Riley, J.J., M. Gad-el-Hak, & R.W. Metcalfe. 1988. Compliant coatings, *Ann. Rev. Fluid Mech.* **20**:393-420.
- Rotenberry, J.M. 1992. Finite-amplitude shear waves in a channel with compliant boundaries, *Phys Fluids A* **4**(2):270-276.
- Rotenberry, J.M., & P.G. Saffman. 1990. Effect of compliant boundaries on weakly nonlinear shear waves in channel flow, *SIAM J. Appl. Math* **50**:361-394.
- Sapir, M.H., & E.L. Reiss. 1979. Dynamic buckling of a nonlinear Timoshenko beam, *SIAM J. Appl. Math* **37**(2):290-301.
- Saric, W.S., & A.H. Nayfeh. 1975. Nonparallel stability of boundary layer flows, *Phys. Fluids* **18**:945-950.
- Schiller, L. 1922. Die Entwicklung der laminaren Geschwindigkeitsverteilung und ihre Bedeutung für Zähigkeitsmessungen, *ZAMM* **2**:96-106.
- Schlichting, H. 1934. Laminare Kanaleinlaufströmung, *ZAMM* **14**:368-373.
- Schlichting, 1955. *Boundary Layer Theory*, McGraw-Hill.
- Schmidt F.W., & B. Zeldin B. 1969. Laminar flows in inlet sections of tubes and ducts, *AIChE J.* **15**(4):612-614.

- Sen, P.K., & D.S. Arora. 1988. On the stability of laminar boundary-layer flow over a flat plate with a compliant surface, *J. Fluid Mech.* **197**:201-240.
- Shabtai, S-M., J.B. Grotberg, & N. Gavriely. 1992. Spectral content of forced expiratory wheezes during air, helium and SF₆ breathing in normal man, *J. Appl. Physiol.* **72**:629-635.
- Shapiro, A.H. 1977. Steady flow in collapsible tubes, *J. Biomech. Engng.* **99**:126-147.
- Sparrow, E.M, S.G. Lin, & T.S. Lundgren. 1964. Flow development in the hydrodynamic entrance region of tubes and ducts, *Phys. Fluids* **7**:338-347.
- Van Dyke, M. 1970. Entry flow in a channel, *J. Fluid Mech.* **44**:813-823.
- Walsh, C., P.A. Sullivan, & J.S. Hanson. 1991. Subcritical flutter in collapsible tube flow: A model of expiratory flow in the trachea, *J. Biomech. Engng.* **113**:21-26.
- Wang, Y.L. & P.A. Longwell. 1964. Laminar flow in the inlet section of parallel plates, *AIChE J.* **10**(3):323-329.
- Weaver, D.S., & M.P. Paidoussis. 1977. On collapse and flutter phenomena in thin tubes conveying fluid, *J. Sound Vibration* **50**(1):117-132.
- Weaver, D.S., & T.E. Unny. 1970. The hydroelastic stability of a flat plate, *Trans. ASME J. Appl. Mech.* **37**:823-829.
- Weaver, D.S., & T.E. Unny. 1973. On the dynamic stability of fluid-conveying pipes, *Trans. ASME J. Appl. Mech.* **40**:48-53.
- Webster, P.M., R.P. Sawatzky, V. Hoffstein, M.J. Hinchey & P.A. Sullivan. 1985. Wall motion in expiratory flow limitation: choke and flutter, *J. Appl. Physiol.* **59**:1304-1312.
- White, F.M. 1974. *Viscous fluid flow*, McGraw-Hill.
- Wilson, S. 1970. The development of Poiseuille flow, *J. Fluid Mech.* **38**:793-806.
- Wilson, S. 1971. Entry flow in a channel. Part 2, *J. Fluid Mech.* **46**:787-799.
- Wilson, T.A., J.R. Rodarte, & J.P. Butler. 1986. Wave-speed and viscous flow limitation, in *Handbook of Physiology*, section 3: The Respiratory System, Vol. III, American Physiological Society.
- Yeo, K.S., & A.P. Dowling. 1987. The stability of inviscid flows over passive compliant walls, *J. Fluid Mech.* **183**:265-292.

APPENDIX A: FINITE DIFFERENCE SOLUTION FOR DEVELOPING CHANNEL FLOW

§A.1 *Problem formulation and uniform grid difference scheme*

In this appendix we formulate a finite difference solution for the flow in a rigid channel that develops from an initially uniform profile. In the boundary layer at the walls of the channel the flow is governed by Prandtl's boundary layer equations. We assume that the simplification involved in the derivation of these equations, namely the assumption that axial diffusion is negligible, may be applied throughout the channel and thus that they may be solved to obtain a complete description of the flow. This reduction is significant, as it reduces the elliptic Navier-Stokes equations to a parabolic form. We may then solve the boundary layer equations with a finite difference formulation, treating the axial coordinate as a time like variable and marching downstream from the initial condition at the channel mouth.

The boundary layer equations are, scaled on the initial (uniform) flow speed S^* and half channel width b^* ,

$$u u_x + v u_y = -\frac{dp}{dx} + \frac{1}{Re} u_{yy} \quad \text{and} \quad u_x + v_y = 0, \quad (\text{A.1})$$

where y is the transverse coordinate ($y=0$ at the wall and $y=1$ at the midline), $Re \equiv S^* b^* / \nu^*$, and u and v are the axial and transverse velocities, respectively. In an unbounded domain the value of dp/dx is given by the inviscid solution for the outer region of the flow; in the case of a channel, however, the central (inviscid) core is accelerated as a consequence of conservation of mass. Thus the fluid pressure, as well as the fluid velocities, must be found. To accomplish this, we impose a constraint requiring that the flow rate in the channel be constant, namely

$$\int_0^1 u \, dy = 1. \quad (\text{A.2})$$

The boundary conditions on the flow are no slip at the wall and a symmetry condition at the midline: $u=v=0$ at the wall, $\partial u/\partial y=v=0$ at the midline.

To solve (A.1) and (A.2) subject to the given boundary conditions, we introduce a grid with axial and transverse indices n and j , respectively, where $1 \leq n \leq n_{\text{tot}}$ and $1 \leq j \leq j_{\text{tot}}$. $n=1$ corresponds to the channel mouth, $j=1$ the channel wall and $j=j_{\text{tot}}$ the channel midline. We replace y derivatives in the momentum equation ((A.1), first equation) with the second order accurate central difference formulas

$$\begin{aligned} \frac{\partial}{\partial y} u_j^{n+1} &= \frac{1}{2\Delta y} (u_{j+1}^{n+1} - u_{j-1}^{n+1}) + O(\Delta y^2) \\ \frac{\partial^2}{\partial y^2} u_j^{n+1} &= \frac{1}{\Delta y^2} (u_{j+1}^{n+1} - 2u_j^{n+1} + u_{j-1}^{n+1}) + O(\Delta y^2). \end{aligned} \quad (\text{A.3})$$

In (A.3) and equations that follow we denote the value of variables at the (n,j) th grid point with a superscripted n and subscripted j ; Δy and Δx indicate the grid spacing in the transverse or axial directions, respectively. For the x derivatives in the momentum equation we use a second order upwind difference formula,

$$\frac{\partial}{\partial x} s_j^{n+1} = \frac{1}{\Delta x} \left(\frac{3}{2} s_j^{n+1} - 2s_j^n + \frac{1}{2} s_j^{n-1} \right) + O(\Delta x^2), \quad s = u_j \text{ or } p. \quad (\text{A.4})$$

Finally, to maintain linearity in the momentum equation we introduce second order accurate approximations for the nonlinear factors of u and v in the inertial terms of (A.1),

$$s_j^{n+1} = 2s_j^n - s_j^{n-1}, \quad s = u \text{ or } v. \quad (\text{A.5})$$

The continuity equation ((A.1), second equation) is evaluated at the $j+1/2$ th transverse grid

point, so that the second order accurate central difference approximation for the y derivative of v is

$$\frac{\partial}{\partial y} v_{j+\frac{1}{2}}^{n+1} = \frac{1}{\Delta y} (v_{j+1}^{n+1} - v_j^{n+1}) + O(\Delta y^2). \quad (\text{A.6})$$

The x derivative of u in (A.1b) is evaluated using the upwind difference formula (A.4), with the values of u at the $j+1/2$ th grid point being expressed as the average of the values at the jth and $j+1$ st points, so that

$$\frac{\partial}{\partial x} u_{j+\frac{1}{2}}^{n+1} = \left[\frac{1}{2\Delta x} \left(\frac{3}{2} (u_{j+1}^{n+1} + u_j^{n+1}) - 2(u_{j+1}^n + u_j^n) + \frac{1}{2} (u_{j+1}^{n-1} + u_j^{n-1}) \right) \right] + O(\Delta x^2, \Delta y^2). \quad (\text{A.7})$$

The integral flux condition is evaluated using a fourth order accurate open integration formula,

$$\begin{aligned} \int_0^1 u^{n+1} dy = \Delta y & \left(\frac{109}{48} u_2^{n+1} - \frac{5}{48} u_3^{n+1} + \frac{63}{48} u_4^{n+1} + \frac{49}{48} u_5^{n+1} + \right. \\ & u_6^{n+1} + \dots + u_{j_{tot}-5}^{n+1} + \frac{49}{48} u_{j_{tot}-4}^{n+1} + \frac{63}{48} u_{j_{tot}-3}^{n+1} - \\ & \left. \frac{5}{48} u_{j_{tot}-2}^{n+1} + \frac{109}{48} u_{j_{tot}-1}^{n+1} \right) + O\left(\frac{1}{j_{tot}^4}\right). \end{aligned} \quad (\text{A.8})$$

Using (A.3), (A.4), and (A.5) in the momentum equation, (A.6) and (A.7) in the continuity equation, and (A.8) in the integral flux condition (A.2), we obtain the difference system

$$\begin{aligned}
& \left[-2 \frac{\Delta x}{\Delta y^2} - Re \frac{\Delta x}{\Delta y} (2v_j^n - v_j^{n-1}) \right] u_{j-1}^{n+1} + \left[4 \frac{\Delta x}{\Delta y^2} + 3Re(2u_j^n - \right. \\
& \left. u_j^{n-1}) \right] u_j^{n+1} + \left[-2 \frac{\Delta x}{\Delta y^2} + Re \frac{\Delta x}{\Delta y} (2v_j^n - v_j^{n-1}) \right] u_{j+1}^{n+1} + 3Rep^{n+1} \\
& = Re(4p^n - p^{n-1}) + Re(2u_j^n - u_j^{n-1})(4u_j^n - u_j^{n-1}),
\end{aligned} \tag{A.9}$$

with continuity,

$$\begin{aligned}
\frac{\Delta x}{\Delta y} (v_{j+1}^{n+1} - v_j^{n+1}) &= -\frac{1}{2} [(u_{j+1}^{n+1} + u_j^{n+1}) - \\
& 2(u_{j+1}^n + u_j^n) + \frac{1}{2}(u_{j+1}^{n-1} + u_j^{n-1})].
\end{aligned} \tag{A.10}$$

and the integral flux condition

$$\sum_{j=2}^{j_{tot}-1} a_j u_j^{n+1} = j_{tot}, \tag{A.11}$$

where the a_j are given in (A.8). To evaluate the no flux condition at the midline, we note that from the central difference formula (A.3) the condition $\partial u_{j_{tot}} / \partial y = 0$ is equivalent to requiring $u_{j_{tot}+1} = u_{j_{tot}-1}$. Thus to implement the no flux condition we apply the momentum equation (A.9) for the midline grid point and use the given relationship between $u_{j_{tot}+1}$ and $u_{j_{tot}-1}$ to eliminate the value of $u_{j_{tot}+1}$.

Equations (A.9) and (A.10) with boundary conditions $u_1^n = 0$, the no flux condition, and initial conditions $u_j^1 = 1$, $p = p_0$ form a problem for u_j^{n+1} and p^{n+1} of the form $\mathbf{M}_1 \mathbf{q}_1 = \mathbf{R}_1$, where the matrix \mathbf{M}_1 is tridiagonal and doubly bordered, and the vectors \mathbf{q}_1 and \mathbf{R}_1 are given by $\mathbf{q}_1 = (u_1^{n+1} \cdots u_{j_{tot}}^{n+1} p^{n+1})^T$ and \mathbf{R}_1 = the right hand sides of (A.9) and (A.10). This may be solved for u and p at the $n+1$ st axial grid point, after which (A.11) with boundary condition $v_1^{n+1} = 0$ and initial condition $v_j^1 = 0$ may be easily solved for v_j^{n+1} . The problem for v_j^{n+1} is of the same form as that for u and p , $\mathbf{M}_2 \mathbf{q}_2 = \mathbf{R}_2$, but in this case the matrix \mathbf{M}_2 is constant for all axial

positions in the channel, so that the matrix inversion need be done only once at the beginning of the calculation.

For the calculation of the velocity and pressure at the first point downstream of the channel inlet we do not have available the two levels of data for u and p required by the upwind difference formula (A.4), and so use a first order difference approximation for this step only,

$$\frac{\partial}{\partial x} s^{n+1} = \frac{1}{\Delta x} (s^{n+1} - s^n) + O(\Delta x), \quad s = u_j \text{ or } p. \quad (\text{A.12})$$

§A.2 *Modifications for a non-uniform grid*

The fundamental difficulty in attempting to solve the system outlined in §A.1 lies in resolving the transition between the initial condition that fails to satisfy the no slip condition at the wall and the flow in the remainder of the channel, for which we require the condition be satisfied. To obtain an accurate description of the flow we must thus have a large number of grid points in the region over which this transition is effected, namely, the boundary layer near the wall. We do not, however, need such a concentration of points in the middle of the channel, where the flow is changing only slightly. This is accomplished through the introduction of a non-uniform transverse grid to concentrate points near the wall. To do this, we introduce a new variable $Y=g(y)$, where $g(y)$ is defined so that when the problem is solved on a uniform set of points Y_j the corresponding points $y_j=g^{-1}(Y_j)$ have the desired spacing. We use the transformation $g(y) = Py + (1 - P)(1 - \tanh(Q(1-y)))/\tanh(Q)$ (Fletcher 1991); P and Q are free parameters chosen to alter the degree of non-uniformity.

The introduction of this new variable changes the boundary layer equations (A.1) and integral condition (A.2) through the replacement of $\partial/\partial y$ and $\partial^2/\partial y^2$ with $(dY/dy)(\partial/\partial Y)$ and

$[(d^2Y/dy^2)(\partial/\partial Y) + (dY/dy)^2(\partial^2/\partial Y^2)]$, respectively. This change does not alter the difference formulas used, however, as it involves only the addition of known coefficients; solution of the problem then proceeds as indicated in §A.1.

§A.3 *Results*

To obtain meaningful results with the finite difference code the axial step size Δx must be chosen to avoid instability; if the step size is too small the system becomes unstable as the flow progresses downstream. At the same time, a small step is required near the channel inlet to resolve the transition from a plug to a viscous profile. Thus the first few steps are taken with a small value of Δx , and thereafter a larger step size is used.

To test that the results produced by the code are accurate, a Poiseuille profile is introduced as an initial condition. This profile remains parabolic at arbitrary positions downstream, with a the pressure drop that is linear in the axial coordinate, as it should be.

The developing flow pressure drop and axial velocity at various positions downstream of the inlet are shown for a plug initial condition in figure A.1. Some jaggedness is seen for small x in the plot for pressure; this is a result of the discontinuous change from a slip to a no slip profile at the inlet. The difference between the pressure drop for the plug initial condition and that for a Poiseuille flow is a useful measure by which to compare with the results of other investigations. We find this difference to be $q=0.341$ (in non-dimensional pressure units); this is consistent with other solutions of the problem. (For comparison, Schlichting (1934) finds $q=0.313$; Bodoia and Osterle (1961) have $q=0.338$; and Brandt and Gillis (1966) give $q=0.331$.)

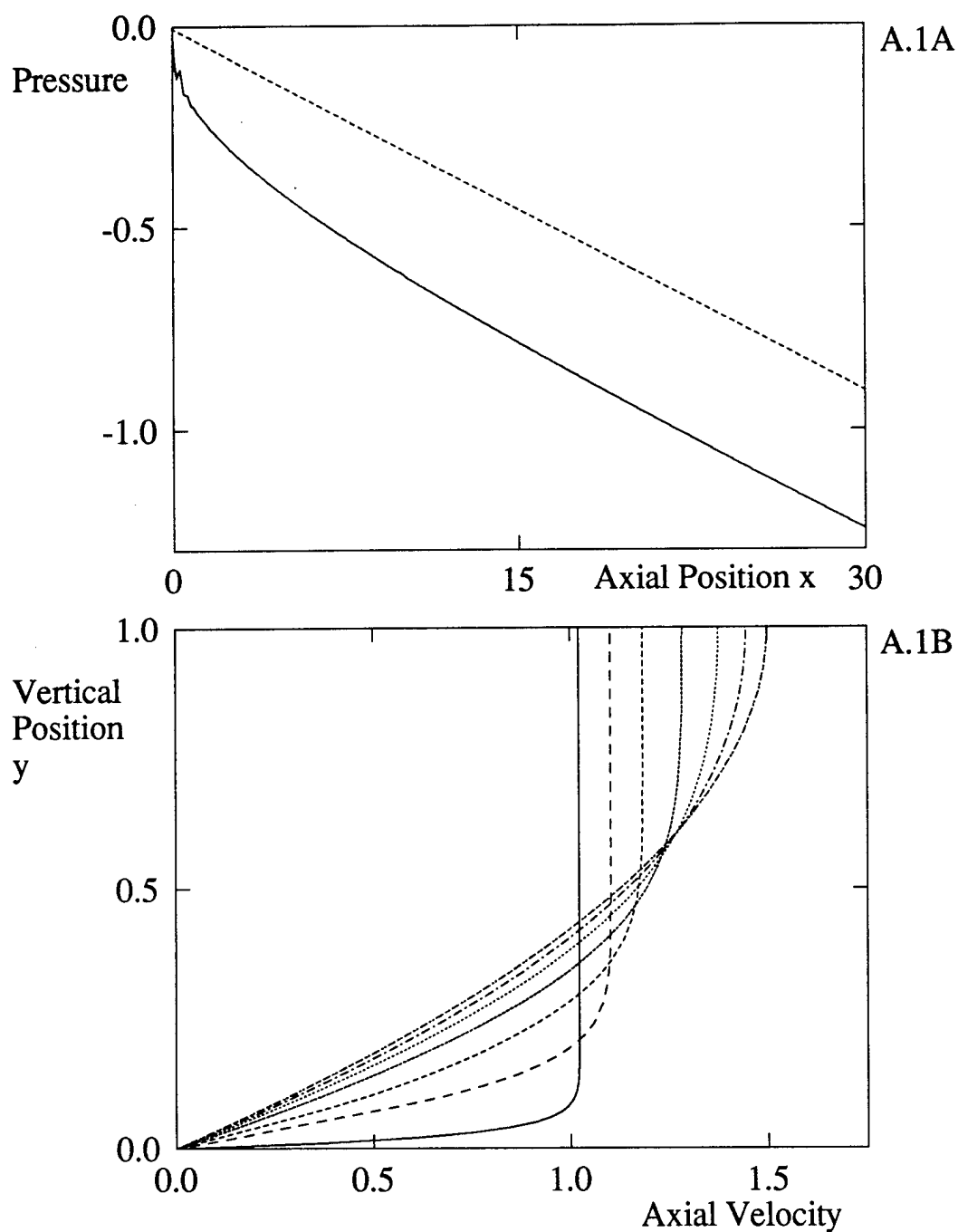


Figure A.1: Finite difference solution for developing channel flow. A.1A: Pressure as a function of axial coordinate x . Solid curve gives developing flow result; dashed, Poiseuille flow. A.1B: Developing flow profiles at axial positions $x=0.05, 0.35, 0.88, 2.8, 5.7, 10$, and 30 . Curve for $x=30$ is Poiseuille flow.

APPENDIX B: FIDAP SOLUTION FOR FLOW IN A COLLAPSED TUBE

§B.1 *Solution procedure*

To use FIDAP, it is necessary to specify the domain of interest and the mesh desired for the finite element solution; this is done for two different approximations to the collapsed tube cross-sectional shape. Due to the two axes of symmetry in the problem, a solution may be obtained for one quarter of the entire tube cross-section and the flow in the remainder of the tube inferred from this reduced problem. The collapsed tube shape is inherently three-dimensional, so that it is not possible to resort to axi-symmetry or two-dimensionality to further simplify the domain considered, but for the purposes of this calculation we are willing to consider the steady flow problem, so that the length of the tube section in which a solution is calculated may be short with periodic boundary conditions. In figure B.1 the domain in which the computation is carried out is shown with the element mesh used. No slip or symmetry conditions are imposed on the appropriate non-periodic boundaries, and the full steady Navier-Stokes equations solved subject to these boundary conditions. To ensure that the mesh being used gives an accurate solution to the problem, a mesh that was half again as dense was used for comparison; little difference between the solutions obtained with the original and refined mesh was observed.

§B.2 *Results*

Vector plots showing the flow profiles generated by FIDAP are shown in figures B.2A and B.2B for the domains considered. Contour plots of the same solutions are shown in figure B.3A and B.3B.

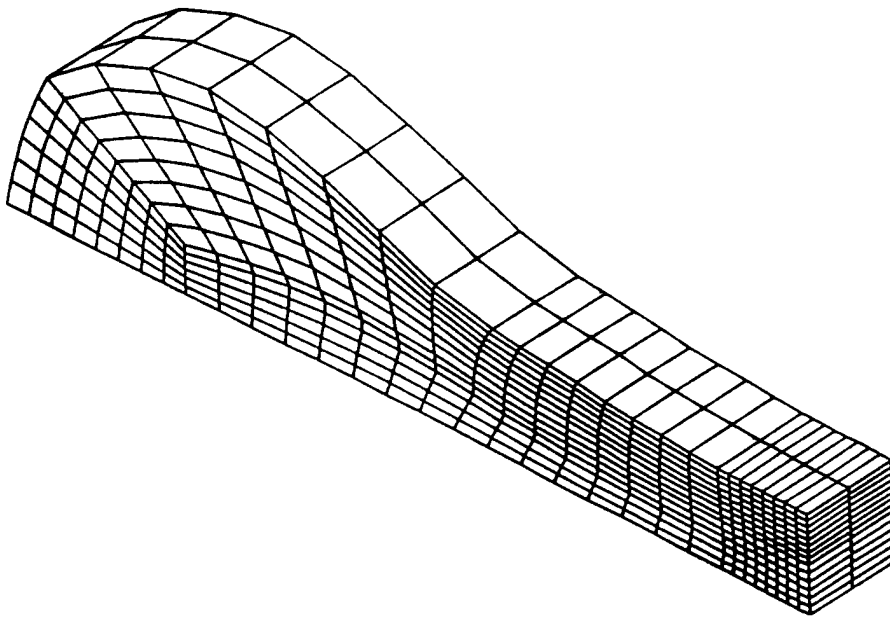
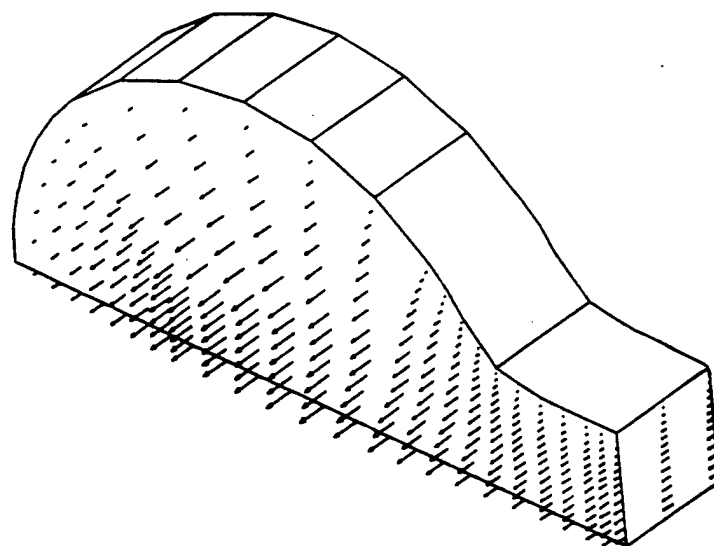
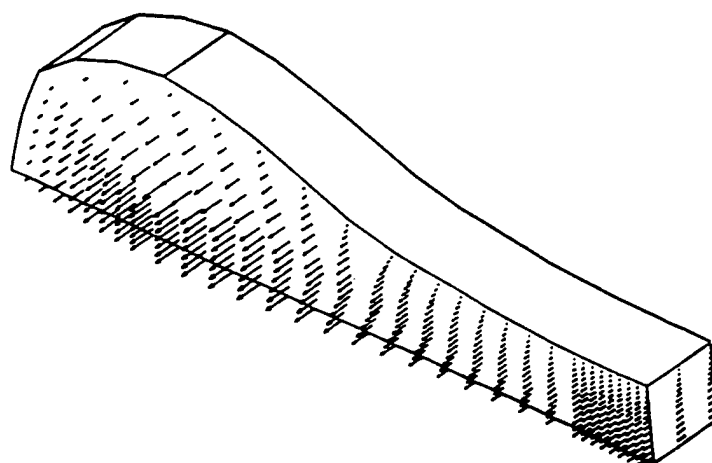


Figure B.1 Meshed domain for FIDAP computations

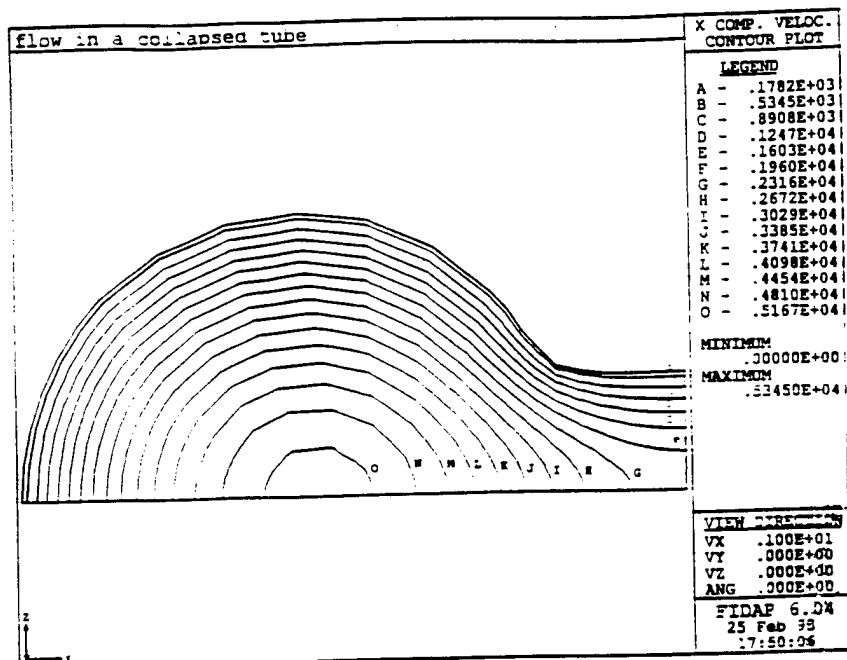


B.2A

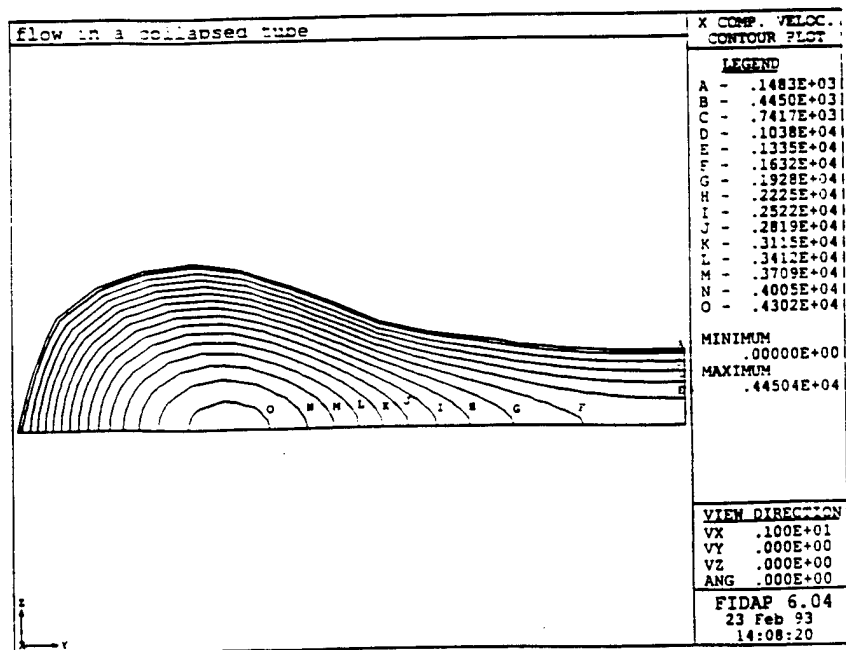


B.2B

Figure B.2 Vector plots of steady velocity in collapsed tube cross-section. B.2A and B.2B show velocities for each of the two tube shapes considered.



B.3A



B.3B

Figure B.3 Contour plots of steady velocity in collapsed tube cross-section.
B.3A and B.3B show velocities for each of the two tube shapes considered.

PETER GAVIN LAROSE

PERSONAL

Address: Dept. Applied Math., Northwestern University
2145 Sheridan Road, Evanston IL 60208
Phone: (708) 491-4308 (work), (708) 328-4326 (home)
E-mail: glarose@nwu.edu
Citizenship: United States

EDUCATION

Northwestern University, Evanston, IL
1994 Ph.D. Engineering Sciences and Applied Mathematics
Dissertation: *Wall-Fluid Instabilities in Compliant Channels Conveying Developing Flows.*
1991 M.S. Engineering Sciences and Applied Mathematics (GPA 4.0/4.0)
Coursework in mathematical modelling, asymptotic and perturbation analysis, differential equations, numerical methods (including finite difference and spectral methods), nonlinear analysis, wave propagation, solidification and fluid mechanics.
Grinnell College, Grinnell, IA
1989 B.A. with Honors Major in Mathematics (GPA 3.9/4.0)

EXPERIENCE

Fall 1993-present **Teaching Assistant, Northwestern University, Evanston, IL**
Taught undergraduates in class and problem discussion sessions, for classes in calculus and differential equations. Coordinated grading and other activities of TAs working on the same courses.
1989-present **Graduate Researcher, Northwestern University, Evanston, IL**
Developed a channel model for a collapsed flexible tube. Evaluated the linear stability of this model analytically and numerically.
Demonstrated shortcomings of previous models and found new physically relevant system behaviors.
Summer 1993 **Instructor, 1993 National High School Institute, Evanston, IL**
Developed and taught a mathematical modelling course, 'Mathematics and the real world' including laboratory computer experience and exposure to advanced mathematical concepts.
Summer 1993 **Research Project Advisor, 1993 National High School Institute, Evanston, IL**
Guided students in individual research projects to explore the formulation and solution of mathematical models.

Summer 1990 **USAF Graduate Research Fellow, *Universal Energy Systems, Dayton, OH***
 Investigated characteristics of the breakup of a small cylindrical liquid jet experimentally to test theoretical predictions, showing needed refinements to the existing theory.

HONORS

XΔX Award for Teaching Excellence, Fall 1993
 National Defense Science and Engineering Graduate Fellowship, 1990-1993
 NSF Graduate Fellowship Honorable Mention, 1990
 Royal E. Cabell Graduate Fellowship, Northwestern University, 1989-1990
 Lynn Smith Prize for Excellence in Mathematics, Grinnell College, May 1989
 Deans List, Grinnell College, 7 of 8 semesters, 1985-1989
 Phi Beta Kappa, May 1988

PUBLICATIONS

Chin, L.P., LaRose, P.G., Tankin, R.S., and Switzer, G.
 Droplet distributions from the breakup of a cylindrical liquid jet,
Phys. Fluids A 3:1897-1906.

LaRose, P.G., and Grotberg, J.B. Wall-fluid instabilities in
 compliant channels conveying developing flows (in preparation)

PRESENTATIONS

LaRose, P.G. and Grotberg, J.B. Modelling fluid dynamic
 flutter in lung airways, 18th International Conference on Lung Sounds,
 Alberta, Canada, August 25-27, 1993.

LaRose, P.G. and Grotberg, J.B. Flutter instabilities in developing flow in a
 compliant channel, American Physical Society Division of Fluid
 Dynamics Meeting, Albuquerque NM, November 21-23, 1993.

PROFESSIONAL ACTIVITIES AND MEMBERSHIPS

Workstation Administrator

Managed an IBM RS/6000 UNIX workstation. Installed operating system and software, organized user accounts and set system configuration.

Supercomputing Techniques Workshop Participant

Learned techniques of supercomputer programming and use. Pittsburgh Supercomputing Center, Pittsburgh, PA, April 26-29, 1993.

Member, American Mathematical Society

Mathematical Association of America
 Society for Industrial and Applied Mathematics